[1] The Faculty of Civil Engineering, Wrocław University of Technology
Wybrzeże Wyspiańskiego 27, 50-370 Wrocław, Poland
Tel. +48 71 320 41 35, Fax. +48 71 320 41 05, E-mail: jan.kmita@pwr.wroc.pl

[2] The Faculty of Civil Engineering, Wrocław University of Technology
Wybrzeże Wyspiańskiego 27, 50-370 Wrocław, Poland
Tel. +48 71 320 34 04, E-mail: wojciech.glabisz@pwr.wroc.pl

[3] The Faculty of Mechanical Engineering, Wrocław University of Technology
ul. Łukasiewicza 5, 50-371 Wrocław, Poland
Tel. +48 71 320 21 73, Fax. +48 71 320 34 22, E-mail: metalplast@pwr.wroc.pl

ARCHIVES
OF CIVIL AND MECHANICAL
ENGINEERING

Contents

Spis treści

Random eigenvibrations of elastic structures by the response function method and the generalized stochastic perturbation technique

M.M. KAMIŃSKI, J. SZAFRAN

Faculty of Civil Engineering, Architecture and Environmental Engineering, Technical University of Łódź, al. Politechniki 6, 93-590 Łódź, Poland.

This paper addresses the important question in structural analysis how to efficiently model the eigenvibrations of the spatial structures with random physical and/or geometrical parameters. The entire computational methodology is based on the traditional Finite Element Method enriched with the stochastic perturbation technique in its generalized nth order approach, while the computational implementation is performed by the use of the academic FEM software in conjunction with the symbolic algebra computer system MAPLE. Contrary to the previous straightforward solution techniques, now the response function method is applied to compute any order probabilistic moments and coefficients of the structural eigenvalues. The response function is assumed in the polynomial form, the coefficients of which are computed from the several solutions of the deterministic problem around the mean value of the given input random parameter. This method is illustrated with the stochastic eigenvibrations of the simple single degree of freedom system and small steel tower modelled as the 3D truss structure with random mass density and Young modulus. This technique may find its wide application in reliability analysis of the real existing engineering structures using the commercial Finite Element Method packages as well as the other discrete computational techniques like the Finite Difference Method at least.

Keywords: *stochastic dynamics, Stochastic Finite Element Method, response function method, stochastic perturbation*

1. Introduction

The analysis of structures with random parameters plays an important role in structural design, optimization and reliability modelling. It results from various and numerous sources of randomness like manufacturing processes, static fracture and dynamically driven fatigue of the structural elements, stochastic degradation of material and geometrical parameters of those elements. The important role play here also stochastic vibrations resulting from the possible earthquakes and wind induced vibrations, car accidents and at least but not last, some weather influence on the structures like ice and snow coverage in some colder regions of the world. This variety and the nature of some structures exploitation leaded to the formulation and the solution to the eigenvibrations problems for the spatial structures with random parameters. Although the model presented in the paper is illustrated with the example of the three dimen-

sional model of the telecommunication tower, it can be applied after some small modifications to the other shell and spatial structures as well.

There are several well established both mathematical and numerical models enabling for inclusion of randomness in design parameters into the structural dynamics problems solutions, see [1, 5–9]. Starting from the analytical approaches based on the response spectrum analysis, through the crude Monte-Carlo stochastic simulation till the computational spectral methods based on the Karhunen–Loeve or polynomial chaos expansions of the input random fields. On the other hand, there are the lower order stochastic perturbation methods, however they have fundamental bounds on the input random dispersion level, so that their application to the real engineering problems may be limited. Taking into account those limitations, huge time consumptions for the simulation method, large expansions for the chaos expansions as well as the availability for analytical solutions in the specific problems only, the new method is proposed here.

This new method is based on the Taylor expansion of any desired order with random coefficients of all uncertain parameters and state functions around their expected values. The second new idea here is an application of the response function method in conjunction with this generalized stochastic perturbation technique. We suppose that the output state function, namely the particular eigenvalue may be represented by the polynomial form of the input random parameter. The coefficients for this response polynomium are computed from the several solutions of the original problem obtained for this parameter values taken around its mean value. The polynomial form of the response function leads to the easy determination of its partial derivatives with respect to this random input parameter, which can be finally employed for analytical determination of the probabilistic moments; it essentially differs from the previous straightforward solution to the equations of an increasing order (like zeroth, first, etc.). The computational implementation of this method is realized with the classical Finite Element Method program enriched with some stochastic procedures written in the symbolic algebra computer system MAPLE, where the response function formation, its coefficients determination as well as the final derivation of the probabilistic moments is carried out. The nature of this implementation will allow in the nearest future some similar implementations with the use of the commercial packages of the FEM and the other computer methods. The entire procedure is tested on the example of the 3D truss structures with random Young modulus and, separately, mass density of the structural members. It shows that the method converges relatively fast (eight and tenth order approaches returns almost the same results).

2. The generalized stochastic perturbation

Let us introduce the random variable $b \equiv b(\omega)$ and its probability density function as $p(b)$. Then, the first two probabilistic moments of this field are defined as

$$E[b] \equiv b^0 = \int_{-\infty}^{+\infty} b\, p(b) db \tag{1}$$

and

$$Cov(b(x_r), b(x_s)) = \int\limits_{-\infty}^{+\infty} [b(x_r) - b^0(x_r)][b(x_s) - b^0(x_r)] p(b) dba. \tag{2}$$

The basic idea of the stochastic perturbation approach is to expand all the input variables and all the state functions of the given problem via Taylor series about their spatial expectations using some small parameter $\varepsilon > 0$. In case of random quantity $b \equiv e$, the following expression is employed:

$$e = e^0 + \sum_{n=1}^{\infty} \frac{1}{n!} \varepsilon^n \frac{\partial^n e}{\partial b^n} (\Delta b)^n, \tag{3}$$

where:

$$\varepsilon \Delta b = \varepsilon (b - b^0) \tag{4}$$

is the first variation of b around its expected value and

$$\varepsilon^2 (\Delta b)^2 = \varepsilon^2 (b - b^0)^2, \tag{5}$$

denotes the second variation of b about b^0. Symbol $(.)^0$ represents the function value $(.)$ taken at the expectation b^0, while $(.)^{,b}$, $(.)^{,bb}$ denote the first and the second partial derivatives with respect to b evaluated at b^0, respectively. Let us analyze further the expected values of any state function $f(b)$ defined analogously to the formula (3) by its expansion via Taylor series with a given small parameter ε as follows:

$$E[f(b); b] = \int\limits_{-\infty}^{+\infty} f(b) p(b) db = \int\limits_{-\infty}^{+\infty} \left(f^0 + \sum_{n=1}^{\infty} \frac{1}{n!} \varepsilon^n f^{(n)} \Delta b^n \right) p(b) db. \tag{6}$$

Let us remind that this power expansion is valid only if the state function is analytic in ε and the series converge and, therefore, any criteria of convergence should include the magnitude of the perturbation parameter; perturbation parameter is taken as equal to 1 in many practical computations. Contrary to the previous analyses in this area, now the quantity ε is treated as the expansion parameter in further analysis, so that it is included explicitly in all the further derivations demanding analytical expressions. Numerical studies performed in the next section demonstrate the influence of this parameter on the expected values and standard deviations in various orders of the perturbation methodology. Both moments are obtained in the form of polynomials of the additional order with respect to the parameter ε.

From the numerical point of view, the expansion provided by Equation (6) is carried out for the summation over the finite number of components. Considering various probability distributions, the essential difference is noticed between symmetric distribution functions, where

$$E[f(b);b] = f^0 + \int_{-\infty}^{+\infty} \left(\sum_{n=1}^{2M} \frac{1}{(2n)!} \varepsilon^{2n} \frac{\partial^{2n} f}{\partial b^{2n}} \Delta b^{2n} \right) p(b) db \tag{7}$$

and non-symmetric probability functions

$$E[f(b);b] = f^0 + \int_{-\infty}^{+\infty} \left(\sum_{n=1}^{N} \frac{1}{(n)!} \varepsilon^{n} \frac{\partial^{n} f}{\partial b^{n}} \Delta b^{n} \right) p(b) db. \tag{8}$$

Let us focus now on analytical derivation of the first two probabilistic moments for the structural response function. According to Equation (6) it yields for the input random variable with symmetric probability density function in the second order perturbation approach

$$E[f(b);b] = \int_{-\infty}^{+\infty} \left(f^0 + \varepsilon f^{,b} \Delta b + \tfrac{1}{2} \varepsilon^2 f^{,bb} \Delta b \Delta b \right) p(b) db$$
$$= f^0(b) + 0 \times \varepsilon f^{,b}(b) + \tfrac{1}{2} \varepsilon^2 f^{,bb}(b) S_{bb}. \tag{9}$$

This expected value can be calculated or symbolically computed only if it is given as some analytical function of the random input parameter b. Many existing models in various branches of engineering can be adopted to achieve this goal. Computational implementation of the symbolic calculus programs, combined with powerful visualization of probabilistic output moments, assures the fastest solution of such problems. If higher order terms are necessary (because of a great random deviation of the input random variable about its expected value), then the following extension can be proposed:

$$E[f(b);b] = f^0(b) + \tfrac{1}{2} \varepsilon^2 f^{,bb}(b) \mu_2(b) + \tfrac{1}{4!} \varepsilon^4 f^{,bbbb}(b) \mu_4(b)$$
$$+ \tfrac{1}{6!} \varepsilon^6 f^{,bbbbbb}(b) \mu_6(b) + \dots \tag{10}$$

where $\mu^n(b)$ denotes nth order central probabilistic moment of the quantity b and where all terms with the odd orders are equal to 0 for the Gaussian random deviates and where higher than the 6th order terms are neglected. Thanks to such an extension of the random output, any desired efficiency of the expected values as well as higher probabilistic moments can be achieved by an appropriate choice of the parameters m and ε corresponding to the input probability density function (PDF) type, relations between the probabilistic moments, acceptable error of the computations etc. This choice can be made by comparative studies with long enough (almost infi-

nite) series Monte-Carlo simulations or theoretical results obtained from the direct symbolic integration. Similar considerations lead to the 6th order expressions for a variance; there holds

$$Var(f) = \int_{-\infty}^{+\infty} \Big(f^0 + \varepsilon \Delta b f^{,b} + \tfrac{1}{2} \varepsilon^2 (\Delta b)^2 f^{,bb} + \tfrac{1}{3!} \varepsilon^3 (\Delta b)^3 f^{,bbb}$$

$$+ \tfrac{1}{4!} \varepsilon^4 (\Delta b)^4 f^{,bbbb} + \tfrac{1}{5!} \varepsilon^5 (\Delta b)^5 f^{,bbbbb} - E[f] \Big)^2 p(f(b)) db. \tag{11}$$

Hence

$$Var(f) \cong \int_{-\infty}^{+\infty} \varepsilon^2 (\Delta b)^2 \big(f^{,b} \big)^2 p(f(b)) db + \int_{-\infty}^{+\infty} \tfrac{1}{4} \varepsilon^4 (\Delta b)^4 \big(f^{,bb} \big)^2 p(f(b)) db$$

$$+ \int_{-\infty}^{+\infty} \varepsilon^4 \Delta b f^{,b} \tfrac{1}{3!} (\Delta b)^3 f^{,bbb} p(f(b)) db + \int_{-\infty}^{+\infty} \varepsilon^4 \Delta b f^{,b} \tfrac{1}{3!} (\Delta b)^3 f^{,bbb} p(f(b)) db$$

$$+ \int_{-\infty}^{+\infty} \tfrac{1}{3!} \varepsilon^6 (\Delta b)^3 f^{,bbb} \tfrac{1}{3!} (\Delta b)^3 f^{,bbb} p(f(b)) db$$

$$+ \int_{-\infty}^{+\infty} \tfrac{1}{4!} \varepsilon^6 (\Delta b)^4 f^{,bbbb} \tfrac{1}{2} (\Delta b)^2 f^{,bb} p(f(b)) db \tag{12}$$

$$+ \int_{-\infty}^{+\infty} \tfrac{1}{4!} \varepsilon^6 (\Delta b)^4 f^{,bbbb} \tfrac{1}{2} (\Delta b)^2 f^{,bb} p(f(b)) db$$

$$+ \int_{-\infty}^{+\infty} \tfrac{1}{5!} \varepsilon^6 (\Delta b)^5 f^{,bbbbb} \Delta b f^{,b} p(f(b)) db$$

$$+ \int_{-\infty}^{+\infty} \tfrac{1}{5!} \varepsilon^6 (\Delta b)^5 f^{,bbbbb} \Delta b f^{,b} p(f(b)) db$$

As it can be recognized here, the first integral corresponds to the second order perturbation, the next three complete 4th order approximation and the rest needs to be included to achieve full 6th order expansion. After multiple integration and indices transformations, one can show that

$$Var(f(b)) = \varepsilon^2 \mu_2(b) f^{,b} f^{,b}$$
$$+ \varepsilon^4 \mu_4(b) \Big(\tfrac{1}{4} f^{,bb} f^{,bb} + \tfrac{2}{3!} f^{,b} f^{,bbb} \Big) \tag{13}$$
$$+ \varepsilon^6 \mu_6(b) \Big(\big(\tfrac{1}{3!} \big)^2 f^{,bbb} f^{,bbb} + \tfrac{1}{4!} f^{,bbbb} f^{,bb} + \tfrac{2}{5!} f^{,bbbbb} f^{,b} \Big).$$

Quite similarly, using the first and the second order terms only, it is possible to derive third order probabilistic moments as

$$
\begin{aligned}
\mu_3(f(b);b) &= \int_{-\infty}^{+\infty}(f(b)-E[f(b)])^3\ p(b)db \\
&= \int_{-\infty}^{+\infty}\left(f^0 + \varepsilon f^{,b}\Delta b + \tfrac{1}{2}\varepsilon^2 f^{,bb}\Delta b\Delta b + ... - E[f(b)]\right)^3 p(b)db \\
&= \int_{-\infty}^{+\infty}\left(\varepsilon f^{,b}\Delta b + \tfrac{1}{2}\varepsilon^2 f^{,bb}\Delta b\Delta b + ...\right)^3 p(b)db \\
&\cong \tfrac{3}{2}\varepsilon^4 \mu_4(b)\left(f^{,b}(b)\right)^2 f^{,bb} + \tfrac{1}{8}\varepsilon^6 \mu_6(b)\left(f^{,bb}\right)^3
\end{aligned}
\tag{14}
$$

and the fourth order probabilistic moment also

$$
\begin{aligned}
\mu_4(f(b);b) &= \int_{-\infty}^{+\infty}(f(b)-E[f(b)])^4\ p(b)db \\
&= \int_{-\infty}^{+\infty}\left(f^0 + \varepsilon f^{,b}\Delta b + \tfrac{1}{2}\varepsilon^2 f^{,bb}\Delta b\Delta b + ... - E[f(b)]\right)^4 p(b)db \\
&= \int_{-\infty}^{+\infty}\left(\varepsilon f^{,b}\Delta b + \tfrac{1}{2}\varepsilon^2 f^{,bb}\Delta b\Delta b + ...\right)^4 p(b)db \\
&\cong \varepsilon^4 \mu_4(b)\left(f^{,b}(b)\right)^4 + \tfrac{3}{2}\varepsilon^6 \mu_6(b)\left(f^{,b}f^{,bb}\right)^2 \\
&\quad + \tfrac{1}{16}\varepsilon^8 \mu_8(b)\left(f^{,b}\right)^3\left(f^{,bb}\right)^4.
\end{aligned}
\tag{15}
$$

Let us mention that it is necessary to multiply each of these equations by the relevant order probabilistic moments of the input random variables to get the algebraic form convenient for any symbolic computations. Because of a great complexity of such a solution, the second order perturbation approach is usually preferred. Recursive derivation of the particular perturbation order equilibrium equations can be powerful in conjunction with symbolic packages with automatic differentiation tools only; it can extend the area of stochastic perturbation technique applications in computational physics and engineering outside the random processes with small dispersion about their expected values. Hence, there is no need to implement directly exact formulas for a particular nth order equations extracted from the perturbation. They can be symbolically generated in the system MAPLE, and next converted to the FORTRAN source codes of the relevant computer software. Finally, it should be emphasized that the random input variables must express here the uncertainty in space or in time, sepa-

rately. Quite analogous expansion may be recalled as a function of the perturbation parameter ε, a perturbation order m as well as the input random variable b

$$
E\big[f(b); b, \varepsilon, m\big] = f^0(b) + \tfrac{1}{2}\varepsilon^2 \frac{\partial^2 f}{\partial b^2}\mu_2(b)
$$
$$
+ \tfrac{1}{4!}\varepsilon^4 \frac{\partial^4 f}{\partial b^4}\mu_4(b) + \tfrac{1}{6!}\varepsilon^6 \frac{\partial^6 f}{\partial b^6}\mu_6(b) + ... + \tfrac{1}{(2m)!}\varepsilon^{2m}\frac{\partial^{2m} f}{\partial b^{2m}}\mu_{2m}(b),
\tag{16}
$$

for any natural m with μ_{2m} being the ordinary probabilistic moment of $2\,m^{\text{th}}$ order.

3. Stochastic dynamics with random parameters

3.1. The single degree-of-freedom case

Let us consider the single-degree-of-freedom dynamical system consisting of a mass m mounted using the spring with the constant k and the dashpot c to the stiff wall and excited by the function $a(\tau)$. The system parameters, i.e. k, c and m are separately defined here as the truncated Gaussian random variables with the specified first two probabilistic moments. Let us assume furthermore that (1) the spring is linear in this system, (2) the excitation is given as $a(\tau) = \hat{a} f(\tau)$, where $f(\tau)$ is a deterministic function of time, while the magnitude is time – independent, (3) the initial conditions are homogenous – $u(0) = 0$ and $\dot{u}(0) = 0$. The general solution to this problem is provided using the Dirac delta distribution, where the forcing function is express in terms of an infinitive sequence of the adjacent impulses with their sampling intervals approach zero; this system response $u(\tau)$ at any time $\tau = t$ is obtained from the superposition of the unit impulse responses

$$
u(t) = \int_0^t a(\tau)w(t-\tau)d\tau = \hat{a}\int_0^t f(\tau)w(t-\tau)d\tau\,,\quad \tau \in [0,T]
\tag{17}
$$

where $w(\tau)$ denotes the response to the Dirac-type excitation $\delta(\tau)$

$$
w(\tau) = w(m,c,k,\tau) = \frac{1}{m\omega_c}\exp(-\xi\omega\tau)\sin\omega_c\tau,\quad \tau \in [0,T],
\tag{18}
$$

where the damped free vibration frequency ω_c, viscous damping factor ξ and natural frequency ω are defined as

$$
\omega_c = \omega(1-\xi^2)^{\frac{1}{2}},\quad \xi = \frac{c}{2m\omega}\,,\quad \omega = \sqrt{\frac{k}{m}}.
\tag{19}
$$

Now we consider the uncertainty in (1) spring stiffness k, (2) the dashpot c and (3) the mass m, separately. Each time we start from the same equation of motion

$$m\ddot{u}(\tau) + c\dot{u}(\tau) + ku(\tau) = \hat{a}f(\tau). \tag{20}$$

For the case (1) we obtain the following hierarchical equations:
0th order:

$$m\ddot{u}^0(\tau) + c\dot{u}^0(\tau) + k^0 u^0(\tau) = \hat{a}f(\tau), \tag{21}$$

1st order:

$$m\ddot{u}^{,k}(\tau) + c\dot{u}^{,k}(\tau) + k^0 u^{,k}(\tau) = -u^0(\tau), \tag{22}$$

2nd order:

$$m\ddot{u}^{,kk}(\tau) + c\dot{u}^{,kk}(\tau) + k^0 u^{,kk}(\tau) = -2u^{,k}(\tau), \tag{23}$$

so for n^{th} order equations one proves easily

$$m\frac{\partial^n \ddot{u}(\tau)}{\partial k^n} + c\frac{\partial^n \dot{u}(\tau)}{\partial k^n} + k^0 \frac{\partial^n u(\tau)}{\partial k^n} = -n\frac{\partial^{n-1} u(\tau)}{\partial k^{n-1}}. \tag{24}$$

Therefore, solving successively those equations one by one and inserting a solution of the previous one into the R.H.S. of the partial differential equation it is possible to collect all components for probabilistic moments expressions for $u(\tau)$, $\dot{u}(\tau)$ and $\ddot{u}(\tau)$. The two remaining case studies return very similar results, so that when c is randomized then the first order equations equals to

$$m\ddot{u}^{,c}(\tau) + c^0 \dot{u}^{,c}(\tau) + ku^{,c}(\tau) = -\dot{u}^0(\tau), \tag{25}$$

whereas the recursive relation of the nth order is equal to

$$m\frac{\partial^n \ddot{u}(\tau)}{\partial c^n} + c^0 \frac{\partial^n \dot{u}(\tau)}{\partial c^n} + k\frac{\partial^n u(\tau)}{\partial c^n} = -n\frac{\partial^{n-1} \dot{u}(\tau)}{\partial c^{n-1}}. \tag{26}$$

3.2. The general elastodynamic problem with random parameters

Let us consider the following set of partial differential equations adequate to the linear elastodynamic problem [2, 5] consisting of

- the equations of motion

$$\mathbf{D}^{\mathbf{T}}\boldsymbol{\sigma} + \hat{\mathbf{f}} = \rho\ddot{\mathbf{u}}, \quad \mathbf{x} \in \Omega, \quad \tau \in [t_0, \infty), \tag{27}$$

- the constitutive equations

$$\boldsymbol{\sigma} = \mathbf{C}\boldsymbol{\varepsilon}, \quad \mathbf{x} \in \Omega, \quad \tau \in [t_0, \infty), \tag{28}$$

- the geometric equations

$$\boldsymbol{\varepsilon} = \mathbf{D}\mathbf{u}, \quad \mathbf{x} \in \Omega, \quad \tau \in [t_0, \infty), \tag{29}$$

- the displacement boundary conditions

$$\mathbf{u} = \hat{\mathbf{u}}, \quad \mathbf{x} \in \partial\Omega_u, \quad \tau \in [t_0, \infty), \tag{30}$$

- the stress boundary conditions

$$\mathbf{N}\boldsymbol{\sigma} = \hat{\mathbf{t}}, \quad \mathbf{x} \in \partial\Omega_\sigma, \quad \tau \in [t_0, \infty), \tag{31}$$

- the initial conditions

$$\mathbf{u} = \hat{\mathbf{u}}^{\mathbf{0}}, \quad \dot{\mathbf{u}} = \hat{\dot{\mathbf{u}}}^{\mathbf{0}}, \quad \tau \in [t_0, \infty). \tag{32}$$

It is assumed that all the state functions appearing in this system are sufficiently smooth functions of the independent variables $\mathbf{x}$ and τ. Let us consider the variation $\mathbf{u}(\mathbf{x}, \tau)$ in some time moment $\tau = t$ denoted by $\delta\mathbf{u}(\mathbf{x}, \tau)$. Using the above equations one can show that

$$-\int_\Omega (\mathbf{D}^{\mathbf{T}}\boldsymbol{\sigma} + \hat{\mathbf{f}} - \rho\ddot{\mathbf{u}})^{\mathbf{T}}\delta\mathbf{u}\,d\Omega + \int_{\partial\Omega_\sigma} (\mathbf{N}\boldsymbol{\sigma} - \hat{\mathbf{t}})^{\mathbf{T}}\delta\mathbf{u}\,d(\partial\Omega) = 0. \tag{33}$$

Assuming further that the displacement function $u(x, t)$ has known values at the initial moment $\mathbf{u}(\mathbf{x}, t_1) = 0$ and at the end of the process $\mathbf{u}(\mathbf{x}, t_2) = 0$, so that the variations of this function also equal 0 at those time moments

$$\delta\mathbf{u}(\mathbf{x}, t_1) = 0, \ \delta\mathbf{u}(\mathbf{x}, t_2) = 0. \tag{34}$$

Integrating by parts with respect to the variables $\mathbf{x}$ and τ we can obtain that

$$\int_{t_1}^{t_2} [\delta\mathbf{T} - \int_\Omega \boldsymbol{\sigma}^{\mathbf{T}}\delta\boldsymbol{\varepsilon}\,d\Omega + \int_\Omega \hat{\mathbf{f}}^{\mathbf{T}}\delta\mathbf{u}\,d\Omega + \int_{\partial\Omega} \hat{\mathbf{t}}^{\mathbf{T}}\delta\mathbf{u}\,d(\partial\Omega)]d\tau = 0, \tag{35}$$

where the kinetic energy of the region Ω is defined as

$$T = \frac{1}{2} \int \rho \dot{\mathbf{u}}^{\mathrm{T}} \dot{\mathbf{u}} \, d\Omega. \tag{36}$$

Equation (35) is considered together with the following strain relation

$$\delta \boldsymbol{\varepsilon} = \mathbf{D} \delta \mathbf{u}, \; \mathbf{x} \in \Omega, \; \tau \in [t_0, \infty). \tag{37}$$

Next, we introduce the assumption that the mass forces $\hat{\mathbf{f}}$ and the surface loadings $\hat{\mathbf{t}}$ are independent from the displacement vector $\mathbf{u}$, which means that the external loadings do not follow the changes in the domain initial configuration. Therefore, Equation (35) can be modified to the following statement:

$$\delta \int_{\mathbf{t}_1}^{\mathbf{t}_2} \left(T - J_p \right) d\tau = 0, \tag{38}$$

where $\mathbf{J}_p$ means the potential energy cumulated in the domain Ω

$$J_{\mathbf{p}} = U - \int_{\boldsymbol{\Omega}} \hat{\mathbf{f}}^{\mathrm{T}} \mathbf{u} \, d\Omega - \int_{\partial \boldsymbol{\Omega}_{\boldsymbol{\sigma}}} \hat{\mathbf{t}}^{\mathrm{T}} \mathbf{u} \, d(\partial \Omega) = 0, \tag{39}$$

whereas the variation is determined with respect to the displacement function and $\mathbf{U}$ is the elastic strain energy given by the formula

$$U = \tfrac{1}{2} \int_{\Omega} \boldsymbol{\varepsilon}^{\mathrm{T}} \mathbf{C} \boldsymbol{\varepsilon} \, d\Omega. \tag{40}$$

It is well known that Equation (38) represents the Hamilton principle widely used in structural dynamics in conjunction with the Finite Element Method approach.

3.3. The generalized perturbation-based eigenvalue problem

Let us consider a deterministic eigenproblem in its matrix description for its further stochastic expansion

$$(\mathbf{K} - \varpi^2 \mathbf{M}) \boldsymbol{\varphi} = \mathbf{0}. \tag{41}$$

Its zeroth order version looks like

$$(\mathbf{K}^0 - (\varpi^0)^2 \mathbf{M}^0) \boldsymbol{\varphi}^0 = 0, \tag{42}$$

whereas the first order equation has the following form:

$$\left(\mathbf{K}^{\prime b} - \frac{d}{db}(\varpi^0)^2 \mathbf{M}^0 - (\varpi^0)^2 \mathbf{M}^{\prime b}\right)\boldsymbol{\varphi}^0 = -(\mathbf{K}^0 - (\varpi^0)^2 \mathbf{M}^0)\boldsymbol{\varphi}^{\prime b}. \tag{43}$$

After some algebraic transformation one can get that

$$(\mathbf{K}^{\prime b} - 2\varpi^0\varpi^{\prime b}\mathbf{M}^0 - (\varpi^0)^2\mathbf{M}^{\prime b})\boldsymbol{\varphi}^0 = -(\mathbf{K}^0 - (\varpi^0)^2\mathbf{M}^0)\boldsymbol{\varphi}^{\prime b}, \tag{44}$$

which finally takes the following form:

$$\mathbf{K}^{\prime b}\boldsymbol{\varphi}^0 - 2\varpi^0\varpi^{\prime b}\mathbf{M}^0\boldsymbol{\varphi}^0 - (\varpi^0)^2\mathbf{M}^{\prime b}\boldsymbol{\varphi}^0 + \mathbf{K}^0\boldsymbol{\varphi}^{\prime b} - (\varpi^0)^2\mathbf{M}^0\boldsymbol{\varphi}^{\prime b} = 0. \tag{45}$$

As it was expected, the perturbed first order equation is much more complicated than the first order equation in the linear elastostatics. The next differentiation of Equation (44) with respect to the input random variable b gives

$$(\mathbf{K}^{\prime bb} - \frac{\partial}{\partial b}(2\varpi^0\varpi^{\prime b}\mathbf{M}^0) - \frac{\partial}{\partial b}((\varpi^0)^2\mathbf{M}^{\prime b})\boldsymbol{\varphi}^0 +$$
$$(\mathbf{K}^{\prime b} - 2\varpi^0\varpi^{\prime b}\mathbf{M}^0 - (\varpi^0)^2\mathbf{M}^{\prime b})\boldsymbol{\varphi}^{\prime b} = \tag{46}$$
$$= -(\mathbf{K}^{\prime b} - 2\varpi^0\varpi^{\prime b}\mathbf{M}^0 - (\varpi^0)^2\mathbf{M}^{\prime b})\boldsymbol{\varphi}^{\prime b} - (\mathbf{K}^0 - (\varpi^0)^2\mathbf{M}^0)\boldsymbol{\varphi}^{\prime bb}.$$

After its simplification we obtain

$$\mathbf{K}^{\prime bb}\boldsymbol{\varphi}^0 + \mathbf{K}^{\prime b}\boldsymbol{\varphi}^{\prime b} - \frac{\partial}{\partial b}(2\varpi^0)\varpi^{\prime b}\mathbf{M}^0\boldsymbol{\varphi}^0 - 2\varpi^0\varpi^{\prime bb}\mathbf{M}^0\boldsymbol{\varphi}^0$$

$$- 2\varpi^0\varpi^{\prime b}\mathbf{M}^{\prime b}\boldsymbol{\varphi}^0 - 2\varpi^0\varpi^{\prime b}\mathbf{M}^0\boldsymbol{\varphi}^{\prime b} - \frac{\partial}{\partial b}((\varpi^0)^2)\mathbf{M}^{\prime b}\boldsymbol{\varphi}^0 \tag{47}$$

$$- (\varpi^0)^2\mathbf{M}^{\prime bb}\boldsymbol{\varphi}^0 - (\varpi^0)^2\mathbf{M}^{\prime b}\boldsymbol{\varphi}^{\prime b} + \mathbf{K}^{\prime b}\boldsymbol{\varphi}^{\prime b} + \mathbf{K}^0\boldsymbol{\varphi}^{\prime bb}$$

$$- \frac{\partial}{\partial b}((\varpi^0)^2)\mathbf{M}^0\boldsymbol{\varphi}^{\prime b} + (\varpi^0)^2\mathbf{M}^{\prime b}\boldsymbol{\varphi}^{\prime b} - (\varpi^0)^2\mathbf{M}^0\boldsymbol{\varphi}^{\prime bb} = 0$$

Finally, one can show that the second order equation is equal to

$$\mathbf{K}^{\prime bb}\boldsymbol{\varphi}^0 + 2K^{\prime b}\boldsymbol{\varphi}^{\prime b} + \mathbf{K}^0\boldsymbol{\varphi}^{\prime bb} - 2\varpi^0(\varpi^{\prime b})^2\mathbf{M}^0\boldsymbol{\varphi}^0 - 2\varpi^0\varpi^{\prime bb}\mathbf{M}^0\boldsymbol{\varphi}^0$$
$$- 4\varpi^0\varpi^{\prime b}(\mathbf{M}^{\prime b}\boldsymbol{\varphi}^0 + \mathbf{M}^0\boldsymbol{\varphi}^{\prime b}) - (\varpi^0)^2(\mathbf{M}^{\prime bb}\boldsymbol{\varphi}^0 + 2\mathbf{M}^{\prime b}\boldsymbol{\varphi}^{\prime b} + \mathbf{M}^0\boldsymbol{\varphi}^{\prime bb}) = 0. \tag{48}$$

It is quite clear here that the generalized version of the stochastic perturbation technique based on the nth order Taylor series expansion may lead to the very complex

equation corresponding to the highest order closure of the entire system [3, 4]. The left hand side of this equation denoted by *LHS(n)* should be equal to

$$LHS(n) = \sum_{k=0}^{n} \binom{n}{k} k^{(n-k)} \boldsymbol{\varphi}^{(k)}, \tag{49}$$

where obviously

$$\boldsymbol{\varphi}^{(k)} = \frac{\partial^k \boldsymbol{\varphi}}{\partial b^k}. \tag{50}$$

An application of the similar nth order differentiation procedure to the right hand side of zeroth order statement results in

$$RHS(n) = \sum_{k=0}^{n} \binom{n}{k} (\varpi^2)^{(k)} \sum_{m=0}^{n-k} \binom{n-k}{m} \mathbf{M}^{(m)} \boldsymbol{\varphi}^{(n-k-m)}. \tag{51}$$

Therefore, the remaining issue is to give a formula for the *k*-th order partial derivative of the eigenvalues second with respect to the input random variable. There holds

$$(\varpi^2)^{(k+1)} = \frac{\partial^{k+1}}{\partial b^{k+1}} (\varpi^2) = \frac{\partial^k}{\partial b^k} (2\varpi \cdot \frac{\partial \varpi}{\partial b}) = \sum_{l=0}^{k} \binom{n}{l} (2\varpi)^{(k-l)} (\frac{\partial \varpi}{\partial b})^{(k)}. \tag{52}$$

Therefore, one can easily get

$$(\varpi^2)^{(k)} = \sum_{l=0}^{k-1} \binom{k-1}{l} (2\varpi)^{(k-(l-1))} \varpi^{(l+1)}. \tag{53}$$

Hence, the Equation (51) may be rewritten in a form

$$RHS(n) = \sum_{k=0}^{n} \binom{n}{k} \sum_{l=0}^{k-1} \binom{k-1}{l} (2\varpi)^{(k-(l+1))} \cdot \varpi^{(l+1)} \sum_{m=0}^{n-k} \binom{n-k}{m} \mathbf{M}^{(m)} \boldsymbol{\varphi}^{(n-k-m)}. \tag{54}$$

A comparison of the Relations (49) and (54) returns

$$\sum_{k=0}^{n} \binom{n}{k} \mathbf{K}^{(n-k)} \boldsymbol{\varphi}^k = \sum_{k=0}^{n} \binom{n}{k} \sum_{l=0}^{k-1} \binom{k-1}{l} (2\varpi)^{(k-(l+1))} \cdot \varpi^{(l+1)} \sum_{m=0}^{n-k} \binom{n-k}{m} \mathbf{M}^{(m)} \boldsymbol{\varphi}^{(n-k-m)}. \tag{55}$$

A solution to his equation makes it possible to determine up to the nth order eigenvalues together with the corresponding eigenvectors.

4. Computational implementation

Let us consider a discretization of the displacement field $\mathbf{u}(\mathbf{x}, \tau)$ using the following forms [2, 5]:

$$\mathbf{u}^{\alpha}_{3x1}(\mathbf{x}, \tau) \cong \varphi_{3\,xN_{(e)}}(\mathbf{x})\,\mathbf{q}^{\alpha}_{N_{(e)}x1}(\tau), \; \mathbf{u}^{\alpha}_{3x1}(\mathbf{x}, \tau) \cong \mathbf{\Phi}_{3\,xN}(\mathbf{x})\mathbf{r}^{\alpha}_{Nx1}(\tau), \tag{56}$$

where:
  $\mathbf{q}$ is a vector of the generalized coordinates for the considered finite element,
  $\mathbf{r}$ is a vector for the generalized coordinates of the entire discretized system,
  $N(e)$ is the total number of the finite element degrees of freedom,
  N is the total number of degrees of freedom in the structure model,
  φ and $\mathbf{\Phi}$ are the corresponding the shape function matrices (local and global).

The generalized coordinates vector for the entire structure model and for the final element are related by the transformation matrix as

$$\mathbf{r}^{\alpha}_{Nx1} = a_{NxN_{(e)}}\mathbf{q}^{\alpha}_{N_{(e)}x1}. \tag{57}$$

Contrary to the classical formulations of both FEM and the perturbation-based Stochastic Finite Element Method we introduce here the additional index $\alpha = 1, ..., M$ to distinguish between different solutions of the elastodynamic problem obtained to build up the response function around the mean value of the input random parameter. Therefore, the strain tensor can be expressed as

$$\varepsilon^{\alpha}_{6x1}(\mathbf{x}, \tau) = B_{6xN(e)}(\mathbf{x})\mathbf{q}^{\alpha}_{N(e)x1}(\tau) = \widetilde{B}_{6\,xN}(\mathbf{x})\mathbf{r}^{\alpha}_{Nx1}(\tau). \tag{58}$$

Application of those relations to the Hamilton principle in Equation (38) leads to the statement

$$\delta\int_{t_1}^{t_2}\left(\frac{1}{2}\sum_{l=1}^{E}\mathbf{q}^{\alpha T}\mathbf{m}^{\alpha}\mathbf{q}^{\alpha} - \frac{1}{2}\sum_{e=1}^{E}\mathbf{q}^{\alpha T}\mathbf{k}^{\alpha}\mathbf{q}^{\alpha} + \sum_{e=1}^{E}\mathbf{Q}^{\alpha T}\mathbf{q}^{\alpha}\right)d\tau = 0, \tag{59}$$

so that the global notation gives here

$$\delta\int_{t_1}^{t_2}\left(\frac{1}{2}\dot{\mathbf{r}}^{\alpha T}\mathbf{M}^{\alpha}\dot{\mathbf{r}}^{\alpha} - \frac{1}{2}\mathbf{r}^{\alpha T}\mathbf{K}^{\alpha}\mathbf{r}^{\alpha} + \mathbf{R}^{\alpha T}\mathbf{r}^{\alpha}\right)d\tau = 0. \tag{60}$$

The element and global mass matrices are defined as

$$\mathbf{m}^{\alpha}_{N_{(e)}xN_{(e)}} = \int_{\Omega_e}\rho^{\alpha}(\mathbf{x})\mathbf{B}^{T}_{N_{(e)}x6}(\mathbf{x})\mathbf{B}_{6xN_{(e)}}(\mathbf{x})d\Omega \tag{61}$$

and

$$\mathbf{M}_{NxN}^{\alpha} = \int_{\Omega} \rho^{\alpha}(\mathbf{x})\widetilde{\mathbf{B}}_{Nx6}^{T}(\mathbf{x})\widetilde{\mathbf{B}}_{6xN}(\mathbf{x})\,\mathrm{d}\Omega. \tag{62}$$

The stiffness matrices at the element and at the global scales are defined as follows

$$\mathbf{k}_{N_{(e)}xN_{(e)}}^{\alpha} = \int_{\Omega_{(e)}} \mathbf{B}_{N_{(e)}x6}^{T}\mathbf{C}_{6x6}^{\alpha}\mathbf{B}_{6xN_{(e)}}\,\mathrm{d}\Omega \tag{63}$$

and

$$\mathbf{K}_{NxN}^{\alpha} = \int_{\Omega_{(e)}} \widetilde{\mathbf{B}}_{Nx6}^{T}\mathbf{C}_{6x6}^{\alpha}\widetilde{\mathbf{B}}_{6xN}\,\mathrm{d}\Omega, \tag{64}$$

the vector $\mathbf{R}\,(\mathbf{x},\,\tau)$ represents the vector of nodal loadings. The time variation over Equation (59) results in a relation

$$\dot{\mathbf{r}}^{\mathbf{T}}\mathbf{M}\,\delta\mathbf{r} - \int_{t_1}^{t_2}(\ddot{\mathbf{r}}^{\mathbf{T}}\mathbf{M} + \mathbf{r}^{\mathbf{T}}\mathbf{K} - \mathbf{R}^{\mathbf{T}})\delta\mathbf{r}\,\mathrm{d}\tau = 0. \tag{65}$$

Considering the assumptions that

$$\delta\mathbf{r}(t_1) = 0,\, \delta\mathbf{r}(t_2) = 0, \tag{66}$$

we finally obtain the dynamic equilibrium system

$$\mathbf{M}^{\alpha}\ddot{\mathbf{r}}^{\alpha} + \mathbf{K}^{\alpha}\mathbf{r}^{\alpha} = \mathbf{R}^{\alpha}, \tag{67}$$

which represents the equations of motion of the discretized system. When we complete this equation with the component $\mathbf{C}_{NxN}^{\alpha}\mathbf{r}_{Nx1}^{\alpha}$ getting

$$\mathbf{M}^{\alpha}\ddot{\mathbf{r}}^{\alpha} + \mathbf{C}^{\varepsilon}\dot{\mathbf{r}}^{\alpha} + \mathbf{K}^{\alpha}\mathbf{r}^{\alpha} = \mathbf{R}^{\alpha}, \tag{68}$$

then we receive the equations system corresponding to the system with nonzero damping; it is frequently defined as

$$\mathbf{C}^{\alpha} = \alpha_0\mathbf{M}^{\alpha} + \alpha_1\mathbf{K}^{\alpha}, \tag{69}$$

where the coefficients α_0 and α_1 are determined using the specific eigenfunctions for this problem, so that

$$\mathbf{M}^\alpha \ddot{\mathbf{r}}^\alpha + \alpha_0 \mathbf{M}^\alpha \dot{\mathbf{r}}^\alpha + \alpha_1 \mathbf{K}^\alpha \dot{\mathbf{r}}^\alpha + \mathbf{K}^\alpha \mathbf{r}^\alpha = \mathbf{R}^\alpha, \tag{70}$$

where no summation over the doubled indices α is applied here. As it is known, the case of undamped and free vibrations leads to the system

$$\mathbf{M}^\alpha \ddot{\mathbf{r}}^\alpha + \mathbf{K}^\alpha \mathbf{r}^\alpha = \mathbf{0}, \tag{71}$$

and the solution $\mathbf{r}^\alpha = \mathbf{A}^\alpha \sin \omega_\alpha t$ leads to the relation

$$-\mathbf{M}^\alpha \mathbf{A}^\alpha \omega_\alpha^2 \sin \omega_\alpha t + \mathbf{K}^\alpha \mathbf{A}^\alpha \sin \omega_\alpha t = \mathbf{0}, \tag{72}$$

so that for $\sin \omega_\alpha t \neq \mathbf{0}$ and $\mathbf{A}^\alpha \neq \mathbf{0}$ there holds

$$-\mathbf{M}^\alpha \omega_\alpha^2 + \mathbf{K}^\alpha = \mathbf{0}. \tag{73}$$

When the index α is postponed, then the stochastic problem is solved in a straight-forward manner analogously to the previous methods and the methodology follows the successive solutions of the increasing order equations proposed in Section 3.3.

As shown during derivation of equations for the generalized perturbation based approach, one of the most complicated issues is numerical determination of up to nth order partial derivatives of the structural response function with respect to the randomized parameter. It is possible to determine this function first by multiple solutions of the boundary value problem around the expectation of the random parameter to complete this task. The response function for each eigenvalue is built up from uniform symmetric discretization in the neighborhood of this expectation, with equidistant intervals. A set of classical deterministic re-computations of the all the components of the eigenvalues vector leads to the final formation of the responses function for all ω_α. That is why we consider further a problem of the unknown response function approximation by the following polynomial of $n - 1$ order:

$$\omega_\alpha = A_1^{(\alpha)} b^{n-1} + A_2^{(\alpha)} b^{n-2} + ... + A_n^{(\alpha)} b^0, \tag{74}$$

having the values of this function determined computationally for n different arguments. With this representation, the algebraic system of equations is formed

$$\begin{cases} A_1^{(\alpha)} b_1^{n-1} + A_2^{(\alpha)} b_1^{n-2} + ... + A_n^{(\alpha)} b_1^0 = \omega_{\alpha(1)} \\ A_1^{(\alpha)} b_2^{n-1} + A_2^{(\alpha)} b_2^{n-2} + ... + A_n^{(\alpha)} b_2^0 = \omega_{\alpha(2)} \\ \qquad\qquad ... \\ A_1^{(\alpha)} b_n^{n-1} + A_2^{(\alpha)} b_n^{n-2} + ... + A_n^{(\alpha)} b_n^0 = \omega_{\alpha(n)} \end{cases}, \tag{75}$$

where the coefficients $\omega_{\alpha(i)}$ for $i = 1, ..., n$ denote the approximated function values in ascending order of the arguments b_i.

Therefore, the following algebraic system of equations is formed to determine the polynomial coefficients $A_i^{\alpha\beta\gamma\delta}$:

$$
\begin{bmatrix}
b_1^{n-1} & b_1^{n-2} & ... & b_1^0 \\
b_2^{n-1} & b_2^{n-2} & & b_2^0 \\
... & ... & & ... \\
b_n^{n-1} & b_n^{n-2} & ... & b_n^0
\end{bmatrix}
\begin{Bmatrix}
A_1^{(\alpha)} \\
A_2^{(\alpha)} \\
... \\
A_n^{(\alpha)}
\end{Bmatrix}
=
\begin{Bmatrix}
\omega_{\alpha(1)} \\
\omega_{\alpha(2)} \\
... \\
\omega_{\alpha(n)}
\end{Bmatrix}.
\tag{76}
$$

The crucial point of this method is a proper determination of the set of input parameters $\{b_1^0, ..., b_n^0\}$ inserted into this equation. This determination is started with a choice of the computational domain $[b - \Delta b, b + \Delta b]$, where $2\Delta b = 0.05b$. Then, this domain is subdivided into the set of equidistant $n - 1$ intervals with the length $\Delta b_{(m,m+1)} = \dfrac{2\Delta b}{n-1}$ for any $m = 1, ..., n-1$.

So, that assuming that $b_0 = b - \Delta b$ it is obtained that $b_m = b - \Delta b + m\dfrac{2\Delta b}{n-1}$. Let us note that since this linear system of equations is non-symmetric, its solution cannot be done by the integration with the FEM solver, and some separate numerical procedure based on the Gauss–Jordan elimination scheme must be employed. The unique solution for this system makes it possible to calculate up to the nth order ordinary derivatives of the homogenized elasticity tensor with respect to the parameter b at the given b_0 as

1st order derivative:

$$
\frac{\partial \omega_\alpha}{\partial b} = (n-1)A_1^{(\alpha)}b^{n-2} + (n-2)A_2^{(\alpha)}b^{n-3} + ... + A_{n-1}^{(\alpha)},
\tag{77}
$$

2nd order derivative:

$$
\frac{\partial^2 \omega_\alpha}{\partial b^2} = (n-1)(n-2)A_1^{(\alpha)}b^{n-3} + (n-2)(n-3)A_2^{(\alpha)}b^{n-4} + ... + A_{n-2}^{(\alpha)},
\tag{78}
$$

kth order derivative:

$$
\frac{\partial^k \omega_\alpha}{\partial b^k} = \prod_{i=1}^{k}(n-i)A_1^{(\alpha)}b^{n-k} + \prod_{i=2}^{k}(n-i)A_2^{(\alpha)}b^{n-(k+1)} + ... + A_{n-k}^{(\alpha)}.
\tag{79}
$$

Providing that the response function of the structural eigenvalue has a single independent argument, that is, the input random variable of the problem, it is possible to employ the stochastic perturbation technique based on the Taylor representation to compute up to the m'-th order probabilistic moments $\mu_m(\omega_a)$. It is clear from the derivation above that to complete the m'-th order approximation we need to solve the initial deterministic problem m times, with its number of degrees of freedom and a single system of algebraic equations $m \times m$, to find a single response function. Including the formulas above for the derivatives of the response function in a definition of the probabilistic moments, one can determine the expectations, variances as well as any order random characteristics of the structural response.

5. Numerical experiments

5.1. The single-degree-of-freedom system with random parameters

The first computational example is devoted to the 1 D.O.F. system without the damping. The mass m and the spring stiffness k are separately considered as the Gaussian random variables with the expected values equal to E[k] = 24E6 and E[m] = 1000. Their coefficients of variations belong to the interval [0.0, 0.3] and sometimes are limited for a more transparent results presentation to the narrower interval [0.1, 0.2]. All the equations and computer visualization has been prepared using the symbolic computations system MAPLE, v.11. Using the methodology described above consisting of the straightforward differentiation approach and the well-known classical formula we study here:

1. The expected values for (a) randomized spring stiffness (all the diagrams at the left) and (b) randomized mass (the right diagrams) computed according to the 2nd, 4th, 6th, 8th and 10th order approaches Figure 1;
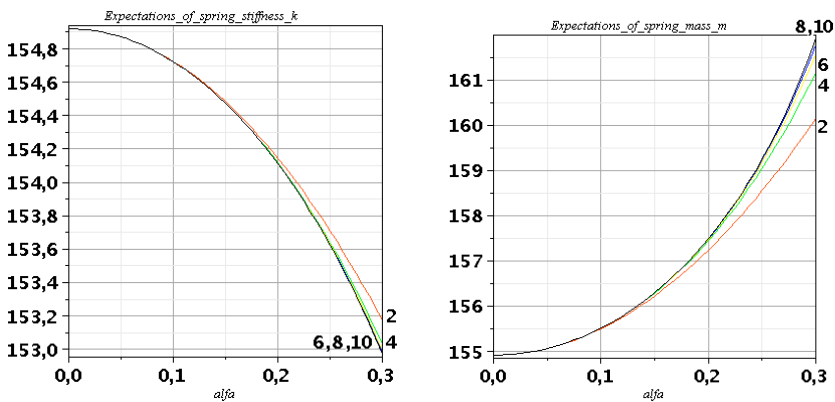
Fig. 1. The expected values for the 1 D.O.F. eigenvalue for the random stiffness (left)
and the random mass (right)

2. The variances for (a) the perturbation parameter variability $\varepsilon \in [0.8, 1.2]$ – Figure 2 and (b) for the perturbation parameter arbitrarily defined as $\varepsilon = 1$ – Figure 3 (according to the 2nd, 4th and 6th order methods); the lowest surface on Figure 2 corresponds to the 2nd order results, the intermediate surface results from the 4th order approach and the upper surface is equivalent to the results of the 6th order analysis; Figure 3 contains the solid lines (2nd order analysis), the dot line for the 4th order method and dash-dot line for the 6th order approach;
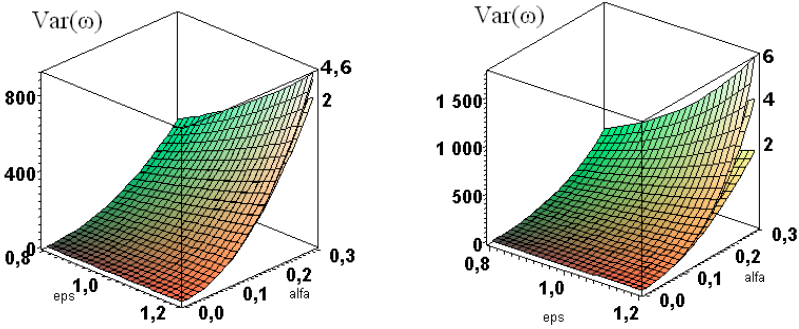
Fig. 2. The variances for the 1 D.O.F. eigenvalue for the random stiffness (left)
and the random mass (right)
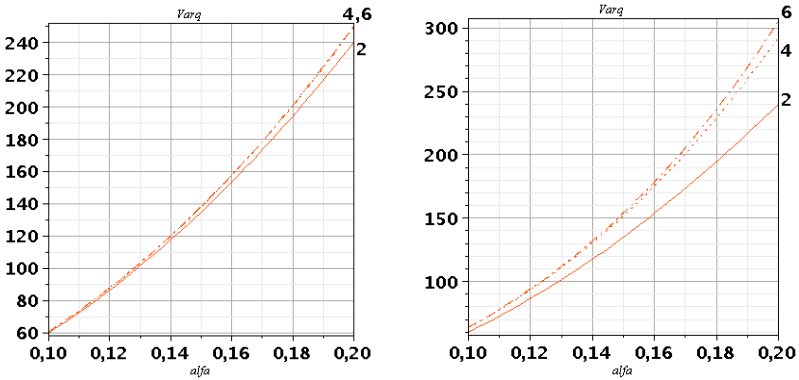
Fig. 3. The variances for the 1 D.O.F. eigenvalue for the random stiffness (left)
and the random mass (right) [$\varepsilon = 1$]

3. The standard deviations for (a) the perturbation parameter variability $\varepsilon \in [0.8, 1.2]$ – Figure 4 and (b) for the perturbation parameter arbitrarily defined as $\varepsilon = 1$ – Figure 5 (according to the 2nd, 4th and 6th order methods); the data presentation is exact the same like in Figures 2 and 3;

4. The lowest order approximation of the third central probabilistic moments as the function of both perturbation parameter and the input coefficient of variation varying as before – see Figure 6;

5. The lowest order approximation of the fourth central probabilistic moments as the function of both perturbation parameter and the input coefficient of variation varying as before – in Figure 7.
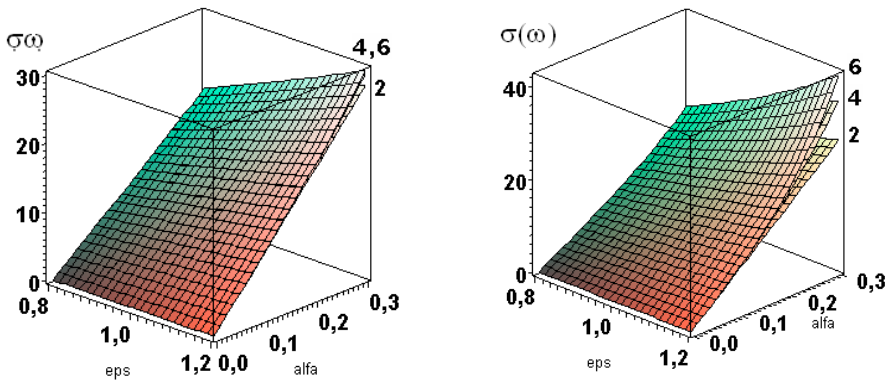
Fig. 4. The standard deviations for the 1 D.O.F. eigenvalue for the random stiffness (left)
and the random mass (right)
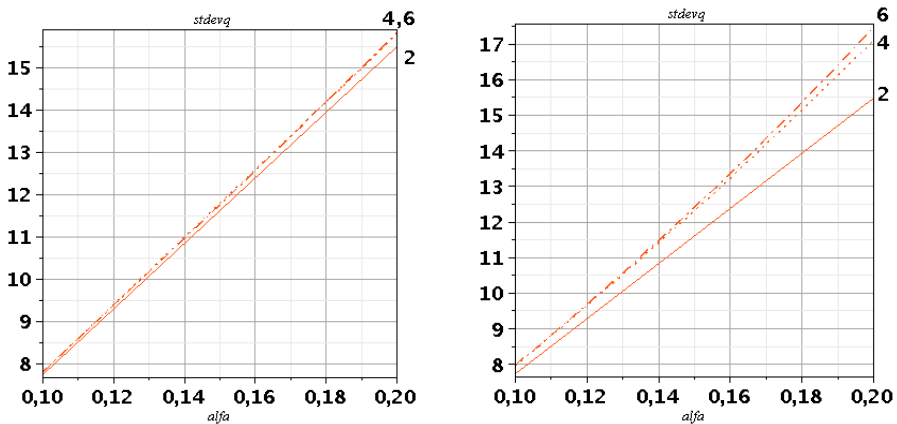
Fig. 5. The standard deviations for the 1 D.O.F. eigenvalue for the random stiffness (left)
and the random mass (right)

The expected values shown in Figure 1 nonlinearly decrease together with an increase of the input coefficient of variation of the spring stiffness and systematically and monotonously increase together with an increase of the input coefficient of variation of the random mass. Those changes become more transparent for each next order of the perturbation analysis, however the differences between the neighboring
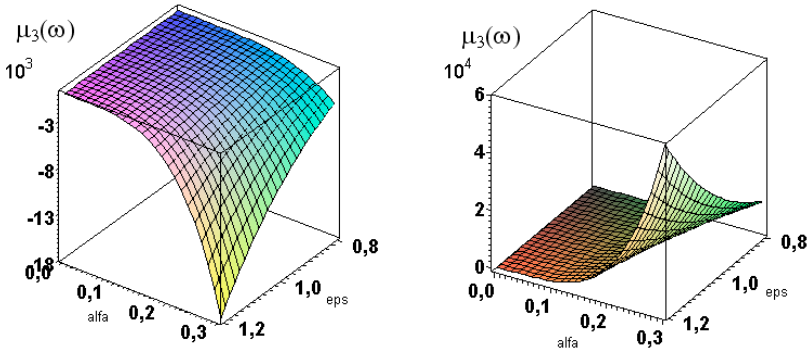
Fig. 6. The third central probabilistic moments for the 1 D.O.F. eigenvalue
for the random stiffness (left) and the random mass (right)
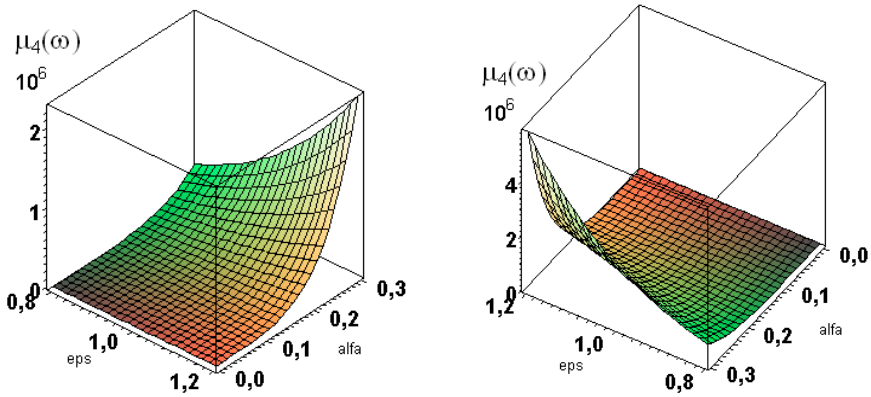
Fig. 7. The fourth central probabilistic moments for the 1 D.O.F. eigenvalue
for the random stiffness (left) and the random mass (right)

stochastic expansion orders systematically vanish. It means that the proposed tech-
nique based on the stochastic perturbation analysis the Response Function Method
converges rather fast even for the very large random dispersion of the input variable as
0.3 in this figure. The variances showed in Figure 3 shows a little different character –
as one may expect both variances increase monotonously together with an increase of
the input coefficient of variation. Those increases become larger together with the
perturbation order taken in the analysis and, as before, the differences between the
neighboring orders systematically decrease, however not so fast as in the case of the
expectations. Figure 2 brings the information about both variances two-parametric
behavior including the perturbation parameter changes. All the three surfaces corre-
sponding to the 2nd, 4th and 6th order computations show that the larger perturbation
parameter the larger final value of the variance. The only exception is obtained when
the input coefficient of variation equals 0 but this is the limiting deterministic case,

when the perturbation does not matter at all. Let us note that the differences between the neighboring orders are larger for the randomized mass than for the randomized spring stiffness. Analogous observations can be drawn for the standard deviations shown in Figures 4 and 5 quite similarly to the presentation of the variances in Figures 2 and 3, accordingly. The only difference is that the standard deviations do not change so nonlinearly as the variances before. The essential changes are observed for the third central probabilistic moments (Figure 6), where the spring stiffness results in the negative values and the randomized mass of the system gives the positive values. Therefore, the probability density function of the system eigenvalue is non-symmetric in both cases and demonstrates negative skewness for the spring stiffness (more probability mass below the expected value) and the positive skewness for the random mass. The absolute values of the third moments for the randomized mass are about two times larger than for the random spring stiffness. The last figure shows the fourth central probabilistic moments, where their values monotonously and nonlinearly increase together with the increases of the perturbation parameter and the input coefficient of variation. Contrary to the previous case, the fourth central moment must be positive everywhere, but similarly to the third moments, the values obtained for the random mass as twice as much as those computed for the randomized spring stiffness. Finally, let us note that we can easily extract from Figures 6 and 7 the coefficients of asymmetry and kurtosis for probability density functions of the eigenvalue by dividing them by the third and fourth powers of the standard deviations, accordingly. Then, the comparison with the Gaussian probability density function would be more transparent.

5.2. The elastic 3D truss structure

Computational analysis has been tested on the example of the telecommunication tower given schematically in Figure 8 with the height equal to 5.0 meters.
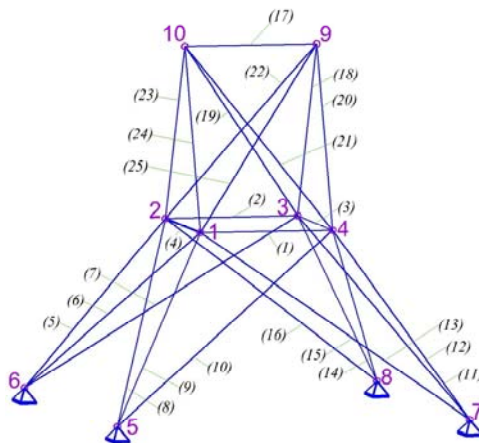
Fig. 8. Structural scheme of the transmission tower

Table 1. Input data for the particular structural members

Element no.	Cross-sectional area [m^2]	Mass density [kg/m]
1	6.450E–06	1.780E–02
2	9.030E–06	2.500E–02
3	6.450E–06	1.780E–02
4	9.030E–06	2.500E–02
5	6.322E–04	1.750E+00
6	1.135E–03	3.143E+00
7	1.574E–03	4.357E+00
8	6.322E–04	1.750E+00
9	1.135E–03	3.143E+00
10	1.574E–03	4.357E+00
11	6.322E–04	1.750E+00
12	1.135E–03	3.143E+00
13	1.574E–03	4.357E+00
14	6.322E–04	1.750E+00
15	1.135E–03	3.143E+00
16	1.574E–03	4.357E+00
17	2.129E–05	5.890E–02
18	1.300E–03	3.598E+00
19	1.821E–03	5.041E+00
20	1.300E–03	3.598E+00
21	1.821E–03	5.041E+00
22	1.300E–03	3.598E+00
23	1.821E–03	5.041E+00
24	1.300E–03	3.598E+00
25	1.821E–03	5.041E+00

The entire structures has been discretized using the two-noded 25 linear space structure finite elements (3D truss elements) joined in 10 nodal points. All the structural members have been manufactured with the stainless steel with Young modulus equal to $E = 210$ GPa. The cross-sectional areas and mass densities for all those members have been collected in Table 1.

Table 2a. Probabilistic moments of the eigenvalues for the telecommunication tower for the randomized Young modulus

Eigenvalue number	The expected values (2)	3rd order moments	4th order moments
1	22.063E5	–0.076E11	0.521E16
2	34.377E5	–0.180E11	0.308E17
3	70.148E5	–0.196E12	0.532E18
4	75.312E5	–0.264E12	0.710E18
5	95.066E5	–0.805E12	0.180E19
6	114.884E5	–0.990E12	0.388E19
7	136.843E5	–0.626E12	0.773E19
8	152.818E5	–0.290E13	0.120E20
9	157.610E5	–0.439E13	0.143E20
10	226.452E5	–0.851E15	0.243E21

Two groups of numerical tests have been performed (a) with randomized Young modulus of the tower, (b) with randomized mass density of the structural members of it. Each time the parameters collected in Table 1 were treated as the expected values (or their deterministic counterparts), while the coefficient of variation was assumed as the parameter in the perturbation-based expansion and belonged to the interval [0.10, 0.20].

The results of computational analysis are presented in Tables 2a, 2b and 3a, 3b as well as in Figures 9–14.

Table 2b. Probabilistic moments of the eigenvalues for the telecommunication tower for the randomized Young modulus

Eigenvalue number	Expected values (2)	Expected values (4)	Expected values (6)	Expected values (8)	Expected values (10)
1	22.063E5	22.063E5	22.063E5	22.063E5	22.063E5
2	34.377E5	34.377E5	34.376E5	34.377E5	34.377E5
3	70.148E5	70.148E5	70.149E5	70.147E5	70.148E5
4	75.312E5	75.314E5	75.312E5	75.313E5	75.313E5
5	95.066E5	95.069E5	95.065E5	95.067E5	95.067E5
6	114.884E5	114.886E5	114.887E5	114.884E5	114.885E5
7	136.843E5	136.842E5	136.846E5	136.840E5	136.843E5
8	152.818E5	152.823E5	152.817E5	152.820E5	152.819E5
9	157.610E5	157.605E5	157.650E5	157.566E5	157.612E5
10	226.452E5	227.444E5	225.402E5	227.380E5	226.600E5

As we may observe in the attached tables, the expected values of the eigenvalues for the random Young modulus and mass density converge very fast. Of course, this convergence depends on the eigenvalue number being analyzed – the higher eigenvalue the larger differences between its expectations obtained from the neighboring orders of the perturbation. The quality of this method should be further compared against the results of the Monte-Carlo simulation for the same input quantities of random parameters. The comparison of Tables 2 and 3 leads to the second important conclusion that the expected values of all eigenvalues for the randomized Young modulus are somewhat smaller than those obtained for the randomized mass density. This result holds true for the fourth order probabilistic moments of all eigenvalues also. Let us note by the way that all of the probabilistic moments increase together with the eigenvalue number analyzed as it is observed in deterministic analysis. According to the method character, those results are supported by the additional response functions we have collected in Figures 9–11 (1st, 2nd and 4th eigenvalues) for the randomized Young modulus as well as in Figures 13 and 14 (1st and 2nd eigenvalues) for the randomized mass density. Figure 12 shows the expected value of the tenth eigenvalue for the random Young modulus, where the coefficient of variation is taken as the parameter belonging to the interval [0.1, 0.2], out of the second order theory validity.

Table 3a. Probabilistic moments of the eigenvalues for the telecommunication tower for the randomized mass density

Eigenvalue numbers	Expected values (2)	3rd order moments	4th order moments
1	22.134E5	0.615E13	0.304E17
2	34.483E5	0.212E14	0.222E18
3	70.364E5	0.173E15	0.329E19
4	75.532E5	0.188E15	0.511E19
5	95.369E5	0.471E15	0.124E20
6	115.230E5	0.721E15	0.268E20
7	137.257E5	0.124E16	0.498E20
8	153.013E5	0.160E15	0.778E19
9	158.080E5	0.180E16	0.918E20
10	227.243E5	0.510E16	0.422E21

Table 3b. Probabilistic moments of the eigenvalues for the telecommunication tower for the randomized mass density

Eigenvaluenumbers	Expected values (2)	Expected values (4)	Expected values (6)	Expected values (8)	Expected values (10)
1	22.134E5	21.999E5	22.197E5	22.026E5	22.092E5
2	34.483E5	34.297E5	34.555E5	34.344E5	34.420E5
3	70.364E5	69.952E5	70.546E5	70.051E5	70.231E5
4	75.532E5	75.139E5	75.690E5	75.237E5	75.401E5
5	95.369E5	94.814E5	95.600E5	94.950E5	95.186E5
6	115.230E5	114.618E5	115.494E5	114.736E5	115.035E5
7	137.257E5	136.506E5	137.566E5	136.693E5	137.009E5
8	153.013E5	152.861E5	152.954E5	152.920E5	152.926E5
9	158.080E5	157.224E5	158.443E5	157.433E5	157.800E5
10	227.243E5	226.054E5	227.736E5	226.349E5	226.852E5

As it can be recognized from Figures 9 and 10, the polynomium obtained for the first and second eigenvalues is very smooth (almost linear), so that is guarantees a reliable determination of its derivatives (no saddle points and fast oscillations).

Figure 11 shows the same tendency for the fourth eigenvalue polynomial response function around the mean value of the randomized parameter. One of the final results of the stochastic perturbation technique is given in Figure 12, where the expected values computed as the function of an input coefficient of variation converge very well together with the perturbation order. It is seen that the difference between the second order approach results (given by the red curve) and the remaining results cannot be neglected. The green curve reflects the fourth order theory, the yellow one – the sixth order approach, the blue and the black curves are plotted for the eight and tenth order theories. Obviously, the differences between the neighboring orders increase together with an increase of the coefficient of variation input value, however any differences between the last two orders cannot be noticed from this figure. Of course, the larger

coefficient of variation, the higher expected value of the tenth eigenvalue being analyzed. It means that the technique presented here is free from a limitation on the input random dispersion and may be reliably applied for any random variables and converges at the same time. At last we compare the response functions for the first and second eigenvalues, where the mass density of the structural elements is randomized.
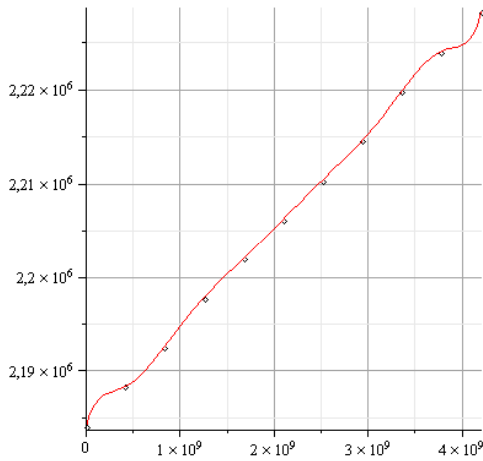
Fig. 9. The approximating polynomium
for the first eigenvalues
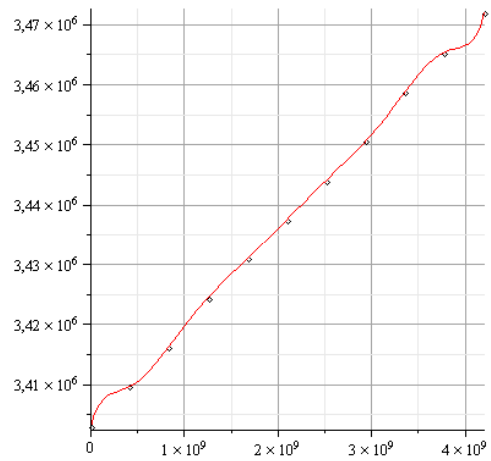
Fig. 10. The approximating polynomium
for the second eigenvalues
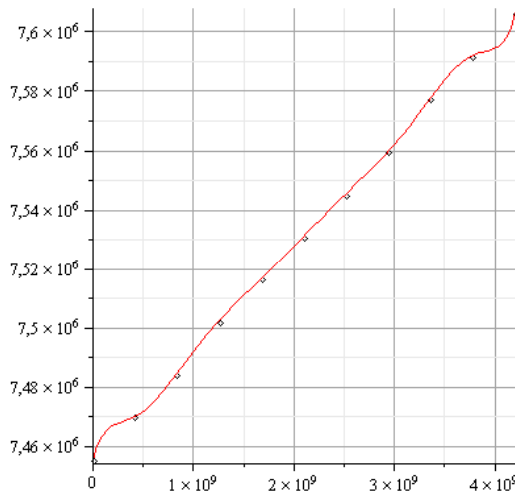
Fig. 11. The approximating polynomium for the fourth eigenvalues
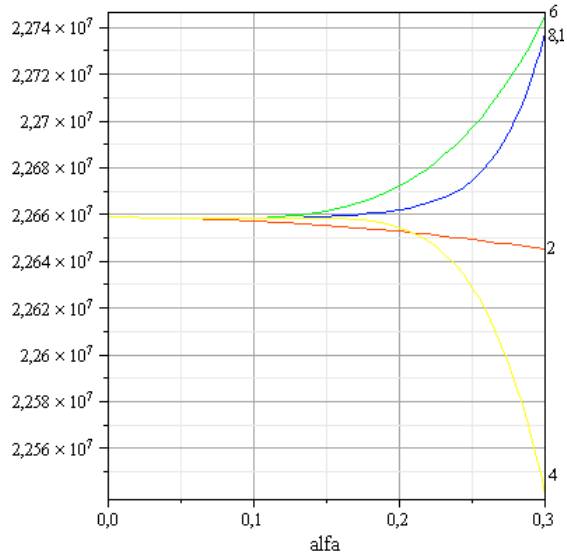
Fig. 12. The expected values for the tenth eigenvalue; random Young modulus

The obtained functions in Figures 13 and 14 are not so smooth like those obtained before, so that the corresponding probabilistic moments may be accompanied by the relatively larger errors.
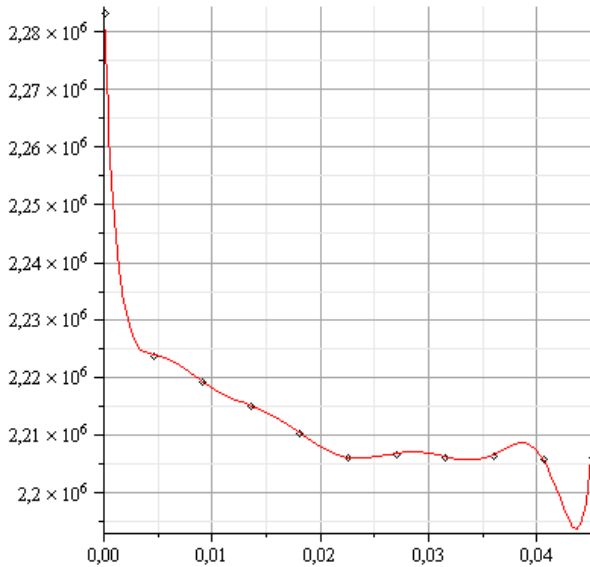
Fig. 13. The response function for the first eigenvalues; random mass density
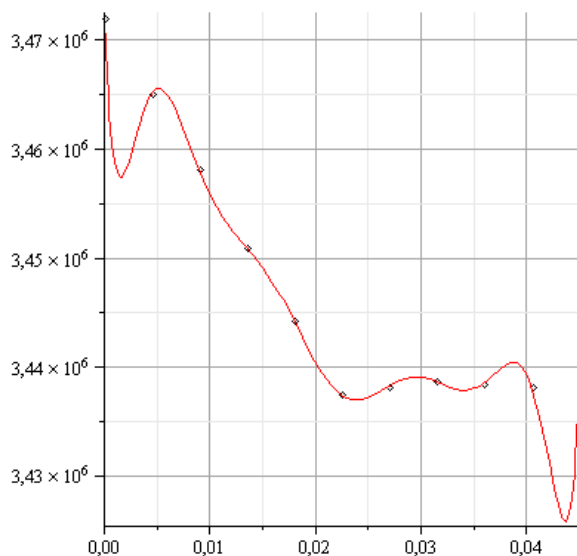
Fig. 14. The response function for the second eigenvalues; random mass density

6. Concluding remarks

1. As it was demonstrated here, the elastodynamic problems with random parameters may be solved efficiently using the generalized Stochastic Finite Element Method. A replacement of the straightforward technique with the response function method enables the relatively easy computations of any probabilistic moments for various eigenfrequencies of the engineering structures. The computational implementation of the traditional Finite Element Method code in conjunction with the symbolic algebra system MAPLE makes it possible to visualize the response functions for various eigenvalues as well as their probabilistic moments as the functions of the initial random input coefficients of variation.

2. This methodology may be further employed for more complex computational problems in stochastic mechanics after a successful comparison against the Monte-Carlo simulations. In particular, an application in the field of reliability engineering analysis seems to be the very promising. The main value of this technique, contrary to the straightforward approach implementation [3–5], is the opportunity to provide its computational realization also for the commercial FEM packages with no access to their source codes.

References

[1] Benaroya H.: *Random eigenvalues, algebraic methods and structural dynamic models*, Applied Mathematics and Computation, Vol. 52, No. 1, 1992, pp. 37–66.

[2] Hughes T.J.R.: *The Finite Element Method – Linear Static and Dynamic Finite Element Analysis*, Dover Publications, Inc., New York, 2000.

[3] Kamiński M.: *Generalized perturbation-based stochastic finite element method in elastostatics*, Computers and Structures, Vol. 85, No. 10, 2007, pp. 586–594.

[4] M. Kamiński: *On probabilistic viscous incompressible flow of some composite fluid*, Computational Mechanics, Vol. 28, No. 6, 2002, pp. 505–517.

[5] Kleiber M., Hien T.D.: *The Stochastic Finite Element Method*, Wiley, Chichester, 1992.

[6] Mehlhose S., vom Scheidt J., Wunderlich R.: *Random eigenvalue problems for bending vibrations of beams*, Zeitschrift für Angewandte Mathematik und Mechanik, Vol. 79, No. 10, 1999, pp. 693–702.

[7] Nair P.B., Keane A.J.: *An approximate solution scheme for the algebraic random eigenvalue problem*, Journal of Sound and Vibration, Vol. 260, No. 1, 2003, pp. 45–65.

[8] Pradlwater H.J., Schueller G.I., Szekely G.S., *Random eigenvalue problems for large systems*, Computers and Structures, Vol. 80, No. 27, 2002, pp. 2415–2424.

[9] Soize C.: *Random matrix theory and non-parametric model of random uncertainties in vibration analysis*, Journal of Sound and Vibration, Vol. 263, No. 4, 2003, pp. 893–916.

Losowe drgania własne konstrukcji wyznaczone metodą funkcji odpowiedzi i uogólnioną metodą perturbacji stochastycznej

Artykuł ukazuje metody analizy konstrukcji pozwalające efektywnie modelować drgania własne konstrukcji przestrzennych z losowym parametrem fizycznym bądź geometrycznym. Całkowita metodologia komputerowa jest oparta na tradycyjnej Metodzie Elementów Skończonych, wzbogaconej metodą perturbacji stochastycznej i jej podejściem *n*-tego rzędu. Komputerowa implementacja została wykonana w programie Metody Elementów Skończonych w powiązaniu z systemem komputerowym algebry symbolicznej MAPLE. W przeciwieństwie do poprzednich rozwiązań bezpośrednich, metoda funkcji odpowiedzi jest zastosowana do obliczeń probabilistycznych momentów dowolnego rzędu i współczynników wartości własnych konstrukcji. Funkcja odpowiedzi jest przyjęta w formie wielomianowej, a współczynniki zostały wyznaczone na podstawie kilku rozwiązań zagadnienia deterministycznego w otoczeniu wartości średniej odpowiedniego parametru losowego. Metoda ta jest zilustrowana na przykładzie stochastycznych drgań własnych prostego układu z jednym stopniem swobody i małej wieży stalowej modelowanej, jako kratowa konstrukcja 3D z losową gęstością masy, a także losowym modułem Younga. Metoda może zostać szeroko zastosowana w analizach niezawodności istniejących konstrukcji inżynierskich przy użyciu komercyjnych programów MES, jak również innych dyskretnych metod obliczeniowych, np. Metody Różnic Skończonych, czy Metody Elementów Brzegowych.

Application of statistical formulas
to hydrodynamic torque converter modelling

A. KESY

Technical University of Radom, Malczewskiego 29, 26-600 Radom, Poland

A. KADZIELA

Technical University of Łódź, Żeromskiego 116, 90-924 Łódź, Poland

In this paper a numerical estimation of hydrodynamic torque converter model is discussed. During the estimation it was assumed that the flow through in working area contains multiple flow streams. A contribution of each individual flow stream in transferring torque was assumed based on a pre-selected torque function. Model estimation relied upon proper equation and function parameter selection that provided minimization of the modelling error. Statistical factors were selected for accuracy evaluation of the modelled torque function. In this case torque functions were converted to diverging series, where values of fundamental statistical factors were calculated. Based on tests and numerical calculations for a pre-selected hydrodynamic torque converter it was concluded that there is a relation between modelling accuracy and values of some of the statistical factors. Application of statistical factors drastically simplified numerical calculations during modelling estimation.

Keywords: *hydrodynamic torque converter model, model estimation, statistical factors*

1. Introduction

Hydrodynamic torque converters (HTC) are widely applied in vehicle power transmission system. Their main advantages are attenuation of sheer vibrations and self adjustment to the applied load. Typical HTC contains three impellers of pump, turbine and stator completely sealed in one frame and filled with working fluid. Power transfer from turbine to pump is obtained via working fluid stream flow within impellers blade passages creating working area of HTC.

Non-dimensional steady-state characteristic is a fundamental function determining HTC. Graphic representation of this function is always provided within a technical specification of each HTC. Typically, non-dimensional steady-state characteristic of HTC provides three curves determining torque ration i_d, torque coefficient λ_M, efficiency η as a function of speed ratio $i_k = \omega_2/\omega_1$, where ω_1, ω_2 are angular velocities of inlet and exit shaft of HTC. Non-dimensional steady-state characteristics are prepared for a selected angular velocity ω_1 and k_o (typically 10) values of i_k ranging from $0 \le i_k < 1$. In order to provide non-dimensional steady-state characteristic it is necessary to

determine torques M_1, M_2 on inlet and exit shaft of HTC for each value of i_k and out-side diameter of HTC – D.

In order to properly select HTC for a vehicle power transmission system and to op-timize HTC construction, development of a mathematical model of HTC is required. It is necessary to properly select HTC to vehicle power transmission system and to op-timize its construction. Due to a complicated working fluid flow through multidimen-sional twisted working area, models based on average stream theory are still used for HTC working fluid flow calculations. Higher modelling accuracy can be obtained through the consideration of additional parameters, such as temperature of working fluid [1], quantitative division of fluid flow into multiple streams [2, 3] or through diligent estimation of modelling parameters [2]. During estimation calculations of HTC random methods are applied including Linja, Monte Carlo or Genetic Algorithm [2–4]. Proper estimation still requires empirical measurements of the modelled HTC. In order to simplify the estimation process of HTC mathematical modelling of statisti-cal factors was proposed in this paper.

2. Mathematical model of hydrodynamic torque converter

Mathematical model of HTC used here is numerical and called a model of multiple streams. This model was introduced based on the following assumptions:

• entire flow through within working area of HTC contains n_o independent streams,

• torque carried through HTC is a sum of torques carried by each stream. The contri-bution of each stream is not constant but varies and depends on a selected torque function.

The model calculates non-dimensional steady-state characteristic of HTC for pre-selected values of speed ratio i_k therefore becomes a discrete model.

A modelling solution is a sum of results for each individual stream contained within the entire fluid flow through inside a working area of HTC. Each individual stream is described as a single-dimensional model of an average stream [5]. Each stream on inlet and exit from the impeller of HTC has different radii and angles due to varying angles along blade edge. A number of streams are limited only by calculating capabilities of the applied computer and calculation time.

Flow through in working area of HTC is not uniform due to non-uniform wall re-action of working fluid flow passages. Most of the loads are concentrated:

• on active blade side (direct pressure on fluid stream),

• beginning of the blade length (influent fluid stream to the impeller runs directly into blade edges then twists and flows along the blade,

• external tours (due to centrifugal force acting on fluid stream).

Non-uniformity results in non-uniform fluid velocities within working area of the HTC, therefore non-uniform utilization of the working fluid to transfer torque [6]. Due to this non-uniformity a different contribution to torque transfer by each HTC working fluid stream was assumed.

Contribution of each HTC working fluid stream was described by a function called torque function. The torque function contains independent variable x which is defined as a division of consecutive number n of working fluid stream by the overall number of streams n_o within the working fluid flow through. A dependent variable of this function is a contribution factor in the torque transfer ranging 0–1. Based on analysis of actual velocities within HTC working space published by Flack [6] it was assumed that the torque function should be sloping up, real, differential, and continuous in the range of $0 \leq x \leq 1$. The torque function determines values of a, b, c, d, f taken from an assumed variables range.

A main disadvantage of the average stream model is typically lower torque calculated values than tests reveal [7, 8], therefore in order to obtain a value of stream contribution higher than 1, the contribution factor was multiplied by an increasing factor z constant for all flow through streams. Values of the constant z were selected from $1 \leq z \leq 3$ range. This range was obtained from initial calculations. A sample application of torque function model is shown on Figure 1.
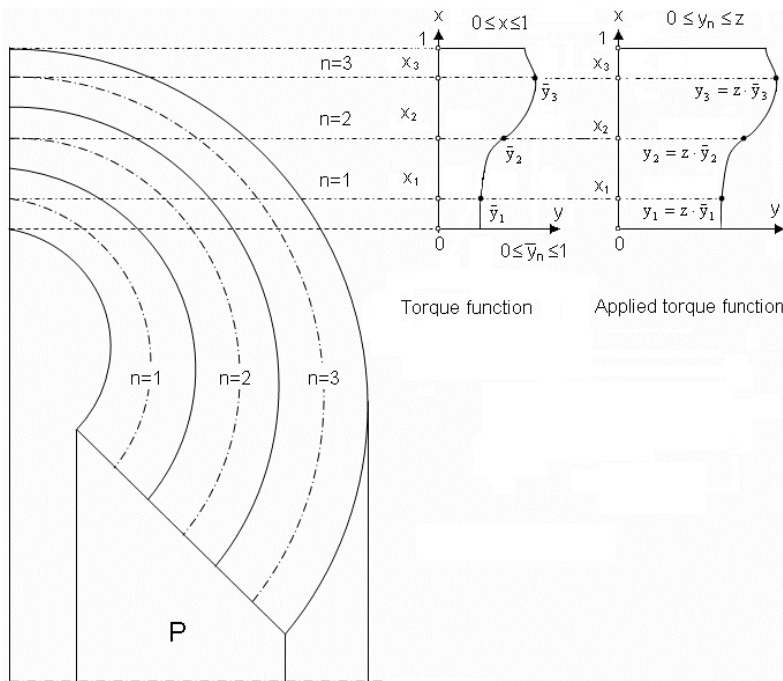
Fig. 1. Application of torque function in a mathematical model
of sample HTC for pump and for $n_o = 3$ streams

Mathematical model of HTC used to obtain non-dimensional steady-state characteristic can be described by the following equations:

$$i_d(i_k) = \frac{M_2}{M_1}; \qquad \lambda(i_k) = \frac{M_1}{\rho D^5 \omega_1^2}; \qquad \eta(i_k) = i_d i_k, \tag{1}$$

where:

$$M_1(i_k) = z \sum_{n=1}^{n_o} y_n M_{1,n}; \qquad M_2(i_k) = z \sum_{n=1}^{n_o} y_n M_{2,n};$$

$$M_{1,n} = \rho k_{12/32,n} Q^2 + \rho r_{12,n}^2 \omega_1 Q,$$

$$M_{2,n} = \rho k_{12/22,n} Q^2 + \rho r_{12,n}^2 \omega_1 Q + \rho r_{22,n}^2 \omega_2 Q, \tag{2}$$

$$a_{1,n} \omega_1^2 + a_{2,n} \omega_2^2 + a_{3,n} Q^2 + a_{4,n} \omega_1 Q + a_{5,n} \omega_2 Q = 0.$$

and:

$$k_{a/b} = \frac{r_a}{F_m} \operatorname{ctg} \beta_a - \frac{r_b}{F_m} \operatorname{ctg} \beta_b,$$

$$a_{1,n} = \frac{1}{2}\left(2r_{12,n}^2 - r_{11,n}^2 - \frac{r_{12,n}^4}{r_{21,n}^2} \right),$$

$$a_{2,n} = \frac{1}{2}\left(2r_{22,n}^2 - r_{21,n}^2 - \frac{r_{22,n}^4}{r_{31,n}^2} \right),$$

$$\begin{aligned} a_{3,n} = \quad & -\frac{1}{2}\left(\frac{1}{r_{11,n}^2} k_{32/11,n}^2 + \frac{1}{r_{21,n}^2} k_{12/21,n}^2 + \frac{1}{r_{31,n}^2} k_{22/31,n}^2 \right) + \\ & -\frac{\psi}{2F_{m,n}}\left(\operatorname{ctg}^2 \beta_{12,n} + \operatorname{ctg}^2 \beta_{22,n} + \operatorname{ctg}^2 \beta_{32,n} + 3 \right), \end{aligned} \tag{3}$$

$$a_{4,n} = k_{12/32,n} + k_{32/11,n} - \frac{r_{12}^2}{r_{21}^2} k_{12/21,n},$$

$$a_{5,n} = \quad -k_{12/22,n} - k_{12/21,n} + \frac{r_{22,n}^2}{r_{31,n}^2} k_{22/31,n},$$

$$F_{m,n} = \frac{\pi(r_{gz}^2 - r_{gw}^2)}{n_o},$$

$$\beta_{ij,n} = \frac{(\beta_{ijz} - \beta_{ijw})(\bar{r}_{ij,n} - r_w)}{r_z - r_w},$$

where:
    i – number of impeller ($i = 1$ – pump, $i = 2$ – turbine, $i = 3$ – stator);
    j – inlet or exist of impeller ($j = 1$ inlet, $j = 2$ exit);
    for inlet $r_w = r_{gw}$, $r_z = r_{gz}$, but for exit $r_w = r_{dw}$, $r_z = r_{dz}$.

$$r_{12,n} = \sqrt{\frac{n}{n_o}r_{gz}^2 + \left(1 - \frac{n}{n_o}\right)r_{gw}^2} \; ; \qquad r_{11,n} = \sqrt{\frac{n}{n_o}r_{dz}^2 + \left(1 - \frac{n}{n_o}\right)r_{dw}^2} \; , \qquad (4)$$

where: n changes values from 0 to n_o and

$$\bar{r}_{1j,n} = \sqrt{\frac{r_{1j,n}^2 + r_{1j,n-1}^2}{2}} \; , \qquad (5)$$

where n decreases from 1 to n_o and determines stream number.
    Remaining radii of average line of streams for the rest of the impellers were obtained as follows:
    • for turbine – inlet radius of turbine is equal to exit radius of pump, exit radius of turbine is equal to inlet radius of pump;
    • for stator – inlet radius of stator is equal to exit radius of pump.
    Method of radii tagging for impellers is shown on Figure 2, and sample tags of stream radii for pump and $n_o = 3$ streams is shown on Figure 3.
    The model input data is as follows:
    • HTC working point parameters – i_k and ω_1;
    • mode parameters – number of values of speed ratio k_o, number of streams n_o, value of flow losses coefficient ψ, torque increasing factor z;
    • HTC geometry and its working area dimensions – D, $r_{gz} = D/2$, r_{gw}, r_{dz}, r_{dw}, $\beta_{ij,z}$, $\beta_{ij,w}$;
    • torque function and its parameters – a, b, c, d, f.
    A computer program used to calculate the mathematical model of HTC contains primarily two nested calculation loops: exterior loop "for $i_k = 0$ to k_o" and interior loop "for $n = 1$ to n_o".

3. Estimation of the hydrodynamic torque converter model

    In order to provide construction calculations it is necessary to provide a precise mathematical model of HTC. Therefore an estimation of the model has to be performed. In other words it is necessary to provide model parameter selection that leads to minimal modelling error. In such model the following are estimated: torque function parameters a, b, c, d, f and parameters z, ψ. Number of streams n_o is obtained as a maximum value at a predetermined calculation time.

Fig. 2. Impeler radii tagging method

Fig. 3. Stream radii tagging method, for a pump and $n_o = 3$ streams

As a modelling precision criteria [2] average relative error of a non-dimensional steady-state characteristic HTC model was taken as described by the equation:

$$\bar{\delta} = \frac{1}{k_o} \sum_{k=1}^{k=k_o} u\delta_{i_d} + (1-u)\delta_\lambda, \tag{6}$$

where:
  u – weigh determining contribution of each characteristic error,

δ_{i_d} – relative error of torque ratio,

δ_λ – relative error of torque level coefficient.

Relative modelling errors of HTC characteristics are described by equations:

$$\delta_{i_d} = \frac{(i_{d,b} - i_{d,m})}{i_{d,b}} \cdot 100\%; \qquad \delta_\lambda = \frac{(\lambda_b - \lambda_m)}{\lambda_b} \cdot 100\%, \tag{7}$$

where index:

b – value obtained empirically,

m – value obtained from mathematical model calculations.

The modelling quality criteria, in other words the relative error, should obtain its minimal value.

4. Calculations of statistical factors

In order to calculate statistical factors based on torque function, it is necessary to convert the function into a divergent series y_n after values of the torque function constants were determined. It was done by dividing a range of independent variable $0 \le x \le 1$ for each torque function onto n_o sub ranges and determining middle elements values y_n, Figure [9, 10]. Next for each divergent series statistical factors were obtained.

In order to evaluate divergent series and their torque functions the following statistical factors were used:

• average value:

$$\bar{y} = \sum \frac{\bar{y}_n \varpi_n}{\Sigma \varpi_n}, \tag{8}$$

where ϖ is average relative frequency;

• standard deviation:

$$S(y) = \sqrt{\frac{\Sigma(\dot{y}_n - \bar{y})^2 m_n}{\Sigma m_n}} = \sqrt{\frac{\Sigma(\dot{y}_n^2 m_n)}{\Sigma m_n} - \left(\frac{\Sigma(\dot{y}_n m_n)}{\Sigma m_n}\right)^2}, \tag{9}$$

where m is series size and $\dot{y}$ is value of average weigh;

• classic variation factor in [%]:

$$V(y) = \frac{S(y)}{\bar{y}} \cdot 100\%, \tag{10}$$

- average deviation:

$$D(y) = \frac{\Sigma|\dot{y} - \overline{y}|m_n}{\Sigma m_n}, \tag{11}$$

- classic factor for measurement of asymmetric value:

$$A(y) = \frac{e_3}{S^3(y)}, \tag{12}$$

where: $e_3 = \dfrac{\Sigma(\dot{y}_n - \overline{y})^3 m_n}{\Sigma m_n}$,

- concentration factor:

$$K(M) = 1 - \Sigma[t(y < y_{1n}) + t(y < y_{1n-1})]w_n, \tag{13}$$

where:
  w – relative frequency,
  t – value of considered size.
Factors $S(y)$, $V(y)$, $D(y)$ determine how far and how dense the obtained values are from average value $\overline{y}$. Asymmetric measure $A(y)$ is used for slope analysis variables y, but concentration measure $K(M)$ is related to asymmetric measure and determines density of variables y.

In order to obtain statistical factors, numerical calculations do not require sophisticated programming techniques therefore calculation time is relatively short.
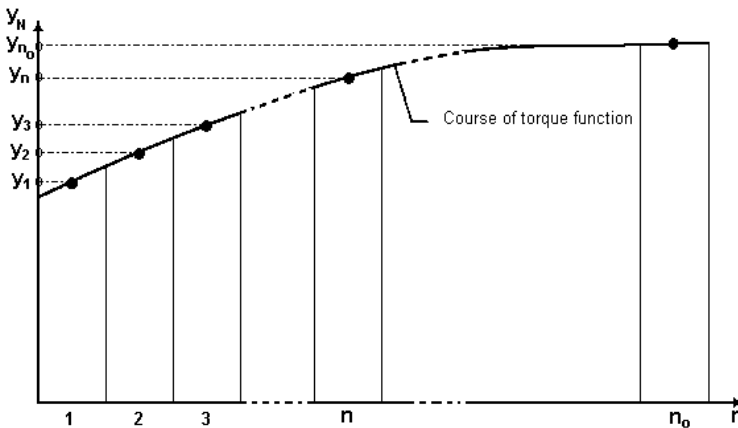
Fig. 4. Statistical factors determination scheme

5. Evaluation of function with statistical factors application

In order to prove that there is a relation between statistical factors and the accuracy of mathematical model, testing and measurements required for modelling estimation were performed for HTC type PH1.410.14 with active diameter $D = 410$ mm.

5.1. Testing

The testing was performed on a test rig. The test rig allowed continuous modulation of torque load applied to HTC while varying angular velocities of inlet and exit shafts. The empirical testing was performed with a constant angular velocity of inlet shaft equal to $\omega_1 = 210$ rad/s. Measuring data were speed ratio i_k in a range of 0 to 1. Assumed $k_o = 24$ measurement points, from $i_k = 0$ to $i_k = 0.5$ every 0.1, and from $i_k = 0.5$ to $i_k = 0.6$ every 0.05 and from $i_k = 0.6$ to $i_k = 1$ exchangeable every 0.03 and 0.02. Values of speed ratio i_k for each measurement point were obtained through the application of a braking system to vary angular velocity of exit shaft. For each $k_o = 24$ measurement point exit angular velocity and torque on inlet and exit shaft were measured. The measurement results of torque, angular velocities of inlet and exit shafts for HTC and values obtained from calculations are shown in Table 1.

Table 1. Measurement results of the tested HTC type PH1.410.14 for $\omega_1 = 210$ rad/s

No.	ω_2	M_1	M_2	i_k	i_d	η	$\lambda \cdot 10^{-3}$
	[rad/s]	[Nm]	[Nm]	[–]	[–]	[–]	[1/rad^2]
1	0	1645	3865	0	2.35	0	3.92
2	21	1653	3680	0.10	2.23	0.223	3.93
3	44	1643	3432	0.20	2.09	0.418	3.91
4	63	1634	3185	0.30	1.95	0.585	3.90
5	85	1632	2934	0.40	1.80	0.721	3.88
6	105	1603	2581	0.50	1.61	0.805	3.82
7	126	1510	2149	0.60	1.42	0.852	3.59
8	147	1384	1738	0.70	1.26	0.882	3.29
9	168	1201	1324	0.80	1.10	0.881	2.85
10	189	919	843	0.90	0.92	0.828	2.19
11	200	729	601	0.95	0.82	0.779	1.74
12	206	594	455	0.98	0.76	0.745	1.41

5.2. Numerical calculations

Calculations were performed using a computer program written in the Turbo Pascal programming language applying numerical random method Monte Carlo [2, 11]. Multiple stream type models contain values that have to be determined before the application of the model. For the analyzed HTC such values of parameters are as follows: z, ψ, k_o, n_o and also the torque function and values of parameters a, b, c, d, f. Additionally a number of selections l_o for the Monte Carlo method and values of

weigh u have to be determined. Fifteen function curves, as the torque functions were selected in these calculations representing various types of functions used in technical modelling [3, 12]. Type of equations and a number of constant parameters of the function are provided in Table 2. Torque function from Table 2 was converted to values ranging $0 \leq y_n \leq 1$ by dividing actual function value by the maximum possible function value available for the referenced range. Declining functions were converted to inclining for the range $0 \leq x \leq 1$ through the application of $x: = 1 - x$ conversion in the computer program. Values and ranges of the remaining parameters of the model are shown in Table 3.

Table 2. Torque functions selected for initial calculations; e – Neper number

No.	Function tag	Function equation	No. of constant parameters
1	**2**	**3**	**4**
1	F1	$y = \left| ax^4 + bx^3 + cx^2 + dx \right|$	4
2	F2	$y = \left| ax(x-1)(x-b)(x-c) \right|$	3
3	F3	$y = \left| ax(x-1)(x-b)(x-c) + d \right|$	4
4	F4	$y = \left| a + (1-a)x \right|$	1
5	F5	$y = \left| 1 - ax \right|$	1
6	F6	$y = \left| e^{ax} \cdot bx(x-1)(x-c) \right|$	3
7	F7	$y = \left| e^{(x-1)} \cdot ax(x-1)(x-b) \right|$	2
8	F8	$y = \left| ax(x-1)(x-b)(x-c)e^{dx+f} \right|$	5
9	F9	$y = \left| \dfrac{a}{b + cx^3} \right|$	3
10	F10	$y = \left| \dfrac{a}{b + c(1-x)^3} \right|$	3
11	F11	$y = \left| \dfrac{a}{b + c(1-x^3)} \right|$	3
12	F12	$y = \left| \dfrac{1}{a - b\ln(cx)} \right|$	3
13	F13	$y = \left| e^{-ax^2} \cdot [b\cos(cx^2) + d\sin(cx^2)] \right|$	4
1	**2**	**3**	**4**
14	F14	$y = \left| e^{-a(1-x^2)} \cdot \{b\cos[c(1-x^2)] + d\sin[c(1-x^2)]\} \right|$	4
15	F15	$y = \left| \dfrac{a - b\cos x}{c - d\sin x} \cdot x \right|$	4

Table 3. Parameter values and ranges applied in numerical calculations of the HTC model

l_o	n_o	u	a, b, c, d, f	Ψ	Z
30 000	30	0.5	1–2	0.3–0.4	1–3

Calculations of each variable were repeated 10 times due to the randomness of the applied calculation method which resulted in obtaining different function curves each time. For each repetition randomly selected values of *a*, *b*, *c*, *d*, *f* were different. As a calculation result minimum and maximum values of the calculated data were taken.

Calculations were done in two steps. For each torque function the following were calculated:
- modelling error,
- statistical factors.

Table 4 shows calculation results of modelling error $\bar{\delta}$ for the analyzed torque function obtained from 10 repetitions of the computer program and parameter values for which these errors were obtained. Per Table 4 minimum modelling error $\bar{\delta}$ was obtained for torque functions F9, F10 and F11 as multidimensional inverted functions. Error magnitude deviates for about 0.02, while error difference between each function with small error $\bar{\delta}$ F12 and functions F10 and F11 was about 0.1, therefore is was five time higher. Small modelling error values $\bar{\delta}$ are noticeable and these functions are distinctive among others. The torque function curves for extreme value of constant parameters *a*, *b*, *c* determined by assumed ranges 1–2 are shown in Figure 5.

Table 4. Minimum values of modelling error $\bar{\delta}$ and corresponding modelling parameter values for the analyzed torque function per Table 2

No.	Function tag	$\bar{\delta}$ [%]	a	b	c	d	f	ψ	z
1	F1	10.98	–0.979	0.622	0.210	0.147	–	0.395	2.596
2	F2	9.52	1.012	1.957	1.988	–	–	0.399	2.977
3	F3	5.74	1.119	1.576	1.132	1.076	–	0.380	2.795
4	F4	5.03	1.289	–	–	–	–	0.395	2.877
5	F5	12.93	1.996	–	–	–	–	0.368	2.931
6	F6	5.18	1.587	1.008	1.621	–	–	0.384	1.909
7	F7	9.18	1.150	1.973	1.678	–	–	0.309	1.127
8	F8	5.87	1.049	1.063	1.000	1.292	1.345	0.329	2.327
9	**F9**	**4.57**	1.418	1.618	1.180	–	–	0.393	1.944
10	**F10**	**4.59**	1.726	1.795	1.003	–	–	0.395	2.092
11	**F11**	**4.59**	1.093	1.381	1.111	–	–	0.387	2.252
12	F12	4.69	1.561	1.160	1.060	–	–	0.385	1.893
13	F13	4.73	1.575	1.175	1.509	1.268	–	0.391	2.742
14	F14	6.09	1.063	1.022	1.107	1.982	–	0.355	2.759
15	F15	6.08	1.015	1.535	1.754	1.230	–	0.343	1.240

Table 5. Statistical factors ranges $V(y)$, $A(y)$, $K(M)$ calculated for torque function per Table 2

No.	Function tag	$V(y)$	$A(y)$	$K(M)$
1	F1	50.7–63.8	1.2138–1.2964	0.2871–0.3649
2	F2	50.9–69.5	1.1989–1.3773	0.2803–0.3972
3	F3	8.4–32.8	1.3133–5.4279	0.0405–0.1829
4	F4	6.0–64.1	1.2177–6.2231	0.3596–0.3659
5	F5	9.1–59.2	1.1162–5.7463	0.0399–0.2249
6	F6	42.9–69.5	1.1989–1.5773	0.3003–0.3972
7	F7	13.2–49.9	1.3171–3.2192	0.0588–0.2857
8	F8	46.9–204.1	1.1268–2.3426	0.2527–0.8203
9	F9	12.8–24.1	1.3713–2.1102	0.0655–0.4327
10	F10	12.6–26.1	1.3370–2.1422	0.0760–0.1444
11	F11	6.6–50.9	1.3007–13.8178	0.0132–0.2929
12	F12	30.8–66,5	1.3592–1.5696	0.1754–0.3638
13	F13	23.2–44.3	1.2982–1.6452	0.1166–0.2469
14	F14	12.6–46.6	1.2570–1.6049	0.0759–0.2640
15	F15	53.2–148.9	1.2905–2.3535	0.2801–0.6757

Tables 5 and 6 show results of minimum and maximum values of statistical factors for torque function according to Table 2 determining ranges of these factors obtained during calculations for ten computer program repetitions. Analysis of average value $\overline{y}$ (Table 6) reveals that function curves are moved upward toward value of $y = 1$. Only for torque functions F8 and F15 minimal values of factor $\overline{y}$ are smaller than 0.5. These functions provide significant values of classic coefficient $V(y)$, where they are distinctive among other functions.

Table 6. Statistical factors ranges $\overline{y}$, S_y, D_y calculated for torque factors per Table 2

No.	Function tag	$\overline{y}$	S_y	$D(y)$
1	F1	0.5371–0.6185	0.3137–0.3425	0.2750–0.3072
2	F2	0.5105–0.7054	0.3004–0.3545	0.2623–0.3196
3	F3	0.7144–0.9428	0.0638–0.2318	0.0603–0.2034
4	F4	0.5432–0.9495	0.0463–0.3481	0.0397–0.3118
5	F5	0.4881–0.8962	0.0818–0.3347	0.0546–0.2828
6	F6	0.5105–0.7054	0.2304–0.3545	0.2023–0.3196
7	F7	0.5808–0.9122	0.1207–0.3898	0.0832–0.2703
8	F8	0.1286–0.6490	0.2625–0.3870	0.1840–0.3769
9	F9	0.7975–0.8955	0.1146–0.1925	0.0943–0.1686
10	F10	0.7816–0.9798	0.1081–0.2041	0.0872–0.1798
11	F11	0.5330–0.9655	0.0639–0.2714	0.0202–0.2351
12	F12	0.3567–0.6623	0.2042–0.2402	0.1727–0.2000
13	F13	0.6762–0.8479	0.1966–0.2999	0.1631–0.2647
14	F14	0.6382–0.8459	0.0915–0.2980	0.0902–0.2641
15	F15	0.1419–0.6786	0.2114–0.3862	0.1515–0.3112

6. Comparison of modelling error values and statistical factors

Table 7 shows values of modelling error $\bar{\delta}$ together with values of statistical factors for torque functions per Table 2. Based on the table data it can be determined that there are torque functions with different values of modelling error $\bar{\delta}$ and closely simi-
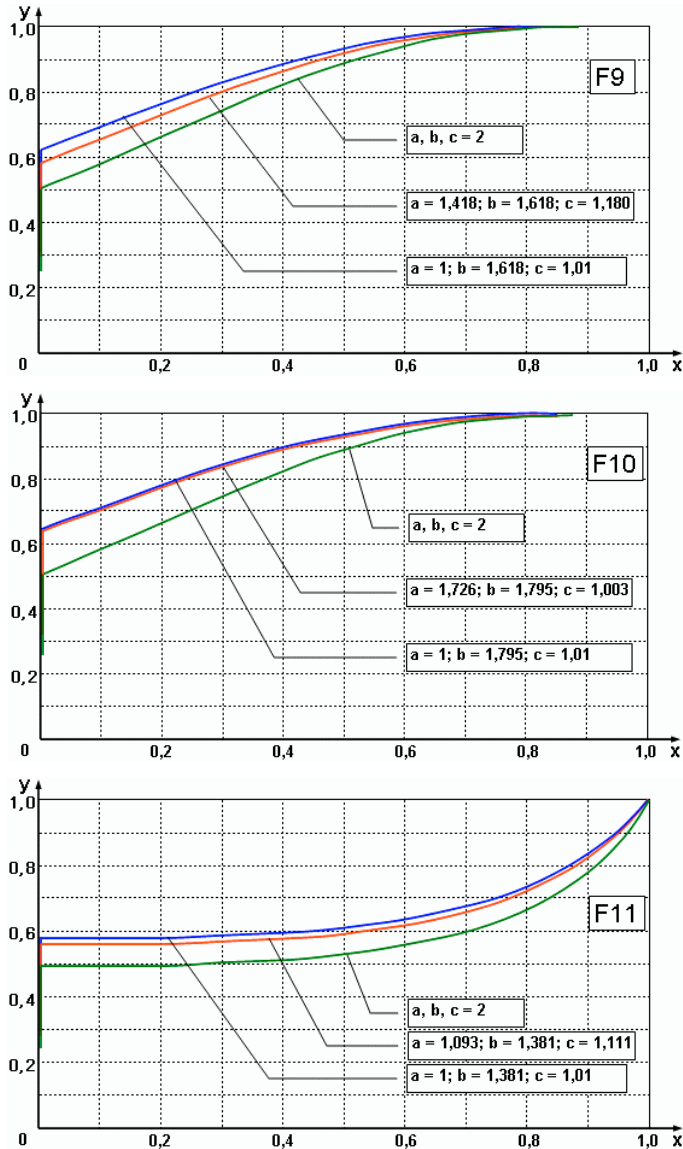
Fig. 5. Function curves where modelling error is minimal for parameter *a*, *b*, *c* values ranging 1–2

lar values of statistical factors. In the example, torque function F11 where $\bar{\delta}$ = 4.57% average value of $\bar{y}$ = 0.6428, and for F15 with average value $\bar{\delta}$ = 6.08%, therefore with error higher than 33% average value $\bar{y}$ is very similar and equal to $\bar{y}$ = 0.6497. However statistical factors for these torque functions differ considerably as follows: for function F11 $V(y)$ = 18, but for function F15 $V(y)$ = 55.1. On the other hand torque functions F9, F10 and F11 have similar values of all statistical factors. Therefore, there are functions which are more suitable for application as torque functions in the mathematical model of the analyzed HTC. These functions contain much closer values of statistical factors and these factors can be applied to evaluate the usefulness of each function as a torque function.

Table 7. Value comparison of statistical factors and modeling error $\bar{\delta}$ for torque function per Table 2

No.	Function tag	$\bar{\delta}$ [%]	$\bar{y}$	S_y	$D(y)$	$V(y)$	$A(y)$	$K(M)$
1	F1	10.98	0.5605	0.3330	0.2970	59.4	1.2313	0.3396
2	F2	9.52	0.6171	0.3162	0.2775	51.2	1.2931	0.2900
3	F3	5.74	0.9128	0.0863	0.0610	9.5	5.2316	0.0421
4	F4	5.03	0.8865	0.0855	0.0594	9.6	5.0152	0.0439
5	F5	12.93	0.4990	0.2901	0.2515	58.1	1.2977	0.3347
6	F6	5.18	0.6426	0.3070	0.2669	47.8	1.3334	0.2684
7	F7	9.18	0.6523	0.3042	0.2634	46.6	1.3503	0.2610
8	F8	5.87	0.5300	0.3550	0.3193	67.0	1.2056	0.3823
9	**F9**	**4.57**	**0.8682**	**0.1376**	**0.1163**	**15.8**	**1.7133**	**0.0837**
10	**F10**	**4.59**	**0.8930**	**0.1169**	**0.0965**	**13.1**	**2.0552**	**0.0673**
11	**F11**	**4.59**	**0.6428**	**0.1154**	**0.0891**	**18.0**	**2.0261**	**0.0867**
12	F12	4.69	0.6462	0.2089	0.1771	32.3	1.3819	0.1843
13	F13	4.73	0.7844	0.2432	0.2089	31.0	1.4432	0.1648
14	F14	6.09	0.8272	0.1290	0.1141	15.6	1.5663	0.0854
15	F15	6.08	0.6497	0.3577	0.2995	55.1	1.5105	0.3085

7. Conclusions

Numerical model of HTC assumes that flow through in working area contains multiple streams. Each stream takes part in torque transfer. Contribution of each stream in torque transfer was determined based on a pre-selected torque function. During the process of model estimation it is necessary to select a form and parameter values for torque function in such a manner that allows obtaining a minimal modelling error. In order to obtain acceptable accuracy, statistical factors are used and calculated for divergence series obtained from these functions.

Based on empirical testing and numerical calculations for the analyzed HTC type PH1.410.14 it was determined there is a relation between modelling accuracy and statistical factors values. Use of statistical factors significantly simplifies the estimation process of the described by a mathematical model HTC, because it allows neglecting the step of selecting a form of torque function equation. Therefore estimation relied only on the se-

lection of modelling parameters. Taking into account the computer programming time and calculation time with application of random methods based on repetitive calculation for randomly selected set of parameters the estimation effort becomes about 50% simpler. Statistical factors calculations do not require a sophisticated computer programming technique and calculation time is relatively short.

Wider application of this torque function selection method during estimation of HTC model requires further testing and numerical calculations for other types of HTC.

References

[1] Kesy Z.: *Hydrodynamic torque converter controlled by working fluid properties*, Technical University of Radom Publishing Company, Radom, 2003.
[2] Kesy A.: *Identification and optimization of hydrodynamic transmission system*, Technical University of Radom Publishing Company, Radom, 2004.
[3] Kadziela A.: *Modelling and optimization of hydrodynamic torque converter with using of genetic algorithm*, PhD thesis, Technical University of Radom, Radom, 2006.
[4] Stesin S.P.: *Optimization of parameters of hydrodynamic transmission systems of building and road machines*, Mashinostroenie, Moscow, 1996.
[5] Pawelski Z.: *Investigation of hydrodynamic torque converter characteristics for unsteady – state of Load*, PhD thesis, Technical University of Łódź, Łódź, 1980.
[6] Flack R.: *Experimental flow fields in an automotive torque converter an invited summary and review paper*, International Journal of Vehicle Design, Vol. 38, No. 2–3, 2005, pp. 240–258.
[7] Stesin S.P.: *Blade machines and hydrodynamic torque converters*, Mashinostroenie, Moscow, 1990.
[8] Kesy Z., Kesy A., Kadziela A.: *Estimation of parameters for a hydrodynamic transmission system mathematical model with the application of genetic algorithm*, Solids Mechanics and its Application, Kluwer Academic Press, 2004, pp. 143–152.
[9] Saltzer B.K.: *Math 300: Descriptive statistics*, Strayer University, 2005.
[10] Starzynska W.: *Practical statistics*, PWN, Warszawa, 2002.
[11] Casella G., Robert C.P.: *Monte Carlo statistical methods*, Springer-Verlag LLC Pub. New York, 2004.
[12] Morrison F.: *The Art of modelling dynamic systems. Forecasting for chos*, Randomness, an Determinism. Multiscience Press Inc., 1991.

Użycie wskaźników statystycznych w modelowaniu przekładni hydrokinetycznej

Artykuł dotyczy estymacji numerycznego modelu przekładni hydrokinetycznej, w którym założono, że przepływ w przestrzeni roboczej składa się z wielu strug. W tym modelu udział poszczególnych strug w przenoszeniu momentu obrotowego określono na podstawie arbitralnie dobranej funkcji rozkładu momentu. Estymacja modelu polegała na doborze postaci równania i parametrów tej funkcji, tak żeby uzyskać najmniejszy błąd modelowania. Do oceny funkcji rozkładu momentu pod kątem dokładności modelu zaproponowano użycie wskaźników statystycznych. W tym celu dobierane funkcje rozkładu momentu zamieniono na szeregi rozdzielcze, dla których następnie obliczano wartości podstawowych wskaźników statystycznych. Na

podstawie badań doświadczalnych i obliczeń numerycznych wybranej przekładni hydrokine-tycznej wykazano, że istnieje związek między dokładnością modelu, a wartościami pewnych wskaźników statystycznych. Użycie wskaźników statystycznych znacznie upraszcza obliczenia numeryczne podczas estymacji.

Numerical analysis of lateral forces
in a die for turbine blade forging

A. KOCAŃDA, P. CZYŻEWSKI

Warsaw University of Technology, ul. Narbutta 85, 02-524 Warsaw, Poland

KHEDHEYER H. MEHDI

Transport Equipment Enterprise PZL-Rzeszów S.A.

There are various processes for production of turbine blades. Hot forging has been the most common, especially for automotive, marine and industrial turbochargers or aero-engines turbines. Advanced computer modelling has become a powerful tool for process planning and tool design in order to get near-net shape blades in hot forging. This paper presents the effect of die cavity positioning on metal flow and distribution of lateral forces in the die during aero-engine turbine blade hot forging. An influence of torsional moment on dies offsetting introduced by these lateral forces has also been pointed out.

Keywords: *turbine blade, forging, lateral forces, torsional moment, computer modelling*

1. Introduction

Analysis of lateral forces in the dies for turbine blade forging has been the main aim of this paper. Small lot production is rather typical for turbine blades what could be regarded as not suitable for hot forging because of high cost of tools. However, forgings are characterized by very advantageous distribution of grains and relatively high strength what has usually been regarded as more important than relatively high cost per piece. There is a growing demand to produce turbine blades in near net-shape geometry. This demand requires special design of dies and special control of forging process. Numerical simulation of blade forging process is difficult due to three-dimensional twisted shape of the blade, non-steady state contact between the die surface and the workpiece, and thermo-mechanical loads. Hence numerous works have been done to develop 3D FEM simulation in order to get deformed configurations on the forging stages and to find the optimized die and preform shapes [1, 2, 7]. Also, minimization of the forging errors with the inclusion of press and die deflections has also been performed [3, 4].

One of the ways to minimize tolerances and allowances is limitation of lateral forces which are present in the dies during forging process. They would cause offsetting of upper and lower dies what results in unacceptable geometrical errors of the forgings. Lateral forces depend mainly on arrangement of die cavity in the die block and positioning of the parting surface [5, 6]. As for industrial practice, finding an optimized die design with low

lateral forces usually requires some number of tool sets to be tested. This way is very expensive. On the other hand, computer modelling provides a possibility to carry out virtual test with different sets of tools what considerably decreases cost of trials [8].

As for this paper, computer modelling of turbine blade forging has been carried out by means of SuperForge software based on finite volume method FVM. Analysis of numerical results has provided data on die loading including lateral forces as well as on an appropriate filling of die cavity in order to limit material folding and fracture. This opens the possibility to counteract the lateral thrust by a proper die design and machining counterlocks into the parting surfaces of the dies.

2. Turbine blade forging

Square bar made of alloyed structural steel PN 18H2N4WA (0.18% C, 1.4% Cr, 4.2% Ni, 1% W), equivalent to DIN 1.5919, has been used to prepare a preform for forging of turbine blade in industrial process. Preform was heated to 1150 °C. Slight upsetting of the preform was used to remove scale from the surface. Next, the preform was forged just in one die cavity. After trimming the flesh, the forging was subjected to drop sizing. Figure 1 presents photos of industrial dies and the final forging.
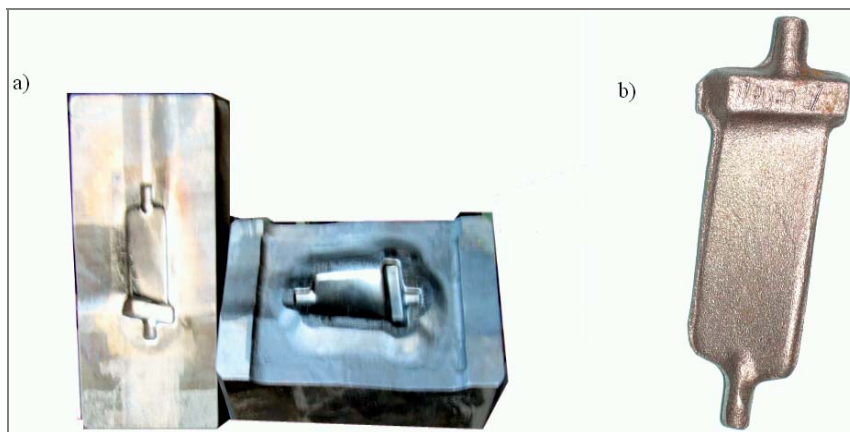
Fig. 1. Industrial dies (a) and the final forging – turbine blade (b)

3. Computer modelling

There were taken into account two cases in computer modelling of turbine blade forging. Case I was related directly with the industrial forging. As for case II, two forgings were made simultaneously at the same stroke of hammer. There were two cavities in one die block. The cavities were positioned in opposite directions as regarding the shape of turbine blade, see Figure 2. Computer models of the dies were prepared by using Unigraphics files on detailed die design.

Dies were preheated before forging to 300 ºC. Friction conditions between lubricated die surface and deformed material were described by friction factor $m = 0.2$. Forging parameters were defined according to crank forging press LKM1600. Thermomechanical numerical analysis took into account temperature dependent changes of material properties during forging. Tools were modelled as elastic bodies and heat transfer was taken into account. A shape of forging obtained by means of computer modelling is shown in Figure 3. This shape corresponded very well with the shape of industrial forging and was the same for cases I and II.
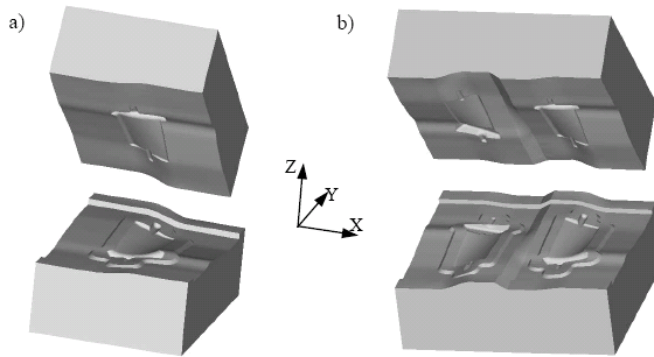
Fig. 2. Computer models of upper and lower dies for turbine blade forging;
case I – industrial dies (a), case II – dies with doubled cavities (b)
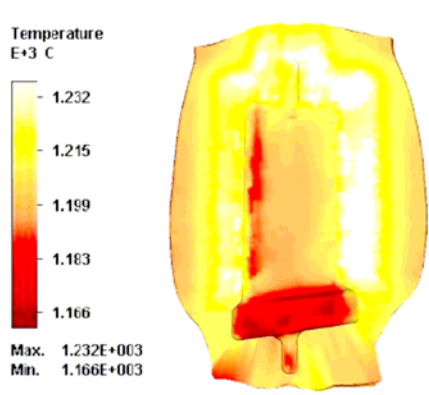
Fig. 3. Turbine blade with a flesh (computer modelling)

4. Numerical results

Figures 4 and 5 present changes in *X* and *Y* lateral forces acting on die cavity for case I and case II. The direction of *x* and *y* axis are shown in Figure 2. Forces had opposite directions for upper and lower dies, Figure 4. Generally lateral force *X* is much

bigger than lateral force *Y*. Maximum values of lateral forces *X* were equal to about 5% of forging force *Z*. These relatively high values would cause offsetting of the upper and lower dies.
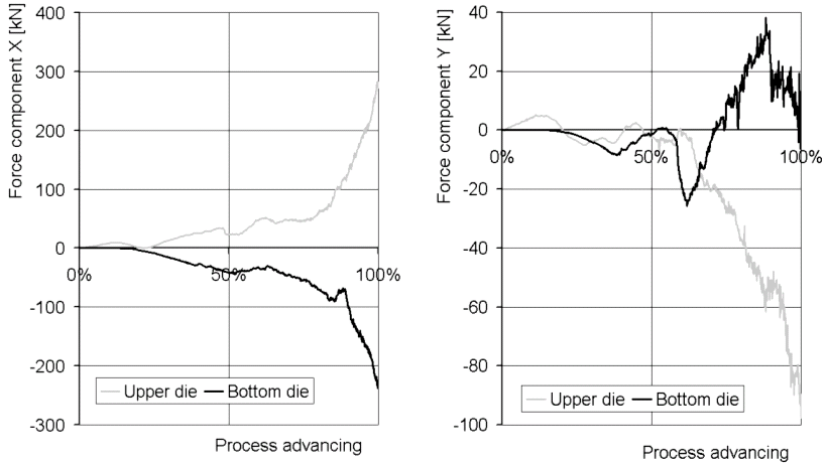
Fig. 4. Changes in *X* and *Y* lateral forces for case I (industrial die)
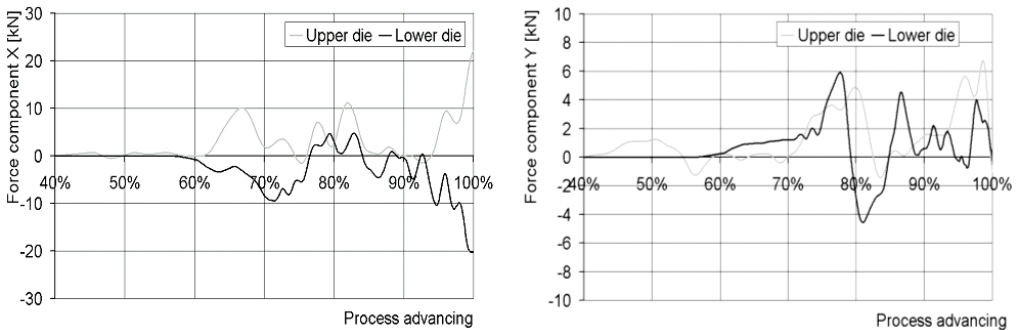
Fig. 5. Changes in *X* and *Y* lateral forces for case II (dies with doubled cavities)

   To minimize an influence of lateral forces on accuracy of forgings, a die design with doubled cavities was proposed. The arrangement of the cavities in opposite directions was supposed to counterbalance *X* lateral forces for each die cavity. It has really been observed – summary of the forces was a few times lower than the force in case I. Origins and values of lateral forces vectors are shown in Figure 6. Though the directions of *X* lateral forces are opposite for each cavity and the summary of the lateral forces is minimized, some torsional moment and tensile stresses in the upper die appeared. Torsional moment should be counterbalanced by special counterlocks.
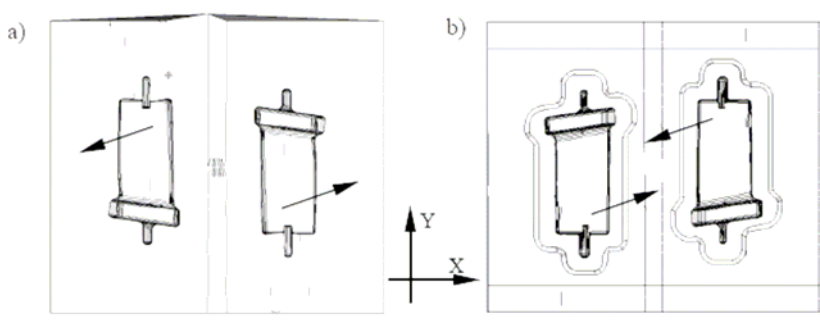
Fig. 6. Summary vectors of maximum lateral forces *X* and *Y* for upper (a) and lower (b) dies (case II)

Tensile stresses are dangerous for hard tool material and would increase a sensitivity to crack initiation in the die.

5. Conclusions

1. Numerical modelling of turbine blade forging revealed considerably high lateral forces in die cavities which would cause offsetting of the lower and upper dies leading to geometrical inaccuracies of the forgings.

2. Doubling die cavities for the same stroke resulted in a considerable decrease in values of *X* lateral forces. However, some new undesirable phenomena appeared – torsional moment between upper and lower dies and tensile stresses in the upper die.

3. An analysis of causes of upper and lower dies offsetting should take into account not only lateral forces but torsional moments as well. Then appropriate counterlocks could be carefully designed for the near net-shape forging dies.

References

[1] Mei Zhan, Yuli Liu, He Yang: *A 3D rigid-viscoplastic FEM simulation of compressor blade isothermal forging*, Journal of Materials Processing Technology, Vol. 117, 2001, pp. 56−61.

[2] Cheng Lv, Liwen Zhang, Zhengjun Mu, Qingan Tai, Quying Zheng: *3D FEM simulation of the multi-stage forging process of a gas turbine compressor blade*, Journal of Materials Processing Technology, Vol. 198, 2008, pp. 463−470.

[3] Zhang H.G., Dean T.A.: *Computer modelling of tool loads and press/tool deflections in multistage forging*, International Journal of Machine Tools Manufacturing, Vol. 35, No. 1, 1995, pp. 61–69.

[4] Ou H., Lan J., Armstrong C.G., Price M.A.: *An FE simulation and optimization approach for the forging of aero-engine components*, Journal of Materials Processing Technology, Vol. 151, 2004, pp. 208–216.

[5] Kocańda A., Czyżewski P., Krzyszkowski P.: *Some developments in analysis of lateral forces and cyclic loading with relation to forging dies*. Proceedings of the 8th ICTP Advanced Technology of Plasticity, Verona, 2005, pp. 171.

[6] Kocańda A., Czyżewski P.: *Determination of side forces in a forging dies*. Proc. 6th Int. Conf. on Industrial Tools and Materials Processing Technologies, Bled, 2007, pp. 57–62.

[7] Czyżewski P., Kocańda A.: *Computer modeling of valve lever forging with various performs*, Archives of Civil and Mechanical Engineering, Vol. VIII, No. 3, 2008, pp. 33–40.

[8] Gronostajski Z., Hawryluk M.: *The main aspects of precision forging*, Archives of Civil and Mechanical Engineering, Vol. VIII, No. 2, 2008, pp. 39–57.

Analiza numeryczna sił bocznych w matrycy do kucia łopatki turbiny

Wiele jest sposobów produkcji łopatek turbin, a kucie na gorąco zaliczane jest do klasycznych. Poprzez kucie produkuje się łopatki do sprężarek różnych silników samochodowych, okrętowych, przemysłowych itd. Zaawansowane modelowanie komputerowe stało się poważnym narzędziem w opracowaniu procesów technologicznych i konstrukcji narzędzi do kucia łopatek prawie na gotowo. W referacie przedstawiono wpływ umiejscowienia wykrojów w matrycy na płynięcie metalu i zmiany sił bocznych działających na wykrój matrycy w trakcie procesu kucia łopatki. Wskazano również, że powstaje moment skręcający matryce dolne i górne, prowadzący do błędów wynikających z przesadzenia matryc.

Boundary approach in shape study of composite dowel shear connector

W. LORENC

Wrocław University of Technology, Wybrzeże Wyspiańskiego 27, 50-370 Wrocław, Poland

An approach for analysis of shape of composite dowel shear connector focused on finding a location of the point of maximal principal stress in steel dowel is presented. It is based on analogy between equations of boundary of closed area under plane stress conditions and beam in two dimensional space. Equations are derived from Airy's potential and polar coordinates are used.

Keywords: *composite dowels, steel dowels, numerical analysis*

1. Introduction

The VFT-WIB® construction method [1–3] represents a new technology in Europe using prefabricated composite beams with innovative type of shear force transfer mechanism. A new type of shear transmission – the composite dowel – allows composite girders without any upper steel flange and an enduring shear connection especially between high strength steel combined and high strength concrete and FRUHPC also [4]. The composite dowel is a co-product from the processing of rolled beams in steel construction without any additional resource (Figure 1).
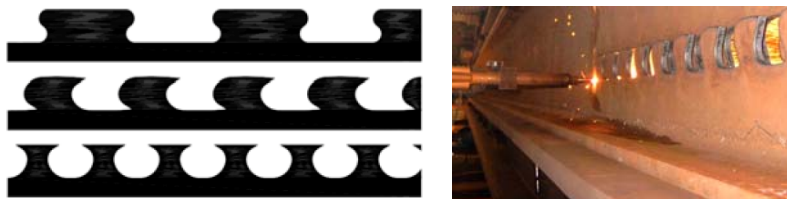
Fig. 1. Different cutting lines for composite dowels [4]
(Puzzle, Fin-cut, Tenon-shape) and cutting process

2. Subject of analysis and the method proposed

The object of work is to find a method to analyze location of point of maximum principal stress (maximum tension) by means of dowel shape and pressure distribution only. Contrary to currently used formulas for resistance of steel dowels based on plas-

tic distribution [5, 6] and FEM [7], this approach would be quite different and based on some analogies in equations of plates and beams [8]. Such a method, if successfully derived, would be efficient tool to solve some of problems considering shape of steel dowels and to prove generally some predictions from FEM analysis – some important aspects regarding cutting shape are still to be solved. It is logical to use some approaches considering boundary problems, as it is interesting to focus only on part of the edge, not the whole dowel. For simplicity that curve with constant radius is analysed at this stage and constant pressure profile. The method (if efficient) would be used for other shapes also, but rather circular arcs and clothoid curves are interesting from practical point of view. Nonlinear pressure profile is easy to introduce by some changes in equations. Uplift forces seem to be possible to include also.

From theory of elasticity [8] for plane stress

$$\frac{\partial^4 \Phi}{\partial x^4} + 2\frac{\partial^4 \Phi}{\partial x^2 \partial y^2} + \frac{\partial^4 \Phi}{\partial y^4} = 0, \tag{1}$$

can be expressed by means of polar coordinates:

$$\left(\frac{\partial^2}{\partial r^2} + \frac{1}{r}\frac{\partial}{\partial r} + \frac{1}{r^2}\frac{\partial^2}{\partial \theta^2} \right)\left(\frac{\partial^2 \Phi}{\partial r^2} + \frac{1}{r}\frac{\partial \Phi}{\partial r} + \frac{1}{r^2}\frac{\partial^2 \Phi}{\partial \theta^2} \right) = 0. \tag{2}$$

The problem of location of critical point (Figure 2) can be handled by means of study of σ_φ (if $\varphi = \theta$). Puzzle shape presented in Figure 2 is substituted by purely theoretical "full arc" shape for later analysis, just to simplify and clarify later FE study.
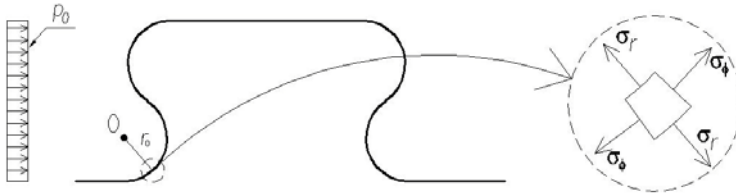
Fig. 2. Scheme of steel dowel with stress state at critical point

The radial stress is

$$\sigma_\varphi = \frac{\partial^2 \Phi}{\partial r^2}. \tag{3}$$

Assuming that only location of point *B* is important and the point *B* belongs to boundary **S** one can notice, that for extreme value of stress (changing with *s*) it should be satisfied

$$\frac{\partial \sigma_\varphi}{\partial s} = 0, \tag{4}$$

what leads to

$$\frac{\partial}{\partial s}\left(\frac{\partial^2\Phi}{\partial r^2}\right)\bigg|_{r=r_0} = 0.$$ (5)

There is connection between function Φ for closed area **V** with boundary **S** and internal forces in virtual beam of shape **S** and the same boundary loads what can be expressed:

$$\Phi(s) = M(s)$$
$$\frac{\partial\Phi}{\partial s} = N(s)$$, (6)

where M and N are bending moment and axial force in virtual beam, respectively (Figure 3).
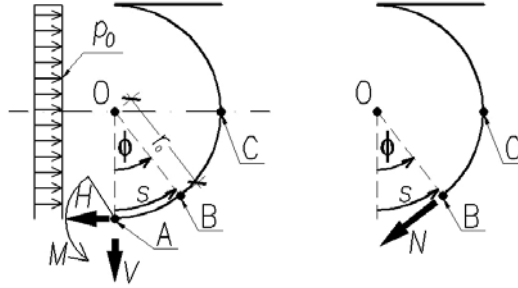
Fig. 3. Beam

With assumption that location of point B expressed by φ and r is of the same φ value for dowels of the same shape (so it does not dependent on size of dowel) and value of stress in point B is the same for the same p_0, Equation (6) may be reduced to:

$$\frac{\partial}{\partial\varphi}\left(\frac{\partial^2\Phi}{\partial r^2}\right)\bigg|_{r=r_0} = 0.$$ (7)

for $s = \varphi \times r_0$.

After substitution of second Equation of (6) to (7) equation for location of critical point B versus φ is:

$$\frac{\partial}{\partial\varphi}\left(\frac{\partial N}{\partial r}\right) = 0.$$ (8)

If assumed that dowels of different shapes (but the same p_0) and constant radius r_0 are under consideration (e.g. different puzzle shapes), one can notice that for every

particular shape, size effect would result in connection of internal force N (for different sizes) by means of linear function:

$$N\big|_{r_0} = N\big|_r \cdot \frac{r}{r_0}.$$
(9)

Hence for location of point B it would be enough to study shapes with one radius r_0 only and it results in equation for location of point B:

$$\frac{\partial N_0}{\partial \varphi} = 0.$$
(10)

One can notice it should be possible to determine φ_B on the basis of H_A, V_A and p_0 only. For every $B \in \mathbf{S}$ between points A and C (described by φ) according to Figure 3:

$$N_0 = H_A \cdot \cos(\varphi) - r_0 \int_0^\varphi p_0 \cdot \sin(\varphi) \cdot d\varphi + V_A \cdot \sin(\varphi),$$
(11)

$$N_0 = H_A \cdot \cos(\varphi) - r_0 p_0 \cdot \big(1 - \cos(\varphi)\big) + V_A \cdot \sin(\varphi),$$
(12)

what after substitution to (10) gives

$$\frac{\partial N_0}{\partial \varphi} = -H_A \cdot \sin(\varphi) - r_0 p_0 \cdot \sin(\varphi) + V_A \cdot \cos(\varphi) = 0,$$
(13)

that leads to equation for location of point B:

$$\mathrm{tg}(\varphi_B) = \frac{V_A}{H_A + r_0 \cdot p_0},$$
(14)

where H_A and V_A are calculated for radius r_0 and p_0 is a constant value.

3. Numerical study

Numerical study was conducted to check method proposed and to study any practical difficulties. One particular dowel shape with constant geometry was analysed ("full arc" shape) under four loadcases (different level of resultant force and pressure/no pressure next to B point). Three types of FE models were necessary to study: M1 – beam model e^1, p^2 (shape of boundary $\mathbf{S}$), M2 – shell model e^2, p^2 (shape body $\mathbf{V}$ with boundary $\mathbf{S}$) M3 – shell model e^2, p^2 (dowel connected to almost infinite space). They are presented in Figures 4 and 5.
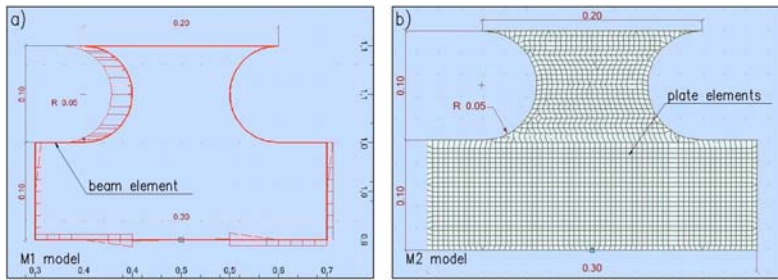
Fig. 4. M1 model and M2 model
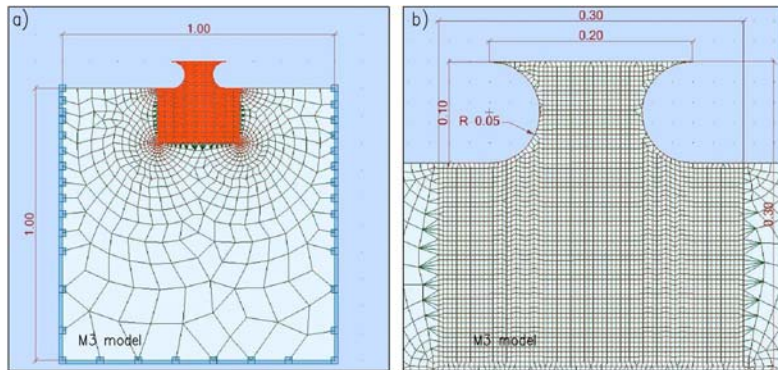
Fig. 5. M3 model: a) whole model and b) dowel region
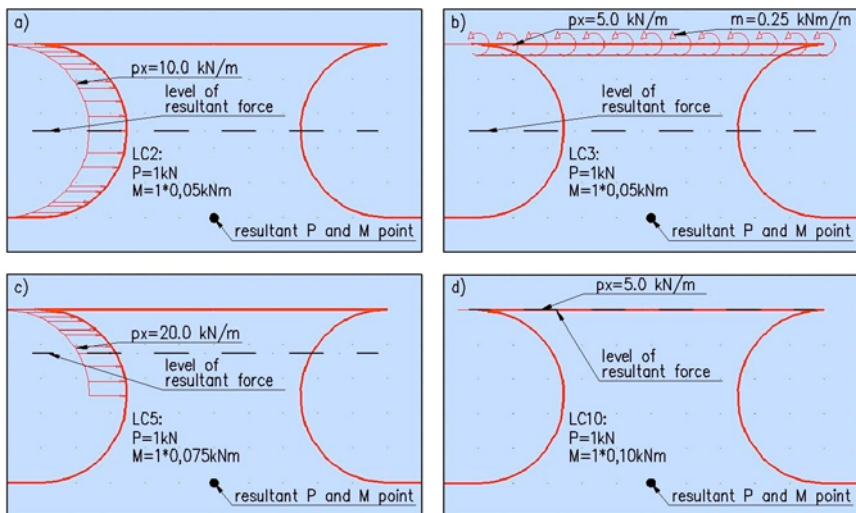
Fig. 6. Load cases: a) constant pressure at whole dowel height, b) constant line load
with moment distributed along the edge, c) constant pressure at upper part
of dowel – half of dowel height d) constant line load

Total force value per dowel is:

$$P = \int_S p_0 dy. \tag{15}$$

The study was conducted for every of four loadcases as follows:

1. Calculation of M3 models with external loads acting the dowel to obtain the stress fields.

2. Study of σ_x, σ_y and τ_{xy} stresses distribution at cuts created in M3 model. The cuts are (geometrically) boundary edges of M1 and M2 models.

3. Defining the external forces according to assumption of distribution of p and t according to Figure 7. Distribution of p and t represents external forces for M1 and M2 models. It should be similar to distribution of σ_x, σ_y and τ_{xy} stresses from M3 model and it must fulfil equations of equilibrium of global forces acting on model, hence for support point $R_x = R_y = M_z = 0$.

4. Study of M2 models with distributions of p and t and external loads acting the dowel. Comparative study of principal stress distribution and their extreme values for M2 and M3 models – they must be comparable in dowel region to claim that boundary geometry and p and t are proper approximation of M3 model.

5. Study of M1 (beam) model focused on internal loads distribution, especially axial forces. Determination of H_A and V_A.

6. Determination of φ_B on the basis of H_A and V_A from (14) what should be confirmed by location of maximal axial force for M1 model (graphically).
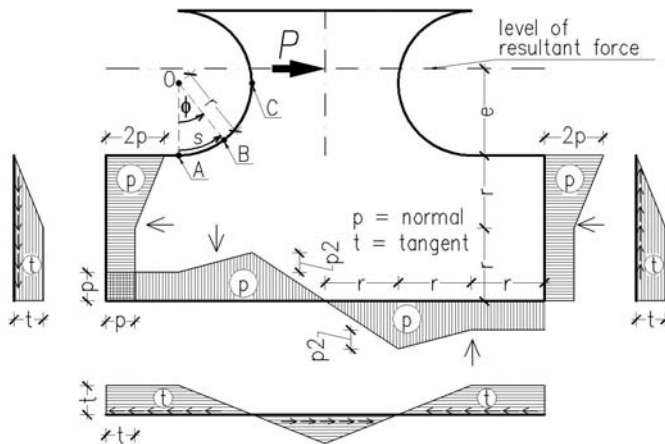
Fig. 7. Distribution of p and t

With assumption that $p = t$ ($\tau_{xy} = \tau_{yx}$ at lower corners) and from $\Sigma X = 0$, $\Sigma M_Z = 0$ it can be derived for scheme presented in Figure 7:

$$p = \frac{1}{7}\frac{P}{r}, \tag{16}$$

$$p_2 = \frac{P}{r}\left(\frac{e}{2 \cdot r} - \frac{2}{3}\right). \tag{17}$$

Forces distribution presented in Figure 7 is one of many possible solutions – it is linear approximation of nonlinear stress distribution. It was chosen on the basis of stress distributions from Figures 8, 9, 12 and 13 and it fulfils some basic conditions like symmetry, etc.

4. Results

Results are presented in Figures 8–12, angle φ_B from (14) for forces from M1 model is presented in Table 1. Straight line tangent to arc and crossing point described by symmetry axis of dowel and level of resultant force is shown in addition.

Table 1. φ_B from Equation (14), LC = loadcase number

LC	P [kN]	$\underline{e}$ [m]	H_0 [kN]	V_0 [kN]	r_0 [m]	p_0 [kN/m]	$r_0 \times p_1$ [kN]	tg (ϕ)	ϕ_B [^{0}]
2	1	0.05	0.614	0.254	0.05	10	0.5	0.2280	12.8
3	1	0.05	0.5	0.219	0.05	–	–	0.4380	23.7
5	1	0.75	0.553	0.342	0.05	–	–	0.6184	31.7
10	1	0.10	0.5	0.436	0.05	–	–	0.8720	41.1

H_0 and V_0 in Table 1 are obtained from M1 model at point A.
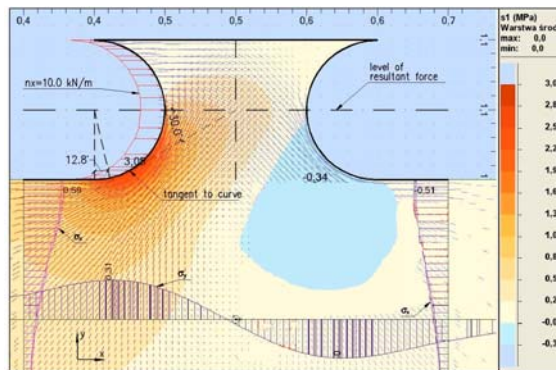
Fig. 8. Model M3, loadcase 2: principal stress σ_1, normal stress σ_y and σ_x distribution at cuts
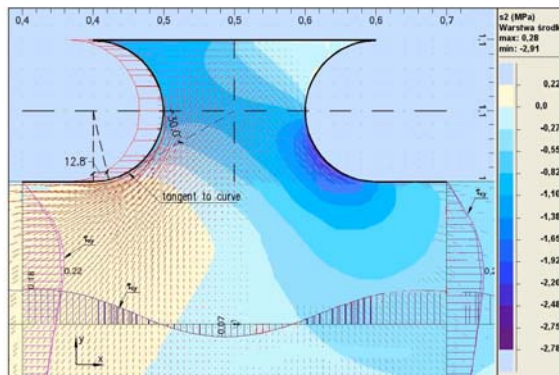
Fig. 9. Model M3, loadcase 2: principal stress σ_2, shear stress τ_{xy} and τ_{yx} distribution at cuts
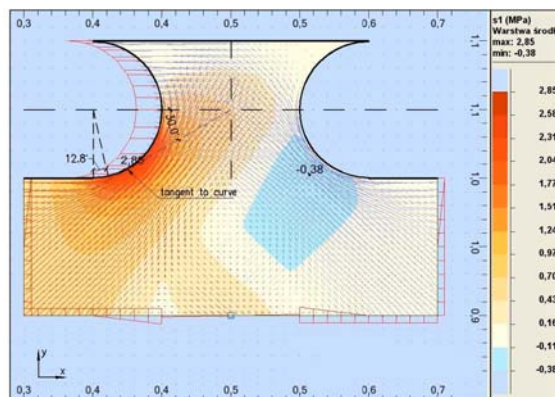
Fig. 10. Model M2, loadcase 2: principal stress σ_1
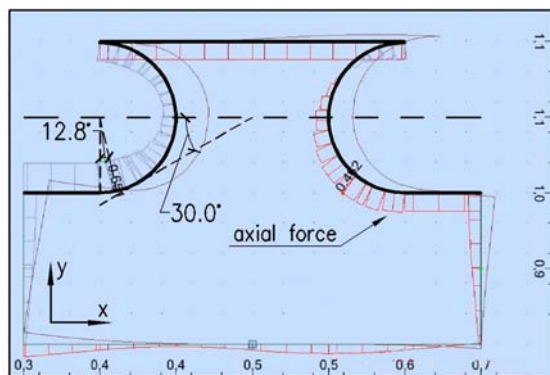
Fig. 11. Model M1, loadcase 2: axial force
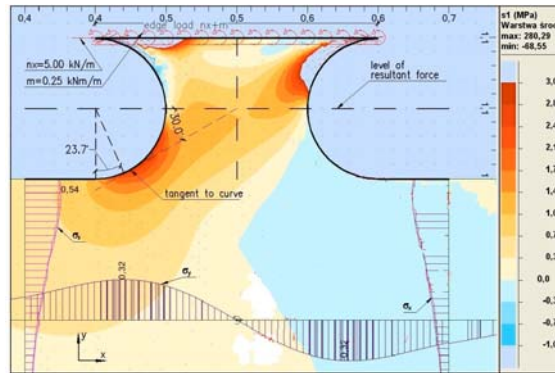
Fig. 12. Model M3, loadcase 3: principal stress σ_1, normal stress σ_y and σ_x distribution at cuts
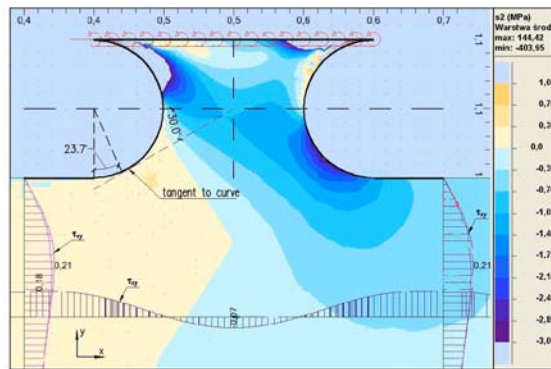
Fig. 13. Model M3, loadcase 3: principal stress σ_2, shear stress τ_{xy} and τ_{yx} distribution at cuts
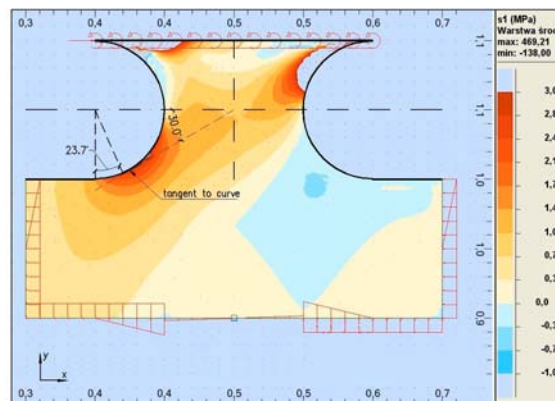
Fig. 14. Model M2, loadcase 3: principal stress σ_1
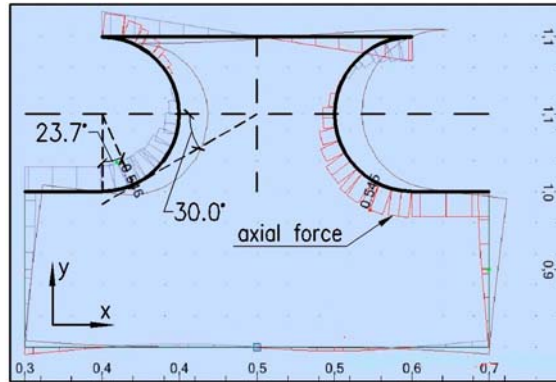
Fig. 15. Model M1, loadcase 3: axial force
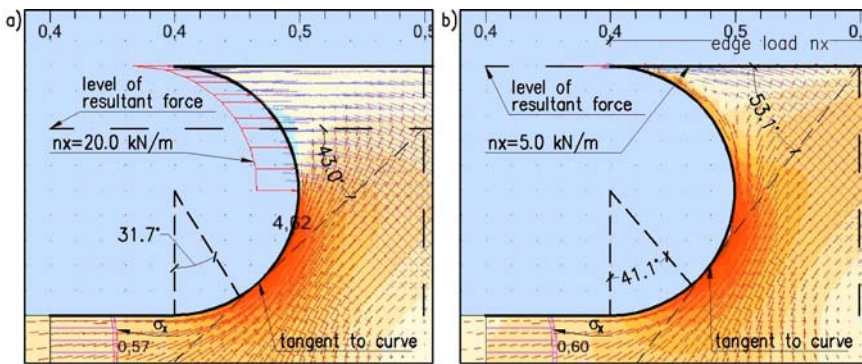
Fig. 16. Model M3, principal stress σ_1, a) loadcase 5 and b) loadcase 10

5. Interpretation of the results

Stress layouts, extreme values of main principal stress and their location (point *B*) are similar for M2 and M3 models, hence M2 model seems to be good approximation of M3 model ($B(s)|M_3 \approx B(s)|M_2$ both for value and location). For all four loadcases point *B* calculated by new approach from (14), ($B(s)|M_1$), with M1 model is situated lower than one from M3 model. Moreover, straight line tangent to arc and crossing point described by symmetry axis of dowel and level of resultant force is tangent to arc (point *T*) between points $B(s)|M_1$ and $B(s)|M_3$. Hence results of new approach confirms some logical predictions (eg. higher *e* value – higher location of *B* point) and their show regularities like $B(s)|M_1 \rightarrow T \rightarrow B(s)|M_3$, but exact location of $B(s)|M_1$ is too low. One should notice, that external loads of M1 model presented in Figure 7 are not the same as stress distribution in model M3 (Figures 8, 9, 12, 13), what is important factor for sure. Geometry of M1 model is only one of many possible solutions and

maybe it should be set in a different way; some basis should be figured out and limitations of Airy's stress functions may be important.

6. Summary

An approach for analysis of shape of composite dowel shear connector focused on finding a location of the point of maximal principal stress in steel dowel has been presented. It is based on analogy between equations of boundary of closed area under plane stress conditions and beam in two dimensional space. Equations are derived from Airy's potential and polar coordinates are used. The approach presented at this stage should be treated rather as an outline of the method proposed. The important point is to choose appropriate geometry of M1 model and external loads distribution. Expressing external loads by means of continuous functions and appropriate geometry of M1 model (if possible) could lead to reduction of complex task to functional problem or maybe even to algebraic one. Hence it could result in efficient tool to solve theoretically many problems regarding shape of steel dowels in aspect of stress distribution.

References

[1] Schmitt V., Seidl G., Hever M.: *Composite bridges with the VFT-WIB construction method – robust and long lasting*, Compendium Eurosteel, Maastricht, Netherlands, 2005.
[2] Seidl G.: *VFT-WIB-Construction Method*, Compendium 5th Japanese-German Joint Symposium for Composite Bridges, Munich, 2005.
[3] Schmitt V., Seidl G., et al.: *Verbundbrücke Pöcking – Innovative VFT-Träger mit Betondübeln, Composite bridge Pöcking – Innovative VFT-girder with steel dowels*, Stahlbau 06, 2004.
[4] Seidl G., Schmitt V., Lorenc W.: *Shear Transmission of Fibre Reinforced Concrete Dowels*, The 7th German-Japanese Bridge Symposium, 30 July–1 August, Osaka, Japan, 2007.
[5] Zapfe C.: *Trag- und Verformungsverhalten von Verbundträgern mit Betondübeln zu Übertra-gung der Längsschubkräfte*, Doctoral thesis, Univer-sität der Bundeswehr, München, 2001.
[6] Hegger J., Feldmann M., Rauscher S., Hechler O.: *Bericht P 621 / AiF-Nr. 13867 – Verbundmittel in hochfestem Beton*. Aachen, 2007.
[7] Lorenc W., Ignatowicz R., Kubica E., Seidl G.: *Numerical model of shear connection by concrete dowels. Recent Developments in Structural Engineering Mechanics and Computation*, Millpress, Rotterdam, Netherlands, 2007.
[8] Timoshenko S, Goodier J.N.: *Theory of elasticity*, McGraw-Hill Book Company, Inc. 1951.

Podejście brzegowe w analizie kształtu zespolenia typu „composite dowels"

W artykule przedstawiono metodę umożliwiającą określenie położenia punktu maksymalnych naprężeń w stalowej części zespolenia typu „composite dowels". Podano podstawy teo-

retyczne, rozwiązano numerycznie wybrane problemy, porównano wyniki i przedstawiono wnioski. Metoda wykorzystuje analogię pomiędzy równaniami brzegu zamkniętego obszaru w płaskim stanie naprężeń a belką w przestrzeni dwuwymiarowej. Równania wyprowadzono wykorzystując funkcję Airye'go i współrzędne biegunowe. Proponowana metoda jest na obecnym etapie szkicem podejścia, istotne jest dobranie odpowiedniej geometrii modeli wycinkowych i rozkładu obciążenia zewnętrznego jako warunków brzegowych, najlepiej w postaci funkcji ciągłych. Jeżeli byłoby to możliwe, to skomplikowane obecnie zagadnienie najprawdopodobniej sprowadziłoby się do problemu analizy funkcjonału i możliwe byłoby zbudowanie efektywnego narzędzia matematycznego do rozwiązywania wielu problemów dotyczących kształtu zespolenia w aspekcie rozkładu naprężeń w części stalowej.

Application of internal variable convection
for modelling of T-shape mould filling

P. MACIOŁ

AGH – University of Science and Technology, al. Mickiewicza 30, 30-059 Kraków, Poland

Numerical methods for thixoforming modelling are shortly reviewed in the paper. Present applications, especially for thixotropy phenomena modelling, are presented. Advantages and disadvantages of methods based on solid mechanics or computational fluid dynamics are pointed out. Internal Variable Convection (IVC) method is introduced as an alternative for classical Lagrangian or Eulerian methods.

Numerical simulations of T-shape mould filling, based on the data taken from literature, are shown. Presented results confirm possibilities of thixoforming processes modelling with Internal Variable Convection method. However, some deficiencies of the present solution are pointed out in the paper as well. It concerns mainly material front tracking methods and treatment of boundary layer. Some ways to resolve existing constraints, as well as plans for future are presented.

Keywords: *thixoforming, internal variable convection, numerical modelling, computational fluid dynamice*

1. Introduction

Semi-solid forming processes, like thixoforming, rheocasting, some continuous casting variants and some others, combine phenomena from fluids and solids behaviour. High deformations and time dependent properties of materials cause that neither structural, nor fluids computational methods are fully applicable. Structural solutions are commonly based on Lagrangian motion description and remeshing is required when mesh becomes too distorted. Remeshing dramatically increases time consumption and decreases accuracy of solution. On the other hand, Computational Fluid Dynamics (CFD) methods, based on Eulerian or ALE motion descriptions, are not suitable for behaviour modelling of history dependent materials. Nevertheless, CFD solutions seem to be more flexible and more promising than based on Lagrangian description. The objective of the paper is to suggest an alternative approach, which is based on the convection of the internal variable.

1.1. Thixoforming modelling

Thixoformed materials are usually described as viscoplastic or elastoviscoplastic (Bellet & Moto Mpong [1], Kopp et al [2]), as well as shear-thinning fluids or Hershel-Bulkley fluid (Huilgol, You [3]; Alexandrou [4]). Compatibility of CFD methods with

viscous, non-Newtonian fluids and structural mechanics based solutions with viscoplastic material was proved by Zienkiewicz and Cormeau [5]. However, in solid computations, dynamic effects are usually omitted. In high speed forming, like thixoforming, dynamic effects are significant, what had been shown by Sołek et al. [6]. Moreover, due to high deformations, solid mechanics based methods need remeshing. It entails high numerical errors and high costs of computations. It is a reason that, despite some disadvantages, the majority of researchers uses CFD methods for thixoforming modelling.

When CFD techniques are employed, thixotropic effects are one of the most important obstacles. These phenomena are connected with long lasting variations of rheological parameters after changes of the flow conditions. Detailed description of this problem could be found in the paper of Muyumdar et al. [7]0. Numerical modelling of rheological parameters dependency on process history needs storage of material state in computational domain. Unfortunately, it is not possible, when classical CFD methods are applied. More detailed description of this subject is presented by Macioł [8].

2. Numerical model of thixotropy

There are several models of thixotropic behaviour described in the scientific literature. Wide review could be found in publications of Atkinson [10], Mujumdar et al. [7] and Barnes [9]. Presently, two families of thixotropy models are used, direct and indirect. Direct models are better grounded on physical basis, but its application requires determination of some thixotropic fluid parameters. It could be extremely difficult, especially for high temperatures, which are typical for thixoforming processes. Indirect models parameters could easily be nominated with inverse method, which makes them easier for practical application. The main measure of thixotropy effects in those models is agglomeration coefficient λ Muyumdar et al. [7]).

In this paper, a modification of indirect model proposed by Modigell and Koke [11] is employed:

$$\frac{d\lambda}{dt} = ae^{-b\dot{\gamma}}\left[\lambda_e(\dot{\gamma}) - \lambda\right] \tag{1}$$

$a = a^+$ when $\lambda_e(\dot{\gamma}) - \lambda \geq 0$

$a = a^-$ when $\lambda_e(\dot{\gamma}) - \lambda < 0$

where:
  a^+, a^- and b – constants,
  λ_e – equilibrium structural parameter,
  λ – structural parameter,

$\dot{\gamma}$ – shear rate. In original Modigell–Koke equation, both a^+ and a^- coefficients are equal.

Relationship between viscosity and structural parameter is based on equation:

$$\mu = \mu_0(f_s) + e^{cf_s} d\lambda\dot{\gamma}^m, \tag{2}$$

where:

c, d and m – constants,

μ – viscosity,

μ_0 – viscosity when $\dot{\gamma} \to \infty$,

f_s – solid fraction. In this work, only constant solid fraction is taken into account, so μ_0 and e^{cfs} are constant. Equilibrium structural parameter is described by equation

$$\lambda_e = \frac{1}{1+(\alpha\dot{\gamma})^n}, \tag{3}$$

where $\alpha = 1$ second and n is a coefficient.

3. Internal variable convection (IVC)

IVC methodology is an attempt to overcome difficulties with modelling of history dependent materials with CFD. Description of basic assumptions of this methodology can be found in works of Macioł [8] [12]. These assumptions are repeated briefly below.

IVC is based on convection of "artificial species", which represents internal variable, similarly to mass transfer problems. Convection of the physical quantities (like volume or solid phase fraction) is introduced in the presently available publications. On the contrary, the convection of the state variable (aggregation coefficient) is used in the present solution. Numerical solution of one time step in transient simulation is divided into two steps – computation of velocity field and subsequently IV convection. If flow parameters (viscosity) are strongly dependent on internal variable distribution, these steps could be iteratively repeated for the quasi-stationary solution.

For the first step, whichever transient CFD method could be employed (Streamline-Upwinded Petrov Galerkin, Characteristic Based Split (CBS) and many others). Second step is typical convection problem with known velocity field. IV changes in time are included with a source mechanism. Reassuming, IVC methodology allows simulation of transient flows of history dependent materials, with arbitrary geometry, taking into account both IV convection and IV variations with time and flow parameters. From numerical point of view, IVC method is identical with coupled problem of fluid flow with mass transport, when fluid viscosity is dependent on mass fraction. The main difference is in treatment of a "mass" – a real species in mass transfer and internal variable in IVC.

4. Numerical results

Computer program CompFlower, based on the IVC methodology, has been developed. It is written in C++ language, but some advanced techniques, like policy based programming and metaprogramming allow keeping high efficiency of the code. Navier–Stokes equations, as well as convection problem are solved with Characteristic Based Split algorithm (Zienkiewicz & Taylor [13]). PETSc library is employed for linear equation system solving. Some numerical tests confirms robustness of the CompFlower code (Macioł 2008).

4.1. Thixotropy modelling

The main task of the CompFlower software is thixotropy modelling. In order to validate the program's capability to model thixotropy, numerical model of the Modigell & Koke experiment [14] was performed. Viscosity and internal variable derivative are computed with equations (1–3). Computations for a series of shear jumps and drops, identical with those shown in the mentioned paper, were carried out. Computational results, compared with experimental data, are presented in Figure 1.
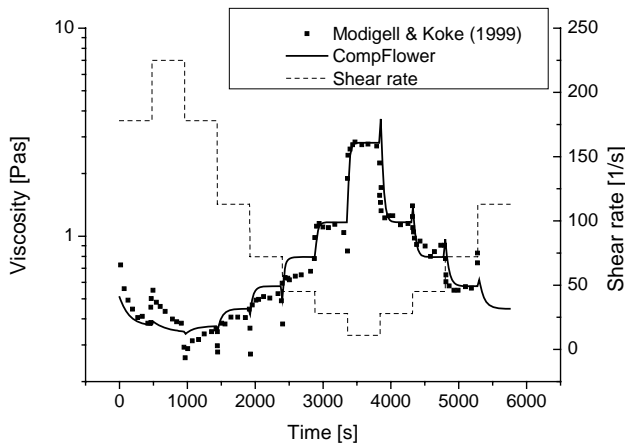
Fig. 1. Comparison of experimental and computed viscosities in shear jump/drop test

Thixotropic behaviour, shown by Modigell & Koke [11] are revealed in two effects. Firstly, delay of reaching equilibrium shear stress when shear rate jumps or drops occur. Secondly, short peaks or pits appear after shear jumps or drops. Classical CFD methods are unable to replicate those effects. As it could be seen in Figure 1, IVC technique gives such a possibility. Differences between experimental and numerical results in high shear stress are caused by numerical model's imperfections. Model's coefficients were chosen manually and could be still optimized with automatic methods, such us inverse method.

Although numerical and experimental data are not completely agreeable, viscosity peaks and pits are predicted properly.

4.2. T-shape form filling

The majority of thixoforming processes is connected with mould filling. Present work is inspired with the experiment presented by Modigell et al. [14]. The shape of computational domain is shown in Figure 2.
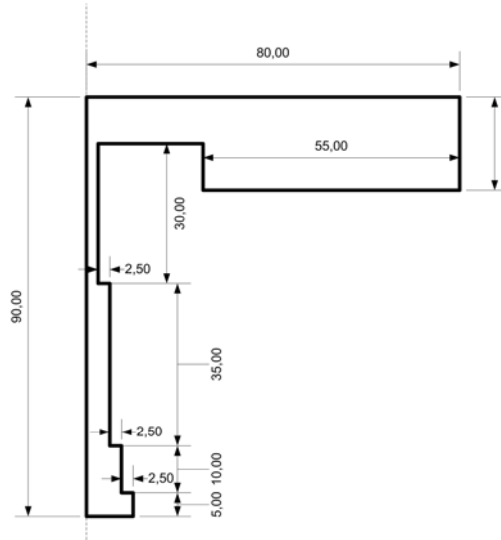
Fig. 2. Dimensions of the T-shape mould

Transient model was designed to check whether the IVC methodology can be successfully used for numerical modelling of mould filling with thixotropic fluid. Unfortunately, CompFlower software has some constraints. The main two issues are simplifications in front tracking and some problems with boundary layer. Front tracking algorithm is based on IVC methodology. IV values can vary in the range [−1; 1]. When value is less than zero, it is assumed, that there is no fluid in this element. In such a case, rheological model describes an air and IV corrections have only convective character. When IV is grater than zero, element is assumed to be filled with liquid metal. Then, full IVC metod is applied, with both convective and source based mechanisms of IV changes. There is no special treatment of boundary layers.

Computations for the three inlet pressures were carried out. In all cases, mould initially was filled with air. No-slip conditions were assumed on boundaries and zero-pressure condition on outlet. Distributions of the IV value for inlet pressure of 1000 Pa is presented in Figure 3. Distributions of the IV values in selected time steps for inlet pressure equal to 300 Pa and 1700 Pa are shown in Figure 4.

$t = 0.25$ s $t = 0.75$ s
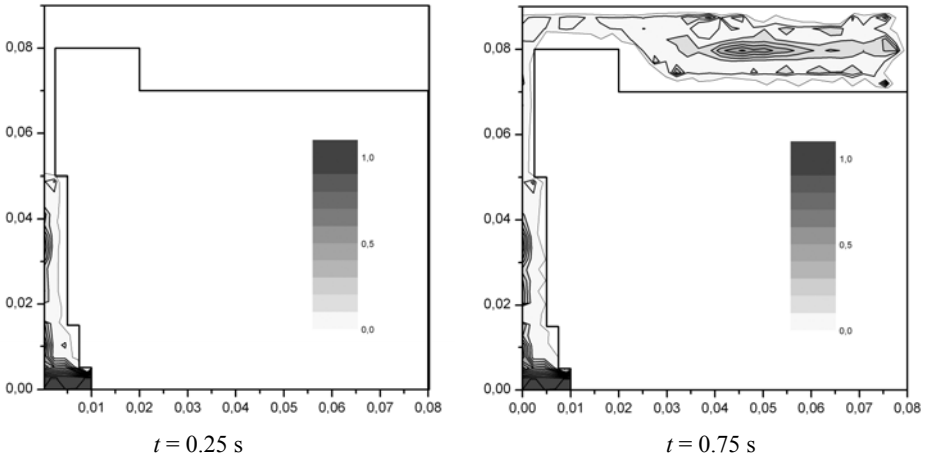
Fig. 3. Internal variable values for following time steps
(inlet pressure equal to 1000 Pa)

a) $p = 300$ Pa, $t = 2.0$ s   b) $p = 1700$ Pa, $t = 0.5$ s
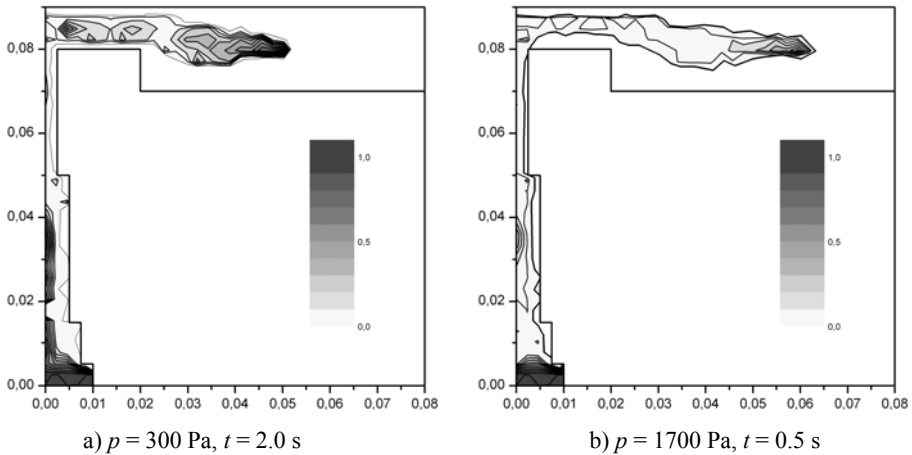
Fig. 4. Internal variable values for chosen time steps
(inlet pressure equal to 300 Pa (a) and 1700 Pa (b))

Computed flow front could be compared with experimental results presented by Modigell et al. [14] (Figure 5). Piston velocity in experiment is approximately 20% lower than in computations with inlet pressure equal to 1700 Pa. Computational and experimental results are generally agreeable. Differences are caused mainly by mentioned simplified boundary layer treatment, front tracking method and some artificial diffusion, necessary to obtain convergence in numerical solution.

Presented results show that inlet pressure in given range has no significant influence on flow directions. Of course, since forming speeds are dependent on inlet pressure, this conclusion cannot be extrapolated to higher or lower pressures. On the other hand, the

higher pressure in inlet constraints higher shears. It could be seen, that internal variable values are lower, when forming speeds are higher. It is in agreement with the expectations and confirms good predictive capabilities of the IVC based model.

The main disadvantage of developed model is a boundary layer. Homogenous finite element mesh, no-slip condition and fluid motion tracking with internal variable effects with artefacts on boundary layer – the gap between formed material and the walls.
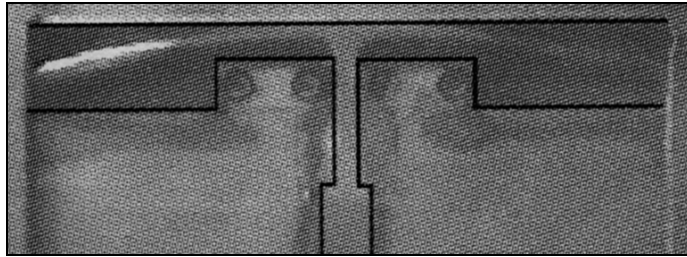
Fig. 5. Flow front of an isothermal filling experiment, v_{piston} = 50 mm/s; source: Modigell et al. [14]

5. Conclusions

With IVC methodology, it is possible to simulate flows of fluids, which rheological parameters are dependent on processes history. Such an approach is not possible with classical CFD techniques. IVC can be used for both steady-state and transient cases. Transient mould filling simulations are possible as well. However, presently used front tracking method and boundary layer solution are strongly simplified. This is an obstacle in obtaining fully reliable results. Presently it is not possible to quantitatively compare numerical and experimental results. It is necessary to further improve the developed software. Although, it is only a technical problem. Hitherto results clearly prove that IVC methodology can be efficiently used for modelling of any flows of history dependent fluids.

Acknowledgements

References

[1] Bellet M., Moto Mpong S.: *Determination of the constitutive equation parameters of a thixotropic Al alloy and FEM modelling of the thixoforming process*, Proc. Conf. NUMIFORM 2001, in: *Simulation of Materials Processing: Theory, Methods and Applications*, Toyohashi, ed. Mori, K., ToyohashiLisse, 2001, pp. 1087–1092.
[2] Kopp R., Choi J., Neudenberger D.: *Simple compression test and simulation of an Sn15% Pb alloy in the semi-solid state*, J. Mater. Process. Technol., Vol. 135, No. 2–3, 2003, pp. 317–323.

[3] Huilgol R.R., You Z.: *Application of the augmented Lagrangian method to steady pipe flows of Bingham, Casson and Herschel–Bulkley fluids*, J. Non-Newton. Fluid Mech., Vol. 128, No. 2–3, 2005, pp. 126–143.

[4] Alexandrou A. N.: *Constitutive modelingmodelling of semisolid materials*, Proc. 4th Int. Con. on Semi-Solid Processing of Alloys and Composites, Sheffield, 1996, pp. 132–136.

[5] Zienkiewicz O. C., Cormeau I. C.: *Viscoplasticity – plasticity and creep in elastic solids – a unified numerical solution approach*, Int. J. Numer. Methods Eng, Vol. 8, 1974, pp. 821–845.

[6] Sołek K., Stuczyński T., Białobrzeski A., Kuziak R., Mitura Z.: *Modelling thixocasting with precise accounting of moving front of material*, Mater. Sci. Technol., Vol. 21, No. 5, 2005, pp. 551–558.

[7] Mujumdar A., Beris A. N., Metzner A. B.: *Transient phenomena in thixotropic systems*, J. Non-Newton. Fluid Mech., Vol. 102, 2002, pp. 157–178.

[8] Macioł P.: *Application of internal variable convection method for thixotropy modelling*, Steel Res. Int., 79, special edition Metal Forming Conf., 2008, pp. 332–339.

[9] Barnes H.: *Thixotropy – a review*, J. Non-Newton. Fluid Mech., Vol. 70, 1997, pp. 1–33.

[10] Atkinson H.V.: *Modelling the semi-solid processing of metallic alloys, major invited review*, Progress in Materials Science, Vol. 50, No. 3, 2005, pp. 341–412.

[11] Modigell M., Koke J.: *Time-dependent rheological properties of semi-solid metal alloys*, Mechanics of Time-Dependent Materials, Vol. 3, 1999, pp. 15–30.

[12] Macioł P.: *Zastosowanie algorytmu Characteristic Based Split oraz konwekcji zmiennej wewnętrznej do modelowania przepływów cieczy tiksotropowych*, Proc. Conf. "Informatyka w Technologii Metali Komplastech 2008", 2008, pp. 177–184 (in Polish).

[13] Zienkiewicz O. C., Taylor R. E.: The Finite Element Method, Butterworth-Heinemann, Oxford, 2000.

[14] Modigell M., Hufschmidt M., Petera J.: *Two-phase simulations as a development tool for thixoforming processes*, Steel Res. Int., Vol. 75, 2004, pp. 513–518.

Zastosowanie metody konwekcji zmiennej wewnętrznej do modelowania wypełnienia formy T-kształtnej

W pracy omówiono metody komputerowe obecnie stosowane do modelowania procesów tiksoformingu, ze szczególnym uwzględnieniem zjawiska tiksotropii. Analizowano zagadnienia związane z modelowaniem przepływów cieczy tiksotropowych przy zastosowaniu opisu kinetyki Lagrange'a lub Eulera. Zaproponowano nową metodę konwekcji zmiennej wewnętrznej, która pozwala na modelowanie takich przepływów w oparciu o rozwiązanie zagadnienia konwekcji dodatkowo wprowadzonej zmiennej, opisującej stan materiału.

Przedstawiono symulacje procesu wypełnienia formy T-kształtnej, oparte na doświadczeniu opisanym w literaturze. Przedstawione wyniki potwierdzają możliwość modelowania procesów tiksoformingu w oparciu o metodę konwekcji zmiennej wewnętrznej. W artykule przedstawiono jednak także istotne niedoskonałości obecnie stosowanej metodyki, szczególnie w zakresie modelowania frontu materiału i warstwy przyściennej. Wskazano również perspektywy rozwoju metody i kroki planowane w celu poprawy jakości rozwiązania.

Fatigue notch factor in steel bridges due to corrosion

Y. SHARIFI, R. RAHGOZAR

Civil Engineering Department, University of Kerman, Kerman, Iran
P.O. Box: 76169-133, e-mail: yasser_sharifi@yahoo.com; rahgozar@mail.uk.ac.ir

In this paper the main aspects that are associated with stress concentration created by corrosion are reviewed and separate functions are produced for fatigue notch factor in terms of average corrosion penetration and exposure time. In particular, the relation of fatigue notch factor in terms of exposure time gives a direct, accurate, and quantifiable assessment of corroded members and it needs only the time of weathering. Finally the fatigue notch factor of corroded steelwork compared with the fatigue notch factor of various classes of structural detail as classified in BS 5400, the UK code requirements for fatigue.

Keywords: *fatigue notch, corrosion, fatigue life, exposure time, steel bridges*

Nomenclature

d_c [mm]   – average corrosion penetration,
K [–]   – constant term relating to mean-line of $\log \sigma_r – \log N$ curve,
K_f [–]   – fatigue notch factor,
K_{fc} [–]   – fatigue notch factor due to corrosion,
m [–]   – inverse slope of the mean-line $\log \sigma_r – \log N$ curve,
N [–]   – number of cycles,
$\sigma_{r,B}$ [MPa]   – stress range for class B,
$\sigma_{r,C}$ [MPa]   – stress range for class C,
$\sigma_{r,x}$ [MPa]   – stress range for class x,
$R_{\max}$ [mm]   – maximum roughness,
S_d [mm]   – standard deviation of roughness,
t [year]   – exposure time.

1. Introduction

Steel bridges are susceptible to pitting corrosion when subjected to severe environments. The pits which result from pitting corrosion can be dangerous because they extend into the metal, showing little external evidence of their existence, and are usually confined to a point or small area. In practice, any fatigue life assessment must include an understanding of the effects of notch geometry and the associated stress field on both the crack formation and subsequent propagation phase of life. The geometrical discontinuities which create stress concentrations are frequently responsible for providing the origin of fatigue crack formation in engineering structures. There is voluminous literature in the field of pitting corrosion and corrosion fatigue [1–5]. But the amount of published work on fatigue notch factor due to corrosion is limited. Albrecht et al. [6] identified three significant fac-

tors which contribute to the total reduction in fatigue strength of a corroded member. Accordingly, the fatigue notch factor or fatigue strength reduction factor is equal to the product of all factors. However, for simplicity Albrecht combined these factors as a single factor, known as the fatigue strength reduction factor. This factor is an appropriate parameter for quantifying the effect of corrosion deterioration on fatigue strength which can be calculated for each specimen on the basis of applied stress range and the number of cycles to failure. The most commonly accepted definition of fatigue notch factor is the ratio of the fatigue strength of a smooth specimen to that of a notched specimen under the same experimental conditions and the same number of cycles [7]. The main goals in this paper are: (1) to review the main aspects that are associated with stress concentration created by corrosion, (2) develop of a function which could represent fatigue notch factor in terms of average corrosion penetration, (3) development of a relation for fatigue notch factor in terms of exposure time and (4) to investigate the fatigue notch factor of corroded steelwork compared with the fatigue notch factor of various classes of structural detail as classified in BS 5400, the UK code requirement for fatigue. In this research the results obtained for roughness measurements of corroded steelwork and cyclic tests have been used from Rahgozar [8] to develop the required relationships for fatigue notch factor.

2. Methods of calculating fatigue notch factor

The presence of discontinuities or pits on the surface of steel structural members due to corrosion can result in a lower S-N curve. The reason for this is the stress concentration at the root of the pit which promotes the initiation of cracks which reduce the fatigue life. The effect of stress concentrations on fatigue resistance can be quantified by using a fatigue stress concentration factor or fatigue notch factor.

Two approaches for determining fatigue notch factors can be considered. The first requires testing smooth specimens, then utilising the Neuber's rule [9] to calculate the fatigue notch factor based on the number of cycles to failure for corroded specimens. The second involves a comparison between test results for corroded specimens and a mean regression line for stress range versus cycles to failure in plain rolled beams. The regression line which was used in the comparison is the same one used in BS 5400: Part 10 [10] for allowable stress range for class B (plain rolled beam) fatigue detail. Further discussion regarding the second approach is presented in this section.

The severity of various classes of structural detail in BS 5400: Part 10 [10] can be expressed in terms of fatigue notch factors, k_f, before considering corrosion. It is more meaningful to select the fatigue strength of the plain rolled beam as the reference line for which the fatigue notch factor is then defined as unity, $k_f = 1.0$. The fatigue notch factor for any other class x is then equal to the ratio between the stress ranges for the class B and class x means at a fixed number of cycles, as shown in Figure 1.

$$k_f = \left(\frac{\sigma_{r,B}}{\sigma_{r,x}} \right).$$

(1)
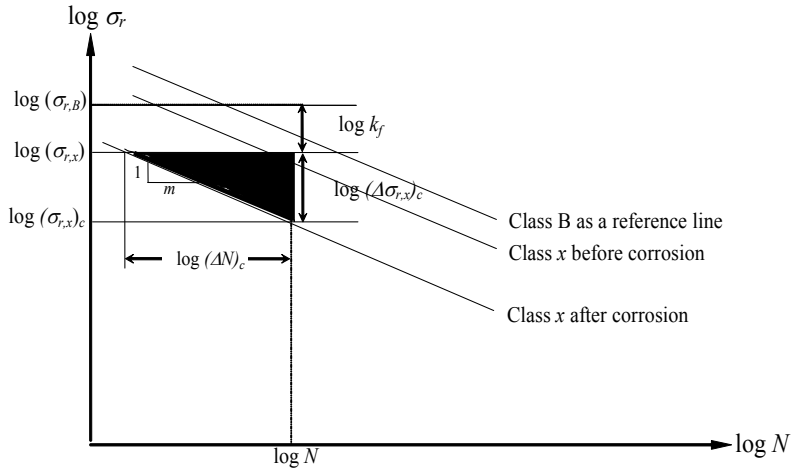
Fig. 1. Definition of fatigue notch factor and computation of loss in stress range and fatigue life

Table 1. Calculation of fatigue notch factors for mean lines of BS 5400

Detail Class	K	m	σ_r at 500.000 cycles	k_f at 500.000 cycles
B	2.34×10^{15}	4.0	262	1.00
C	1.08×10^{14}	3.5	241	1.09
D	3.99×10^{12}	3.0	200	1.31
E	3.29×10^{12}	3.0	189	1.39
F	1.73×10^{12}	3.0	151	1.74
F2	1.23×10^{12}	3.0	135	1.94
G	0.57×10^{12}	3.0	105	2.50
W	0.37×10^{12}	3.0	91	2.88

Since the slopes of the eight mean regression S–N lines vary, the fatigue notch factors were computed at 500.000 cycles of loading, which is about the logarithmic mean of the number of cycles to failure of the beams tested by Fisher et al [11] that form the basis of the design requirement in the Standard Specification of Highway Bridges. This reference ($N = 500.000$ cycles) is about midway on the range of N for which test data exist and has been used extensively by different authors [12–14]. The stress ranges for different classes listed in Table 1 (more details can be found in Reference [15]). Dividing these stress ranges into 262 MPa, the stress range for class B yields k_f in accordance with equation 1 (Table 1 and Figure 1).

3. Calculation of fatigue notch factor for corroded specimens

Fatigue notch factor due to corrosion, k_{fc}, can be defined as the ratio of the stress range of a non-corroded base metal, $(\sigma_{r,x})$, to the stress range of the same metal with corrosion, $(\sigma_{r,x})_c$, under the same experimental conditions.

$$k_{fc} = \frac{(\sigma_{r,x})}{(\sigma_{r,x})_c}. \tag{2}$$

Table 2. Calculation and results of fatigue notch factor

Specimen no.	d_c (mm)	R_{max} (mm)	S_d (mm)	$(\sigma_{r,B})_c$ (MPa)	N (Cycles)	$(\sigma_{r,B})$ (MPa)	k_{fc}
1	0.13	0.34	0.067	200	36.900.000	89	0.45
2	1.59	1.20	0.226	200	23.525.000	100	0.50
3	0.19	0.94	0.112	250	506.200	260	1.04
4	1.23	1.53	0.357	250	990.900	220	0.88
5	1.71	0.73	0.110	250	1.843.500	189	0.76
6	0.09	0.47	0.090	250	795.200	233	0.93
7	2.28	1.75	0.324	350	40.960	489	1.40
8	1.83	2.79	0.630	350	990	1270	3.63
9	1.25	2.62	0.465	350	15.590	622	1.78
10	0.13	0.39	0.064	350	244.690	313	0.90
11	0.16	1.01	0.170	350	298.170	298	0.85
12	0.38	1.15	0.271	350	161.660	347	1.00
13	1.61	1.68	0.317	350	24.790	554	1.58
14	2.31	1.78	0.349	350	25.420	551	1.57
15	2.34	1.36	0.232	350	15.570	623	1.78
16	2.68	3.37	0.775	350	3.360	914	2.61
17	1.93	2.70	0.483	350	38.640	496	1.42
18	1.58	0.60	0.101	350	94.180	397	1.13
19	1.61	1.58	0.105	350	218.940	322	0.92
20	1.06	0.56	0.098	350	241.750	314	0.90
21	2.06	2.01	0.515	250	512.090	260	1.04
22	1.26	0.82	0.159	250	1.479.890	199	0.80
23	1.34	0.98	0.210	250	969.380	222	0.89
24	1.12	0.93	0.202	250	1.116.900	214	0.86
25	1.19	1.23	0.215	250	770.800	235	0.94
26	1.23	1.21	0.227	250	870.960	228	0.91
27	1.52	1.15	0.261	250	560.300	254	1.02
28	2.05	2.29	0.469	250	389.010	279	1.12
29	1.64	1.80	0.304	250	594.100	251	1.00
30	2.16	2.06	0.522	250	463.070	267	1.07
31	1.56	1.67	0.366	250	634.200	246	0.98
32	1.46	1.26	0.217	250	676.080	243	0.97
33	1.39	1.28	0.254	250	741.300	237	0.95
34	2.06	2.59	0.717	250	268.000	301	1.20

Where $(\sigma_{r,x})$ is the mean stress range for class x at a reference number of cycles. This can be calculated by substituting the number of cycles to failure, N, into the fatigue power law equation. The value of $(\sigma_{r,x})_c$, represents the stress range which has been applied to the corroded specimen in the plane of crack. This relationship is illustrated in Figure 1, where the equation is evaluated at the mean cycle life for a group of specimens tested at a given stress range. In this study the base metal has been taken as

class B and the values of $(\sigma_{r,B})$ have been calculated and listed in Table 2 by using the following equation as fatigue power law:

$$\left(\sigma_{r,B}\right) = \left(\frac{K}{N}\right)^{1/m}.$$ (3)

Where K is the constant term relating to the mean-line of the results and m is the inverse slope of the mean-line $\log \sigma_r - \log N$ curve. The values of K and m were taken to be 2.34×10^{15} and 4.0 respectively for class B. It should be noted, that the specimens performed better than class B. These had a notch factor of less than 1.0, and were included in the regression analysis.

4. Fatigue notch factor in terms of corrosion penetration

Further investigation was carried out to develop a relation for fatigue notch factor, k_{fc} in terms of average corrosion penetration, d_c. Two approaches were considered. The first requires measurements of the average corrosion penetration, d_c, the standard deviation of roughness, S_d, the maximum roughness, R_{max} and the calculation of fatigue notch factor, k_{fc} based on the fatigue test.
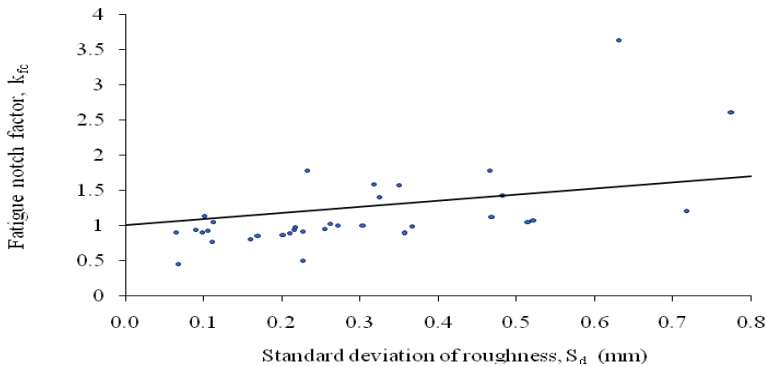
Fig. 2. Fatigue notch factor versus standard deviation of roughness

The fatigue notch factor for corroded specimens was calculated and plotted against standard deviation of roughness, S_d as shown in Figure 2. The following equation was produced from Figure 2 based on a mean regression line through the data points with the intercept of 1.0 calculated with the least-square-fit method:

$k_{fc} = 1 + 0.99S_d.$ (4)

The fatigue notch factor of a corroded member by having measurements on average corrosion penetration is given by

$k_{fc} = 1 + 0.2d_c.$ (5)

The following equation was produced for fatigue notch factor of corroded specimens in terms of maximum roughness, R_{max} by using the same procedure as used for Equation 4.

$$k_{fc} = 1 + 0.2R_{max}. \tag{6}$$

5. Fatigue notch factor in terms of the exposure time

An attempt has been made to develop a relation for fatigue notch factor in terms of the exposure time. The following relationship was developed for corrosion penetration in terms of exposure time [8]:

$$d_c = 90.74(t)^{0.75}. \tag{7}$$

In order to relate the effect of exposure time, t, to fatigue notch factor, k_{fc}, average corrosion penetration, d_c, from Equation 7 has been substituted into Equation 6.

$$k_{fc} = 1 + 0.018(t)^{0.75}. \tag{8}$$

Equation 8 can be used to calculate the fatigue notch factor of a corroded specimen or a member at any given exposure time in years.

6. Comparison of the fatigue notch factor with BS 5400 classes

The relationship developed for fatigue notch factor in terms of corrosion penetration (Equation 5) is plotted in Figure 3. Superimposed on this graph is the corresponding fatigue notch factor for different classes of structural detail as classified
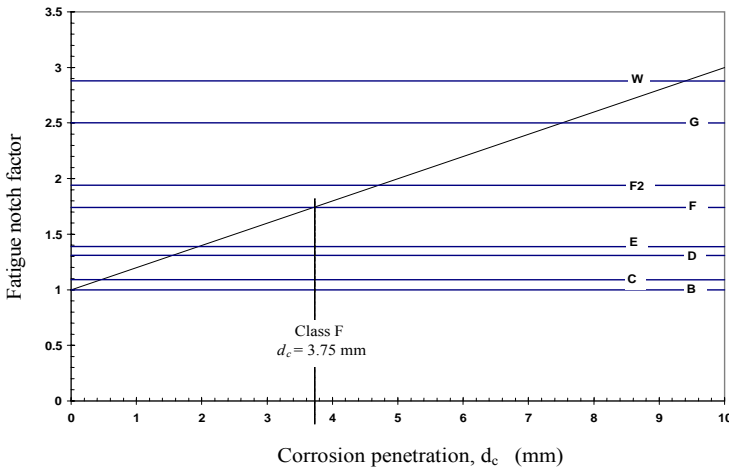
Fig. 3. Comparison of the relation developed for fatigue notch factor in terms
of corrosion penetration with BS 5400 classes

Table 3. Fatigue notch factor of new steelwork detail classes compared with corroded steelwork of equivalent corrosion penetration

Detail class	log K	m	k_f at 500.000 cycles	Equivalent d_c (mm)
B	15.37	4.0	1.00	0.00
C	14.03	3.5	1.09	0.40
D	12.60	3.0	1.31	1.65
E	12.52	3.0	1.39	1.95
F	12.24	3.0	1.74	3.75
F2	12.09	3.0	1.94	4.75
G	11.76	3.0	2.50	7.50
W	11.57	3.0	2.88	9.40

in BS 5400: Part 10 (1980), the UK code for fatigue design (Table 1) [10]. This equation was then used to obtain the equivalent value of d_c which corresponded to each of the structural detail classes. For example the fatigue notch factor curve intersects class F at a value of $d_c = 3.75$ mm. This is shown in Figure 3. This procedure was repeated for all classes and the results are given in Table 3.

Based on the results of the present study, two cases are possible, depending on whether the fatigue notch factor due to corrosion is smaller or greater than that of a given type of detail. If the fatigue notch factor due to corrosion is smaller than the fatigue notch factor for non-corroded detail, $k_f \geq k_{fc}$, then the fatigue notch factor of the detail, k_f, will govern. If, on the other hand, $k_{fc} \geq k_f$, the fatigue notch factor due to corrosion, k_{fc}, will govern.

7. Conclusions

It has been found that the fatigue notch factor is an appropriate parameter for quantifying the effect of corrosion deterioration on fatigue life and a comparison between the fatigue notch factor developed for corrosion penetration and the fatigue notch factor for a particular class should be made and the one of higher magnitude governs. Also two relationships developed for calculating fatigue notch factor which can be used for the assessment of corroded steel structures. The first is in terms of average corrosion penetration which increased on average with the average corrosion penetration and the second is in terms of exposure time. The assessment of the remaining fatigue life of existing corroded steel structures, in terms of fatigue notch factor, requires only information of the average corrosion penetration or the time of exposure at the time of the assessment. In particular, the relation of fatigue notch factor in terms of exposure time gives a direct, accurate, and quantifiable assessment of corroded members and it needs only the time of weathering.

References

[1] Aquino J.M., Della Rovere C.A., Kuri S.E.: *Localized corrosion susceptibility of super-martensitic stainless steel in welded joints*, J. of Corrosion Science, Vol. 64, No. 1, 2008, pp. 35–39.

[2] Nakai T., Matsushita H., Vamamoto N.: *Effect of pitting corrosion on the ultimate strength of steel plates subjected to in-plane compression and bending*, J. of Marine Sci. and Techno., Vol. 11, 2006, pp. 52−64.

[3] Ramachandra Murthy D.S., Madhava Rao A.G., Santhakumar A.R.: *Corrosion fatigue of stiffened offshore steel tubular joints*, J. of Struc. Eng., ASCE, Vol. 120, No. 7, 1994, pp. 1991−2010.

[4] Zuraski P.D., Johnson J.E.: *Research on the remaining life in steel ridges*, ASCE Speciality Conference on Probabilistic Mechanics and Structural Reliability, Berkeley, CA, 1984, pp. 414–418.

[5] Kitagawa H., Tsuji K., Hisada T., Hashimoto Y.: *An analysis of random pits in corrosion Fatigue: A statistical three-dimensional evaluation of an irregularly corroded surface*, Corrosion Fatigue: Mechanics, Metallurgy, Electrochemistry, ASTM STP 801, Crooker T.W. and Leis B. N, 1983, pp. 147–158.

[6] Albrecht P., Shabshab C.F., Li W., Wright W.: *Remaining fatigue strength of corroded steel beams*, International Association for Bridge and Structural Engineering Workshop, Vol. 59, 1990, pp. 71–84.

[7] Kuhn P., Hardraht H.F: *An engineering method for estimating the notch-size effect in fatigue tests on steel*, NACA TN2805, Langley Aeronautical Laboratory, Washington, 1991.

[8] Rahgozar R.: *Fatigue endurance of steel structures subjected to corrosion*, PhD Thesis, Department of Civil Engineering, University of Bristol, UK, 1998.

[9] Neuber H.: *Theory of stress concentration for shear-strained prismatical bodies with arbitrary non-linear stress-strain law*, J. of Applied Mech., Transactions of the ASME, Vol. 28, 1961, pp. 544–550.

[10] BS 5400, *Steel, concrete and composite bridges*, Part 10, Code of practice for fatigue, British Standards Institution, London, 1980.

[11] Fisher J.W., Albrecht P.A., Yen B.T., Klingerman D.J., McNamee B.M.: *Fatigue strength of steel beams with welded stiffeners and attachments*, NCHRP Report 147, Transportation Research Board, 1974.

[12] Kulicki J.M., Prucs Z., Sorgenfrei D.F., Mertz D.R.: *Guidelines for evaluating corrosion effects in existing steel bridges*, National Cooperative Highway Research Program, Report 333, Transportation Research Board, National Research Council, Washington, D.C., 1990.

[13] Albrecht P., Naeemi A.H.: *Performance of weathering steel in bridges, national cooperative highway research program*, Report 272, Transportation Research Board, National Research Council, Washington, D.C., 1984.

[14] Albrecht P., Shabshab C.F.: *Fatigue strength of weathered rolled beam made of A588 steel*, J. of Mater. in Civil Eng., ASCE, Vol. 6, No. 3, 1994, pp. 407−428.

[15] Rahgozar R.: *Remaining capacity assessment of corrosion damaged beams using minimum curves*, Journal of Constructional Steel Research, Elsevier, Vol. 65, No. 2, 2009, pp. 299–307.

Wpływ korozji na zmęczeniowy współczynnik karbu w mostach stalowych

W artykule przeanalizowano główne aspekty związane z koncentracją naprężeń powstałych na skutek korozji, opracowano funkcje zmęczeniowego współczynnika karbu w zależności od średniej penetracji korozji i czasu ekspozycji. W szczególności związek pomiędzy zmęczeniowym współczynnikiem karbu a czasem ekspozycji umożliwia bezpośrednią, dokładną i wymierną ocenę skorodowanych elementów na podstawie czasu ich wietrzenia. Ostatecznie zmęczeniowy współczynnik karbu skorodowanej konstrukcji stalowej porównano z bazującymi na brytyjskiej normie BS 5400 zmęczeniowymi współczynnikami karbu różnych elementów konstrukcyjnych.

Characteristics of Nd:YAG laser welded joints of dual phase steel

M.S. WĘGLOWSKI, K. KWIECIŃSKI, K. KRASNOWSKI, R. JACHYM

Institute of Welding, Testing of Materials Weldability and Welded Constructions Department, Błogosławionego Czesława 16–18, 44-100 Gliwice, Poland

Examination results of microstructure, mechanical properties, fatigue strength and residual stresses of laser welded joints in dual phase HDT580X steel have been presented. The main goal of these studies was to verify whether Nd:YAG laser welding without filler metal can be used for welding of dual phase steel. In the frame of this investigation the microstructure has been studied by optical and scanning microscopy. Mechanical properties have been analysed by tensile, bend and hardness tests. Additionally fatigue tests and residual stress measurements were carried out. The results revealed that the HDT 580X steel is characterized by good laser weldability. The tensile strength of welded joints is at the same level as that of the base metal and the maximum hardness does not exceed 343 HV. The microstructure of welded joints is mainly composed of lath martensite in the weld and a mixture of lath martensite, bainite and ferrite in the heat affected zone (HAZ). The fatigue class FAT was determined, which is equal to 284 MPa and 150 MPa for base material and welded joint, respectively. Residual stresses determined by the hole drilling method and the videoextensometer were: $\sigma_{max}= 573$ MPa and $\sigma_{min}= -126$ MPa.

Keywords: *dual phase steel, Nd:YAG, fatigue ,residual stress, videoextensometer*

1. Introduction

Fuel economy and, thereby, weight reduction have become a point of considerable interest in the car industry over the past 20 years. The body-in-white, the heaviest and largest car component, comprises about 25–30 percent of the total weight of a medium-sized passengers car. Hence, it has to fulfill a variety of material − relevant requirements. For car manufacturer, five demanding areas can be distinguished: cost, production, styling and space optimization, physical characteristics and quality, environmental impact [1]. The dominating role of steel as the material for car bodies is attributed to its good response to most of these requirements and its adaptability. Cold rolled, high strength sheet steels have been developed predominantly for automotive applications, and newly developed high strength steels are measured by the five criteria listed. Hence, the aim is to increase strength without decreasing formability, joinability, coatability, and also process ability [2]. Various new grades of steels – IF (Interstitial Free), DP (Dual

Phase), HSLA (High Strength Low Alloy) –have been developed which show excellent formability and are able to meet the most automotive requirements. The most popular grades of automotive steels are DP grades [1–3].

Dual Phase steel, so called because they consist essentially of a dispersion of martensite in a ferrite matrix, are produced by intercritically annealing and cooling at such a rate as to give the desired structure. Apart from the chemical composition, the microstructure and mechanical properties in the practical point of view the most important factor is "jointability" of automotive steels [4]. Traditionally, resistance welding and fusion welding have been used in the automotive industry. However, the most prospective welding process in this branch of industry is laser welding. The main advantages of laser welding are small distortions of the sheets caused by a small width of HAZ, high welding speed and flexibility of this process. Investigations which have been carried out so far and cover laser welding of DP steels, are focused on mechanical [5, 6] and structural properties [5, 7] of welded sheets in thicknesses lower than 2 mm. The research have shown [5] characteristics of Nd:YAG laser welded 600 MPa grade DP steel, 1.4 mm in thickness, in respect of hardness, microstructure, mechanical properties and formability. They concluded that the hardness in the HAZ was about 380 HV at the welding speed of 1.2 m/min and the laser power of 3.5 kW. The strength of the welded joint was higher than that of the base metal. The weld and HAZ was composed of ferrite and rapidly solidified structure (RSS). Dilthey et al. [6] has presented mechanical properties of DP600 steel welded joint 2.0 mm in thickness. They found that the hardness in the welded zone is higher than 400 HV and the tensile strength of the joint was at the same level as of the base metal. Krizan et al. [7] reported mechanical and structural properties of DP laser welded joints 1.5 mm in thickness. Welding was performed by a CO_2 laser welding unit operated in the continuous wave mode. The microstructure of the base metal consisted of ferrite, bainite and martensite. Both the fine-grained and the coarse-grained supercritical HAZ's consisted of lath martensite. In the weld a fully lath martensite was observed. Nagasaka et al. [8] reported on the improvement of the press formability of YAG laser welded TRIP/DP tailored blanks. They investigated the DP600 steel 1.2 mm in thickness. Anand et al. [9] determined the fatigue strength of dissimilar thickness laser-welded sheets and different coatings. The results showed that tailor welded blanks (TWB) made from zinc-coated/galvanized steels exhibited a lower fatigue limit as compared to the TWB combination from uncoated bare metal. Authors [10] presented results of the influence of martensite volume fraction on the fatigue limit of DP steel. They concluded that the higher volume of martensite improved the fatigue limit for rolled and not rolled materials. Some results of numerical simulation of distortion and residual stresses of DP steel weldments are also available [11]. Authors [11] concluded that the demonstrated numerical simulation of the welding process is a powerful tool for the prediction of distor-

tions and residual stresses in welded structures. Paper [12] contains microstructure analysis of DP600 steel after three different welding methods: MAG, resistance welding and braze welding. The authors conclude that the resistance welded zone is composed of the Widmannstätten structure with hardness about 420 HV.

However, there have been essentially no reports on laser welding of the DP600 steel more than 2 mm in thickness. Because of this, butt-welded joints 2.4 mm in thickness have been welded using a Nd:YAG laser, and their microstructure, mechanical properties, fatigue strength and residual stresses were examined and tested. The aim of investigation presented in this paper is to perform good quality joints of thick steel sheets. Applications for this kind of joints include mainly automotive industry etc. bumper reinforcements, pillars and beams.

2. Experimental procedure

2.1. Welding procedure

The 2.4 mm thick hot rolled sheets of dual phase steel (HDT580X acc. to PN-EN 10336:2007 [13]) were laser welded at a robotized laser stand which, was composed of the solid state laser Nd:YAG TRUMPH HL 2000D, the focusing head TRUMPF D70 and the robot KUKA – KR 30/2 HA. The chemical composition of the HDT580X steel is given in Table 1.

Table 1. Chemical composition of HDT580X steel [%]

C	Mn	Si	P	S	Cu	Cr	Ni
0.07	0.90	0.09	0.028	0.001	0.04	0.40	0.04
Mo	V	Al	N	Nb	Ti	B	Sn
0.01	0.004	0.039	0.0058	0.002	0.022	0.0003	0.003

Ito and Bessyo [15] define the carbon equivalent of steel with the carbon content in mass % less than 0.18 as follows:

$$CE = C + \frac{Si}{30} + \frac{Mn + Cu + Cr}{20} + \frac{Ni}{60} + \frac{Mo}{15} + \frac{V}{10} + 5B. \tag{1}$$

The carbon equivalent of the HDT580X steel is 0.14 %.

Before welding the surface of the specimens was chemical cleaned by acetone. Butt welding was performed acc. to EN ISO 15614-11:2005 [14]. The joints were produced by deep penetration welding method (also known as keyhole welding) without filler metal at the following welding parameters: beam power at workpiece – 2.0 kW, travel speed – 2.1 m/min, shielding gas – argon at a flow rate of 16 l/min, working distance – 223 mm. Tensile tests, bend tests and metallographic examination were done on specimens cut off the welding joints.

2.2. Testing

Transverse sections of the welded joints passing through the weld centre as well as sections of base metal were prepared by a standard metallographic procedure and etching in 3% alcoholic nitric acid solution. The microstructural examinations were carried out by an optical microscope LEICA MEF4M and scanning electron microscope HITACHI S-3500N. The microstructure of base metal was also studied by TEM – JEM200CX.

The Vickers microhardness measurement across the weld and the base metal was carried out on metallographic specimens at a load of 500 g. During microhardness testing the indentations were randomly made on the matrix without marking the specific phases. However, in case of welded specimens specific attention was paid to place the indentations in the region of HAZ and weld. Hardness measurement of the welded sheet was performed by using the Zwick hardness tester.

The tensile tests of the welded joints (acc. to EN 895 [16]) as well as of the base metal (acc. to EN 10002-1 [17]) was performed on a mechanical universal testing machine (INSTRON 1420) by using three specimens. The bend tests were carried out on a mandrel of 10 mm in diameter acc. to EN 910 [18]. The tensile and bend tests were performed at room temperature.

The fatigue properties of the laser welds and base metal were determined on the universal fatigue machine 1000 kN MTS type 311.31 at a frequency in the range from 15 to 20 Hz. Tests were conducted at room temperature at a load ratio $R = 0.2$ (where $R = \sigma_{min}/\sigma_{max}$). The analysis of data was performed acc. to the document XIII-2151-07/XV-1254-07 of the International Institute of Welding (IIW) [19].

The distribution of residual stresses in welded joints was determined by using the hole-drilling method [20] and videoextensometer type Messphysik ME-46. A full image video-camera was focused on the test specimen upon which contrasting marks (targets) have been plotted and the resulting image was analyzed in real time by a PC-based video processor. The associated software ensures that the distance between targets is continuously measured during testing. The Video Extensometer automatically acts as a "strain meter" by directly calculating the measured extension as a percentage of the original length. Then the extensions were calculated to stresses.

3. Results and discussion

3.1. Base metal

The dual phase structure of the base metal, revealed by nital etching, with martensite islands (dark areas) in a ferrite matrix (white areas) is shown in Figure 1a. Due to the fact that in some cases dark areas can be indicated as ferrite, the colour etching by the Beraha reagent has been used to unambiguously identify the martensite phase. Figure 1b shows the effect of colour etching of the base metal – white areas are martensite, dark areas – ferrite. The authors of the publication [21] have indicated that

the microstructure of a dual phase steel can consist of martensite and fine pearlite islands in ferrite matrix or martensite and bainite islands in ferrite matrix. The small content of carbon causes that the presence of pearlite phase is of little probability. To estimate the real microstructure of the HDT580X steel, the SEM microscope was used. Figure 2a shows the SEM microstructure of base metal which is composed of martensite-austenite (M-A) islands in a ferrite matrix. The SEM techniques did not reveal the bainite and pearlite phases. So, the TEM microscope was used, which shows that the microstructure of the HDT580X steel is composed of martensite-austenite islands in ferrite matrix, in some island bainite is also present (Figure 2b).

The mechanical properties of HDT580X steel are given in Table 2.
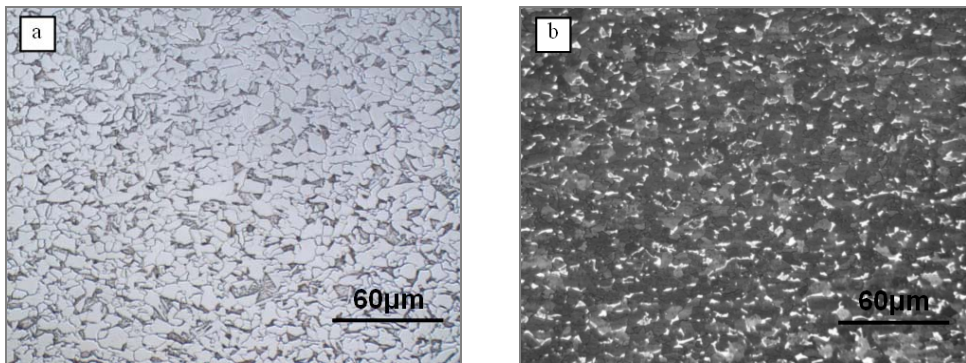
Fig. 1. Microstructure of HDT 580X steel, a) etched by Nital 3% reagent,
b) colour etched by Beraha reagent
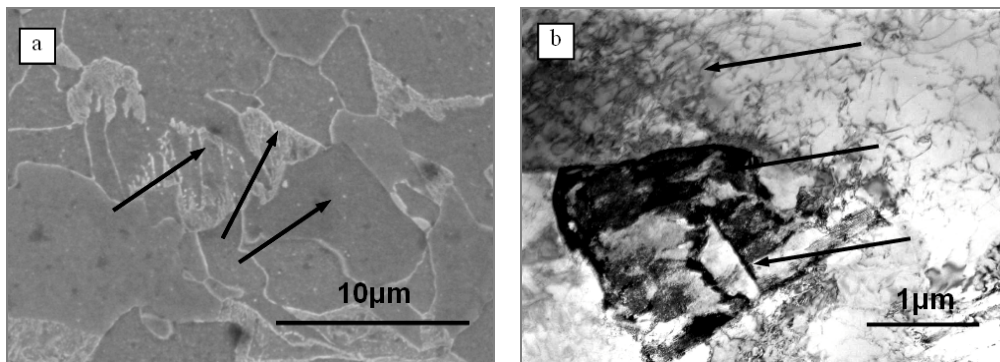
Fig. 2. Microstructure of HDT 580X steel, a) SEM – etched by Nital 3% reagent,
b) TEM. F – ferrite, M – martensite, B – bainite, A – austenite

3.2. Macrostructure and microstructures of the welded joint

Figure 3 shows the macrostructure of the laser weld of DP steel. As can be seen the weld is well formed and free of imperfections, i.e. without porosities or cracks in the

fusion zone. The epitaxial crystallisation of the fusion zone initiated on the fusion boundary with the formation of columnar grains that grew towards the weld centre line. The quality level of this joint has been determined as B acc. to EN ISO 13919-1 [22].

Etch. Nital 3%   ×10
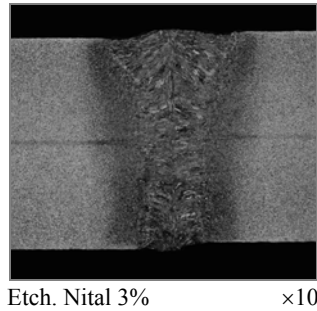
Fig. 3. Macrostructure of the laser welded (2.0 kW, 2.1 m/min) HDT 580X steel joint

Table 2. Mechanical properties of HDT580X steel (mean values)

	Orientation to rolling direction	
	longitudinal	transverse
R_m	612 MPa	630 MPa
R_e	420 MPa	423 MPa
A_5	31.5 %	27.9 %
A_{10}	24.5 %	22.23 %
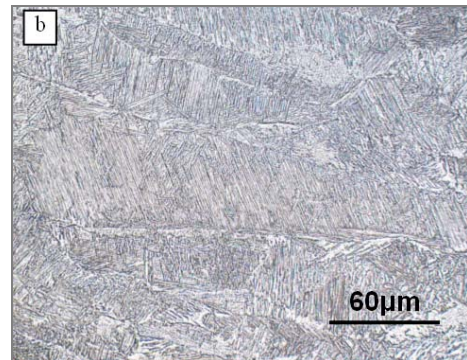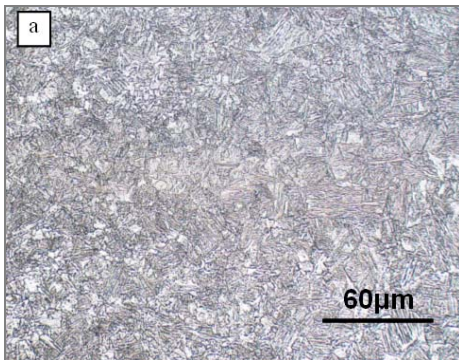
Fig. 4. Microstructure of welded HDT 580X steel. Optical microscope, a) HAZ b) weld

The optical microstructures of the HAZ and weld observed in the welded joint are shown in Figure 4. The structure of the HAZ is composed of ferrite, bainite and martensite (Figure 4a). The microstructure of the weld is uniform and consists of lath martensite, typical for this kind of low carbon steel. The lath martensite is built in packets as shown in Figure 4b.
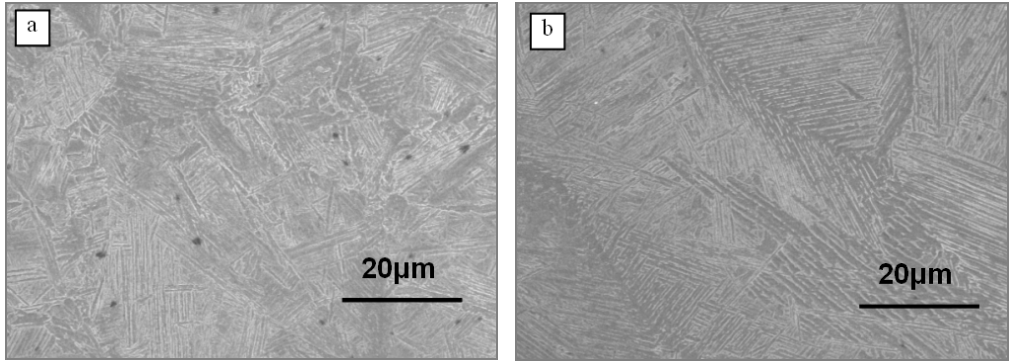
Fig. 5. SEM microstructure of the welded joint, a) HAZ, b) weld

Figure 5 shows the SEM microstructure of the HAZ and weld. The results of SEM confirmed those achieved by optical microscopy. The HAZ is composed of a mixture of ferrite, martensite and bainite. In the weld zone a fully lath martensite structure was observed due to the rapid cooling.

3.3. Microhardness across the welded joint

The changes of hardness across the weld in the cross sectional plane of the laser welded joint are shown in Figure 6. The base material hardness values did not exceed 226 HV. In the HAZ there was an increase of hardness to 285 HV. The maximum hardness 343 HV was observed in the weld. These results confirmed that the low carbon lath martensite was present in the weld and HAZ.
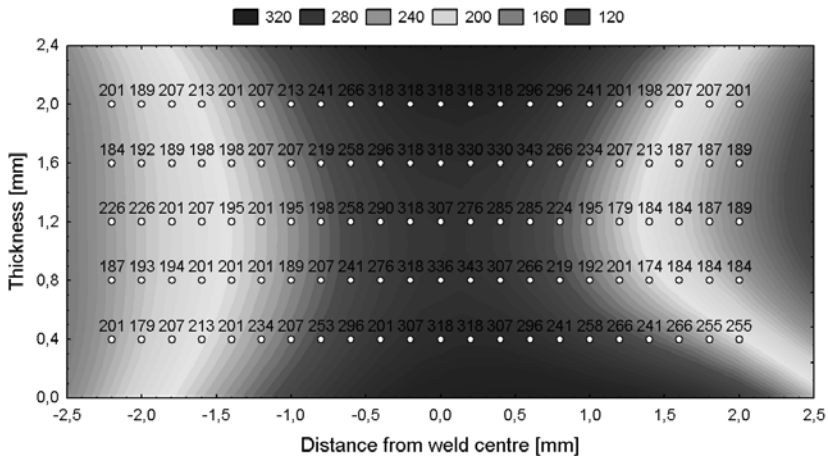
Fig. 6. Microhardness distribution across the welded joint

3.4. Mechanical properties

The tensile test revealed that the strength of welded joints is at the same level as that of the base material, and equals R_m = 631 MPa (average value of three specimens). All specimens fractured in the base metal away from the weld. These results indicate that the strength of welded joints is not less that that of the base material

The bend tests were performed up to the angle of 180°, for all cases on the surface of welds cracks or other imperfection did not occur.

So, based on structural and mechanical properties of the welded joints, it can be concluded that the welding parameters used in the tests guarantee their proper quality.

3.5. Fatigue strength

Fatigue tests were performed to establish fatigue strength curves for the base material and welded joint. Figure 7 shows the fatigue sample for the base metal and welded joints. Statistical methods offer three ways of testing a limited number of samples from a larger population [19]:
- a specimen to failure,
- first specimen to failure,
- p specimens to failure amongst n specimens.
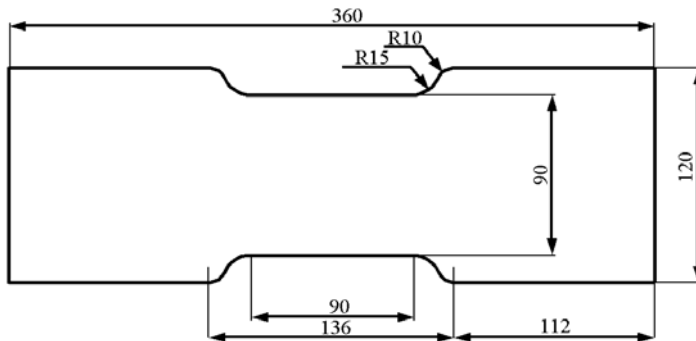
Fig. 7. Fatigue sample for base metal and welded joints

The presented results are based on the first method – specimen to failure. The test results were obtained at constant stress ratios R. The S–N data was presented in a graph showing log(endurance in cycles) as the abscissa and log(range of fatigue actions) as the ordinate (Figure 8). In order to get the defined fatigue characteristic values at $2 \cdot 10^6$, the fatigue test data have been calculated using a statistical method [19]. These characteristic values are, in principle, values at α = 95% survival probability (5% probability of failure) associated to a two sided confidence interval of 75% of the mean x_k and of the standard deviation Stdv of β = 75% (12.5% probability of being above or below the extreme values of the confidence interval).
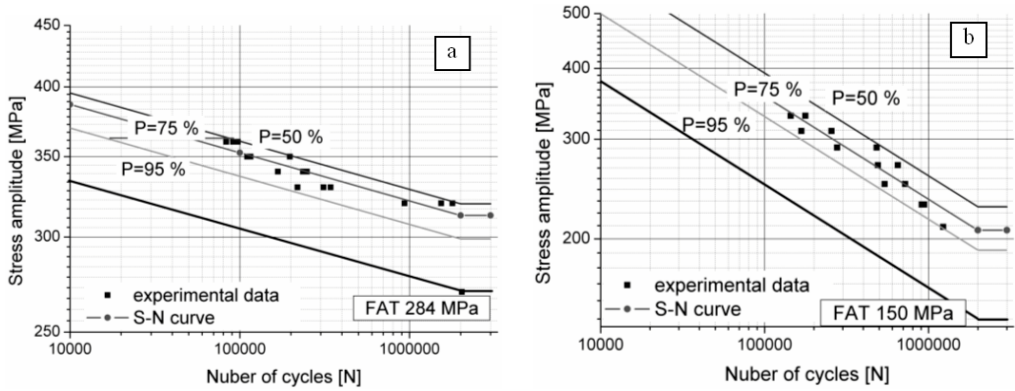
Fig. 8. Fatigue resistance for the base material, a) and welded joint, b) *P*-probability

For the evaluation of test data originating from a test series, the characteristic values were calculated by the following procedure:

a) computing the $\log_{10}$ of all data: stress range $\Delta\sigma$ and number of cycles N,

b) computing the exponents m and constant $\log C$ of the formula:

$$\log N = \log C - m \cdot \log \Delta\sigma, \tag{2}$$

by linear regression take stress as the independent variable:

$$\log N = f(\log \Delta\sigma) \tag{3}$$

c) computing the mean x_m and standard deviation *Stdv* of $\log C$ through m,

d) computing the characteristic values x_k by the formula:

$$x_k = x_m - k \cdot Stdv, \tag{4}$$

where k is equal 2.4 [19] for 15 fatigue samples.

For the base material, the regression line (2) is expressed as:

$$\log N = 68.49 - 24.96 \log(\Delta\sigma), \tag{5}$$

for the welded joint:

$$\log N = 19.06 - 6.51 \log(\Delta\sigma). \tag{6}$$

The calculated results indicate that the fatigue class – FAT for the HDT580X steel and welded joint equals 284 MPa and 150 MPa, respectively.

3.6. Residual stress

The residual stresses in the area surrounding the drilled hole relax. The hole was made by a drill 1.2 mm in diameter. The method is based on the measurement of the relieved strains by the videoextensometer and than by computing the stresses. The measurements of residual stresses in the area of the welded joint were performed acc. to the following procedure [20, 23]:
– computing the stresses σ_{max}, σ_{min} from:

$$\sigma_{min}, \sigma_{max} = \frac{E(\varepsilon_3 + \varepsilon_1)}{4A'} \pm \frac{E\left(\sqrt{(\varepsilon_3 - \varepsilon_1)^2 + (\varepsilon_3 + \varepsilon_1 - \varepsilon_2)^2}\right)}{4B'}, \tag{7}$$

where:
    A', B' – calibration constants,
    ε_1, ε_2, ε_3 – relieved strains,
    E – Young's modulus,
– computing the constants A', B' from:

$$A' = -(1 + v) \cdot \frac{a}{r}, \ B' = \frac{a}{r}\left[(1 + v)\cdot\left(1 + \frac{a}{r} + \frac{a^2}{r^2}\right) - 4\right] \tag{8}$$

where:
    v – Poisson's ratio,
    a – radius of drilled hole 1.2 mm in diameter (see Figure 9),
    r – radius of videoextensometer measurement base circle (see Figure 9),
    – computing the relieved strains ε_1, ε_2, ε_3 from:

$$\varepsilon_1 = \frac{\Delta A}{2r}, \ \varepsilon_2 = \frac{\Delta B}{2r}, \ \varepsilon_3 = \frac{\Delta C}{2r}, \tag{9}$$

where ΔA, ΔB, ΔC – reference bases (see Figure 9),
    – computing the angle α (measured clockwise from direction of base ΔC to the direction of σ_{max} – see Figure 9) from:

$$\alpha = \frac{1}{2}\text{arctag}\left(\frac{\varepsilon_3 + \varepsilon_1 - \varepsilon_2}{\varepsilon_3 - \varepsilon_1}\right). \tag{10}$$

For reasons of pictorial clarity in Figure 9, the principal residual stresses σ_{max}, σ_{min} are shown as uniformly acting over the entire region around the hole location. In

actuality, it is not necessary for the residual stresses to be uniform over such a large region.

The relived strains depend only on the principal stresses originally existing at the boundaries of the hole. The stresses beyond the hole boundaries do not affect the relieved strains. Because of this, the hole drilling method combined with the videoextensometer provides a very localized measurement of residual stresses.
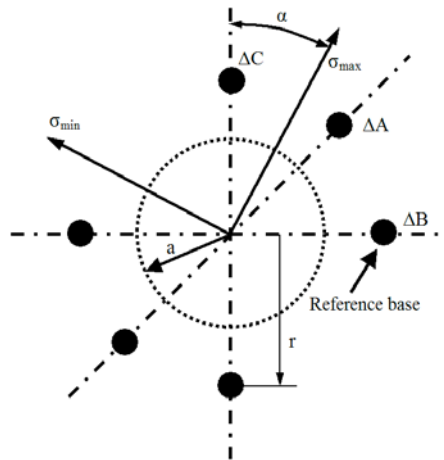
Fig. 9. Schematic diagram of videoextensometer reference bases arrangement

After calculation the residual stresses σ_{max} = 573 MPa, σ_{min} = –126 MPa and the angle α = 33.8°.

3. Conclusion

The characteristics of Nd:YAG laser welded HDT580X steel joint was investigated in respects of hardness, mechanical properties, fatigue resistance and residual stress and the following results were obtained:

– the structural examination of the weld cross sections revealed that the welds were free of any defects such as porosity, concavity, voids, inclusions or misalignment. This indicates that the laser welding parameters are appropriate to obtain sound welds;

– the microstructure of the HDT580X steel is composed of martensite-austenite islands in ferrite matrix, in some islands bainite was observed;

– the macroscopic examination and mechanical tests indicate that it is possible to achieve good quality welds by the application of proper welding parameters;

– the welding process has an affect on the fatigue class, the FAT for the base material is 284 MPa, and for the welded joint 150 MPa;

– the welding residual stresses are: σ_{max} = 573 MPa and σ_{min} = –126 MPa.

References

[1] Hamm L.: *Stahl–ein zukunftsträchtiger Werkstoff im Karosseriebau?*, Proc. IISI 27th Annual Meeting and Conference, Paris, 1993.

[2] Bleck W.: *Cold rolled high strength sheet steels for auto applications*, JOM, No. 7, 1996, pp. 26–31.

[3] Kuziak R., Kawalla R., Waengler S.: *Advanced high strength steels for automotive industry*, Archives of Civil and Mechanical Engineering, Vol. 8, No. 2, 2008, pp. 103–117.

[4] Svensson L.E., Larsson J.K.: *Welding and joining of high performance car bodies*, Steel World (UK), Vol. 7, No. 7, 2002, pp. 21–32.

[5] Kang C.Y., Han T.K., Lee B.K., Kim J.K.: *Characteristics of Nd:YAG Laser Welded 600 MPa Grade TRIP and DP Steel*, Materials Science Forum, Vol. 539–543, 2007, pp. 3967–3972.

[6] Dilthey U., Ghandehari A., Bleck W., Budak I.: *Mechanical-technological properties of beam welded high and ultra high strength steels*, Zeitschrift für Metallkunde, Vol. 92, No. 3, 2001, pp. 221–225.

[7] Krizan D., Waterschoot T., Koruk A.L., De Coman B.C.: *Bake hardening of laser welded Dual Phase steel*, Steel Research, Vol. 74, No. 10, 2003, pp. 639–645.

[8] Nagasaka A., Sugimoto K.I., Kobayashi M., Makii K.: *Press formability of YAG laser welded TRIP/DP tailored blanks*, J. Phys. IV France, Vol. 115, 2004, pp. 251–258.

[9] Anand D., Chen D.L., Bhole S.D., Andreychuk P., Boudreau G.: *Fatigue behavior of tailor (laser)-welded blanks for automotive applications*, Materials Science and Engineering A, Vol. 420, 2006, pp. 199–207.

[10] Sarwar M., Priestner R., Ahmad E.: *Influence of martensite volume fraction on fatigue limit of Dual Phase steel*, Journal of Materials Engineering and Performance, Vol. 11, No. 3, 2002, pp. 274–277.

[11] Brand M., Siegele D.: *Numerical simulation of distortion and residual stresses of dual phase steel weldments*, Welding in the World, Vol. 51, No. 9–10, 2007, pp. 56–62.

[12] Kustroń P., Rutkowska – Gorczyca M., Ambroziak A., Lachowicz M.: *Microstructure of welds of modern steel DP600 applied in automotive industry*, Proceedings of XXXVI Materials Engineering School, Kraków–Krynica 2008, pp. 203–207.

[13] EN 10336:2007 – *Continuously hot-dip coated and electrolytically coated strip and sheet of multiphase steels for cold forming. Technical delivery conditions*.

[14] EN ISO 15614-11:2002 – *Specification and qualification of welding procedures for metallic materials. Welding procedure test. Part 11: Electron and laser beam welding*.

[15] Ito I., Besssyo K.: *Weldability formula of high strength steels*. IIW document IX-576-68.

[16] EN 895:1995 – *Destructive tests on welds in metallic materials – Transverse tensile test*.

[17] EN 10002-1:2001 – *Metallic materials. Tensile testing. Part 1: Method of test at ambient temperature*.

[18] EN 910:1999 – *Destructive tests on welds in metallic materials – Bend tests*.

[19] Hobbacher A.: *Recommendations for fatigue design of welded joints and components revision of XIII-1539-96 / XV-845-96*, IIW document XIII-2151-07/XV-1254-07.

[20] ASTM Standard E837-92 *Standard test method for Determining Residual Stresses by the Hole-Drilling strain-Gage Method*.

[21] Gupta P., Ghosh P.K., Nath S.K., Ray S.: *Resistance spot weldability of plain carbon and low alloy dual phase steels*, Zeitschrift für Metallkunde, Vol. 81, No. 7, 1990, pp. 502–508.

[22] EN ISO 13919-1:1996 – *Welding. Electrons and laser beam welded joints. Guidance on quality levels for imperfections* – Part 1: *Steel*.

[23] Sędek P.: *Modification of the hole-drilling method of residual stress measurement* (Part 1) (in Polish), Welding Institute Bulletin, Vol. 37, No. 3, 1993, pp. 36–39.

Charakterystyka złączy ze stali typu Dual Phase spawanych laserem typu Nd:YAG

W artykule przedstawiono wyniki badań strukturalnych, własności mechanicznych, oraz badań zmęczeniowych i pomiarów naprężeń własnych złączy spawanych wiązka laserową ze stali typu Dual Phase (HDT580X). Celem przeprowadzonych badań było sprawdzenie możliwości wykonania prawidłowych złączy spawanych laserowo przy użyciu lasera typu Nd:YAG bez materiału dodatkowego. Ocenę budowy strukturalnej złączy przeprowadzono przy użyciu mikroskopu optycznego i skaningowego, a materiału podstawowego dodatkowo przy użyciu transmisyjnego mikroskopu elektronowego. Badania własności mechanicznych obejmowały próby statycznego rozciągania, zginania i pomiarów twardości. Dodatkowo przeprowadzono badania zmęczeniowe i pomiary naprężeń własnych. Przeprowadzone badania wykazały, że stal HDT 580 X jest łatwo spawalna przy użyciu wiązki lasera Nd:YAG. Wytrzymałość złączy była na poziomie materiału rodzimego. Maksymalna twardość w obszarze spoiny wynosiła 343 HV. Struktura spoiny składała się głównie z martenzytu listwowego, a SWC z mieszaniny martenzytu listwowego, bainitu i ferrytu. Kategoria zmęczeniowa FAT dla materiału podstawowego wynosiła 284 MPa, a dla złącza spawanego 150 MPa. Do wyznaczenia poziomu naprężeń własnych zastosowano zmodyfikowaną metodę otworkową. Pomiary odkształceń przeprowadzono przy użyciu wideoekstensometru. Naprężenia główne wyniosły σ_{max} = 573 MPa, a σ_{min} = –126 MPa.